Unterschrift des Betreuers

DIPLOMARBEIT

Quality of the CMS Tracker End Cap Silicon Strip Modules

ausgeführt am

Institut für Hochenergiephysik
der Österreichischen Akademie der Wissenschaften

und am

Atominstitut
der Österreichischen Universitäten

unter Anleitung von
Univ.Doz. Dipl.-Ing. Dr.techn. Manfred KRAMMER

durch

Stephan Hänsel

Schönbrunnerstrasse 110/2/24
1050 Wien

14. Februar 2006

Unterschrift

Preface

The Large Hadron Collider (LHC) at CERN, a 2×7 TeV proton-proton collider, is planned to be operable in 2007 and will run for at least 10 years. The Compact Muon Solenoid (CMS), a huge multipurpose detector, is one of the four major experiments at the LHC. The construction of the Inner Tracker of CMS required more than 15.000 silicon micro-strip detector modules including about 24.000 large area silicon strip sensors.

This diploma thesis has been composed at the Institute for High Energy Physics (HEPHY) of the Austrian Academy of Sciences [1]. It reviews the quality assurance for the 6.400 silicon micro-strip detector modules, built of one or two silicon strip sensors, in the Tracker End Caps (TEC), one out of four subsystems of the Inner Tracker. In the production laboratories, including our institute, the main steps during the fabrication of these modules are reception tests of the industrially produced module parts, their precise mechanical assembly, application of thin wire micro-bond connections and electrical functionality tests of the finalised modules.

This diploma thesis begins with a short overview of the Large Hadron Collider taking a deeper look at the CMS experiment. Then an overview of silicon sensors and the basic elements of the TEC silicon strip modules are provided. Afterward the quality assurance program during the module production and its results are presented.

At HEPHY Vienna the complete production of the Tracker End Cap Ring 2 modules was performed. My first task was to review the module assembly precision at our institute, where some problems had to be solved. At the same time I became responsible for the testing of the frames and front-end hybrids before the module assembly and the tests of the finalised modules. This included the fine-tuning of the cuts for the fault finding algorithm of the automated setup for the hybrid and module tests and the repair of different faults. I investigated the problem of the conductive glue on the sensor backplane and developed a solution. Later on I started to monitor the quality of the whole TEC module production and to supervise the repairs and the sensor recuperation of the faulty modules together with Marko Dragicevic and Thomas Bergauer. We characterised every faulty module and with the help of a specially created data base we could produce a statistic on them. Finally I became responsible for characterising and repairing of the TEC spare modules.

Kurzfassung

Der Large Hadron Collider (LHC) am CERN soll 2007 in Betrieb genommen und 10 Jahre lang für Experimente verwendet werden. Der Compact Muon Solenoid (CMS), ein so genanntes "multi purpose" Experiment, ist eines der vier großen Experimente am LHC. Der Bau des Siliziumdetektors von CMS benötigte mehr als 15.000 Detektormodule mit ungefähr 24.000 grossflächigen Silizium Sensoren.

Diese Diplomarbeit wurde am Institut für Hochenergiephysik (HEPHY) in Wien verfasst und beschäftigt sich mit der Qualitätssicherung wärend der Produktion der 6.400 Detektor Endkappen (TEC) Module des CMS Siliziumdetektors. Die wichtigsten Schritte bei der Produktion dieser Module, bei der unser Institut einen wichtigen Beitrag geleistet hat, sind Eingangstests der industriell hergestellten Einzelteile, deren präziser Zusammenbau, Bonden der elektrischen Verbindungen und die abschließenden Funktionalitätstests der fertigen Module.

Nach einem Überblick über den LHC und das CMS Experiment werden die Eigenschaften von Silizium-Streifen Sensoren und die Bestandteile der Detektormodule beschrieben. Abschließend wird die Qualitätssicherung wärend der Modulproduktion und deren Ergebnisse präsentiert.

Am HEPHY wurden alle Ring 2 Detektormodule der beiden Detektor Endkappen produziert. Meine Arbeit begann mit einem Genauigkeitsproblem beim Modulzusammenbau, das gelöst werden konnte. Zeitgleich übernahm ich die Verantwortung für die Tests der Rahmen, der Front End Hybride und der fertigen Module. Dabei half ich die Feineinstellungen des Fehleranalyse-Algorithmus der Testsoftware für die Hybrid- und Modultests zu verbessern. Kaputte Hybride und Module wurden, wenn möglich, von mir repariert. Weiters habe ich die Probleme mit dem Leitkleber an der Sensorrückseite untersucht und eine Lösung entwickelt. Später fing ich an die Qualität der gesamten TEC Modulproduktion zu überwachen und mir die kaputten Module genauer anzusehen. Das HEPHY entwickelte sich zum "TEC Module Repair Center" und zerlegte außerdem alle Module bei denen nur noch der Sensor gerettet werden konnte. Gemeinsam mit Marko Dragicevic und Thomas Bergauer wurden alle kaputten Module charakterisiert und mithilfe einer speziell erzeugten Datenbank eine Statistik produziert. Schlussendlich wurde die Aufgabe der Charakterisierung und Reparatur von Ersatzmodulen von mir übernommen.

Contents

Chapter 1

Introduction

The Standard Model of elementary particle physics (SM) has proved to be a successful theory and was able to make important predictions. Although there is no confirmed accelerator data that contradicts it, there are some theoretical reasons to consider it unsatisfactory and to expect some physics beyond the SM. One of the main reasons to make it an unattractive candidate for a 'theory of everything' is, that it contains too many free parameters. To gain deeper insight into the theory and to confirm yet unexplored predictions, particle collisions at energies as high as never reached before in an experiment are required. The Large Hadron Collider (LHC) at CERN[1] is a huge step forward in exploring the higher energy regime of the Standard Model. One of the most important open questions is the origin of mass. In the Standard Model the masses of fermions and the quanta of the weak interaction, the W- and Z-bosons, are anticipated to be massless. Instead the bosons are among the heaviest known particles. To handle this problem the Higgs mechanism was postulated. In this theory masses of particles are explained by their coupling with a so-called Higgs field, an additional scalar field with a non-vanishing vacuum expectation value. As a consequence of this mechanism, an additional particle, the Higgs boson, must exist. Unfortunately the mass of this particle is not predicted by the model.

Till now this Higgs mechanism could not be confirmed. Former particle physics experiments combined with theoretical considerations could only constrain the mass of the Higgs boson between 114,4 GeV/c^2 and 1 TeV/c^2. With the Large Hadron Collider particles of this mass and even beyond will be producible for the first time. The Higgs boson both completes the Standard Model of particle physics, and points to how to extend the Standard Model.

Besides this most prominent example there exist a huge spectrum of envisaged physics analysis. Another main goal of the LHC project is the search for potential supersymmetric particles. The discovery of these supersymmetric partners would confirm a very popular idea suggested for the unification of the forces, which is called supersymmetry (SUSY). The LHC will also lead to a deeper understanding of the puzzle around the lack of an exact CP symmetry, like described in [2].

[1] CERN: Conseil Europ*é*en pour la Recherche Nucl*é*aire (http://cern.ch)

1.1 Large Hadron Collider

The Large Hadron Collider (LHC) is being build in the former tunnel of the Large Electron Positron Collider (LEP) at CERN. This circular tunnel lies around 50 to 175 meters below the surface and crosses the Swiss and the French borders on the outskirt of Geneva. The 27 km long tunnel houses 1.232 super-conducting dipoles that produce a magnetic field of 8,33 Tesla each, which is necessary to keep the beams on their trajectories. The LHC is designed to collide two counter rotating beams of protons or heavy ions (Pb-Pb). In the proton-proton mode it will operate with a center of mass energy of 14 TeV ([2]). The two beams cross only at four points. Around these so called collision points huge detector systems are built in order to measure the interactions of the colliding particles. Altogether four major and one minor experiment are located at the LHC. Two of the major experiments, ATLAS[3] at Point 1 and CMS[4] at Point 5 are build around the two high-luminosity collision points located in diametrically opposite sections, see Figure 1.1. The other large experiments are ALICE[5] at Point 2 and LHC-B[6] located at Point 8. The minor

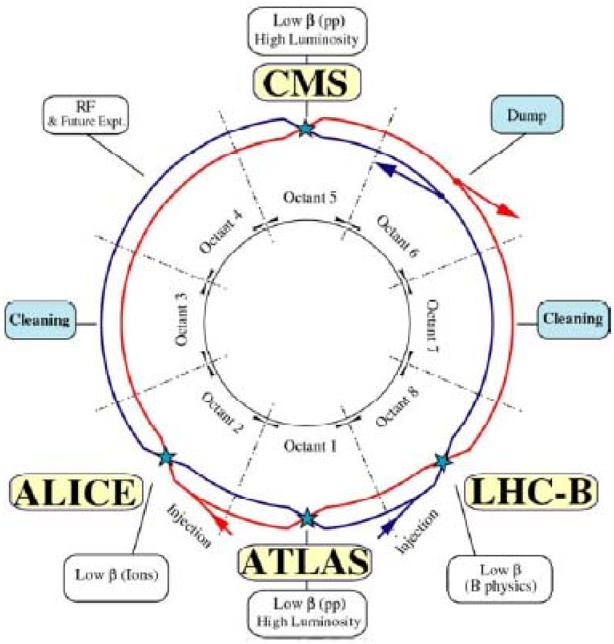

Figure 1.1: Schematic overview showing the four main experiments and the two ring structure of the LHC

experiment is TOTEM[7] which is located close to the LHC beam axis on both

[2] 1 TeV is about the energy of motion of a flying mosquito. Extraordinary is that LHC squeezes this energy into a space about a million million times smaller than a mosquito.

[3] ATLAS: A Toroidal LHC ApparatuS (http://atlas.ch/)

[4] CMS: Compact Muon Solenoid (http://cmsinfo.cern.ch/outreach/index.html)

[5] ALICE: A Large Ion Collider Experiment (http://aliceinfo.cern.ch/)

[6] LHC-B: Large Hadron Collider beauty experiment (http://lhcb-new.web.cern.ch/)

[7] TOTEM: Total Cross Section, Elastic Scattering and Diffraction Dissociation (http://totem.web.cern.ch/Totem/)

sides of the CMS detector. Two more initiatives, MOEDAL and LHCf are being proposed for the LHC, but till now only the technical designs have been worked out [3].

The LHC machine parameters relevant for the operation of the detectors are listed in Table 1.1. It comprises 9.300 magnets including 1.232 dipoles and 858 quadrupoles which optimize the particle trajectories. Eight radiofrequency (RF) cavities per beam ensure high luminosity at the collision points and hence maximise the number of collisions. The luminosity is the interaction rate of particles per unit cross-section and given by:

$$\mathcal{L} = \frac{\gamma f k_B N_p^2}{4\pi \epsilon_n \beta^*} F, \tag{1.1}$$

where γ is the Lorentz factor, f is the revolution frequency, k_B is the number of bunches, N_p is the number of protons/bunch, ϵ_n is the normalized transverse emittance (with a design value of 3,75 μm), β^* is the betatron function at the interaction point (IP) and F is the reduction factor due to the crossing angle.

		pp	HI	
Energy per nucleon	E	7	2,76	TeV
Dipol field at 7 TeV	B	8,33	8,33	T
Design Luminosity (*)	$\mathcal{L}$	10^{34}	10^{27}	$cm^{-2}s^{-1}$
Bunch separation		25	100	ns
No. of bunches	k_B	2.808	592	
No. particles per bunch	N_p	$1{,}15\times10^{11}$	$7{,}0\times10^{7}$	
Collisions				
B-value at IP	β^*	0,55	0,5	m
RMS beam radius at IP	σ^*	16,7	15,9	μm
Luminosity lifetime	τ_L	15	6	hr
Number of collisions/crossing	n_c	≈20		

Table 1.1: The machine parameters relevant for the LHC detectors, listed for the proton-proton (pp) hand heavy-ion (HI) interactions. ((*) ... For HI operation the design luminosity for Pb-Pb collisions is given.)

Also relevant is the bunch structure of the beam. The gaps between the particle bunches can be used for synchronization, acquiring calibration data and providing resets to front-end electronics. The beam structure is defined by the injection chain of the protons and ions, which can be seen in Figure 1.2. At the beginning of the proton injection chain, protons generated in a proton-source are injected into a radio-frequency (RF) cavity, which accelerates them to 750 keV. After this, they are transmitted to a proton linear accelerator (proton LINAC), where they reach energies of 50 MeV. The proton synchrotron Booster (PSB) increases the energy up to 1,4 GeV and sends the protons to the 26 GeV Proton Synchrotron (PS). There the bunches get formed with the correct 25 ns spacing. Then the beam is accelerated to 450 GeV in the Super Proton Synchrotron (SPS) and finally injected into the LHC.

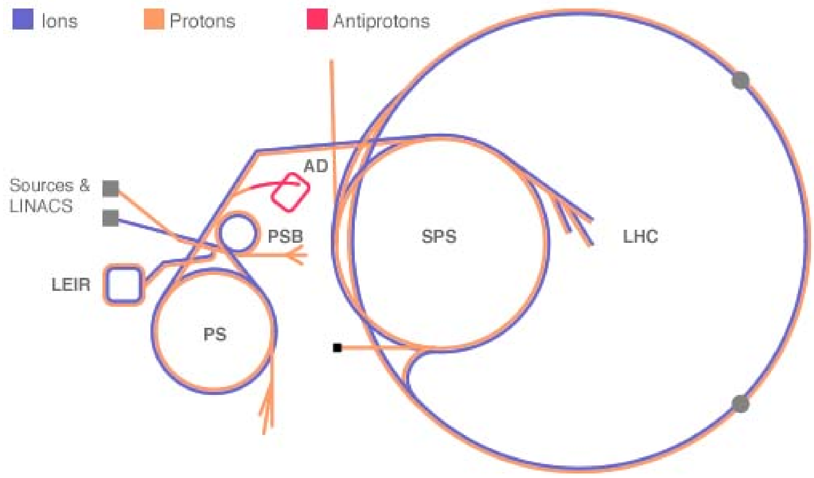

Figure 1.2: LHC proton and ion injection chain

At the nominal intensity, the bunch spacing in the LHC will be 7,48 m in space and 25 ns in time giving an interaction rate of 40 MHz. Each of the two beam pipes will be filled with 2.808 bunches. At the start of the nominal fill each bunch consists of $1{,}15 \cdot 10^{11}$ protons. At the interaction points the transverse bunch radius will be squeezed down to 16 μm in order to increase the probability of a collision. The focusing and bending of the beams on each other is shown in Figure 1.3. The bunch length of 30 cm leads to a effective distribution of the vertex position along the beam axis of 5,5 cm (rms). The beams will be stored in the ring for about 10 to 20 hours before being dumped and the next insertion starts. More details can be found in [4].

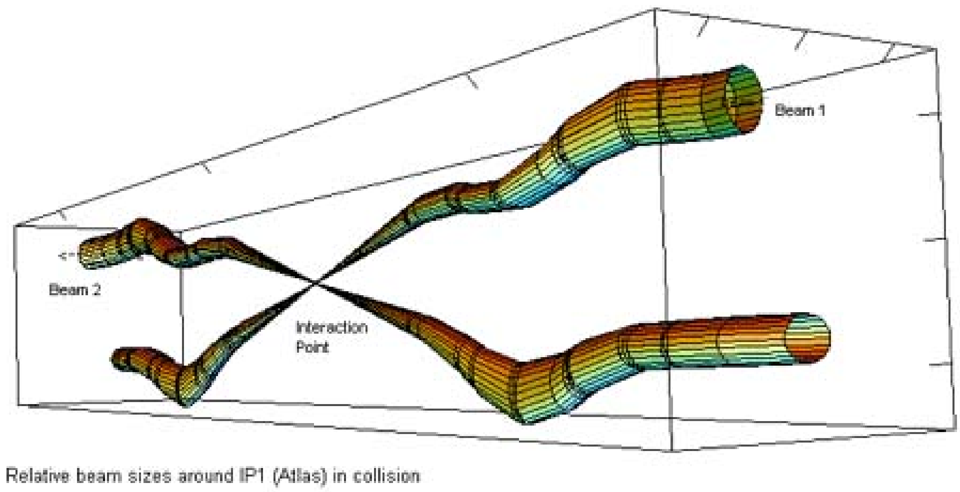

Figure 1.3: Simulation of the relative beam sizes around interaction point 1 (Atlas).

1.1.1 2007-2008

In this section, the expected evolution of the LHC performance parameters during the years 2007 and 2008 is given. More detailed information can be found in [4].

In November 2007 the so-called calibration run will be performed to align the LHC components and to bring the beams on their foreseen lines. This includes the first injection of two beams simultaneously into the LHC with the aim to establish collisions at a centre of mass energy of 900 GeV. The main goals during this run are to establish a good understanding of the machine and to properly commission the safety systems. If things go well, machine development could see single beams ramped up to centre of mass energy of 1,1 TeV, which would be a new world record for proton beam energy.

In 2008 the full commissioning to 7 TeV will take place, following a staged approach:

- Stage 1
  Initial commissioning with the goal to bring moderate intensities into collision for the first time. Also including the commissioning of the LHC cycle with low intensity beams and the move to a two-beam operation. The first collisions will be un-squeezed, followed by a partial squeeze in this stage.

St 1	bunches	β^* $[m]$	bunch intensity	Luminosity $[cm^{-2}s^{-1}]$	event rate per crossing
start	43 × 43	18	$3 \cdot 10^{10}$	$3,8 \cdot 10^{29}$	0,05
end	156 × 156	4	$9 \cdot 10^{10}$	$5,6 \cdot 10^{31}$	1,9

  At the end of this stage it would be possible to reach a luminosity of $1,1 \cdot 10^{32}$ with 156 bunches per beam, but the experiments requested maximum event rate per crossing of around 2 would be exceeded, implying the need to move to a bunch spacing of 75 ns (stage 2).

- Stage 2
  At first the machine protection needs to be fully commissioned. Then the aim is to move to a bunch spacing of 75 ns with intensities of about 4-$6 \cdot 10^{10}$ particles per bunch. The squeeze, only partially commissioned at this stage, needs to be pushed to 2 m, with the associated control of key beam parameters.

St 2	bunches	β^* $[m]$	bunch intensity	Luminosity $[cm^{-2}s^{-1}]$	event rate per crossing	% total I
start	936 × 936	10	$4 \cdot 10^{10}$	$2,3 \cdot 10^{31}$	0,13	0,12
end	936 × 936	1	$6 \cdot 10^{10}$	$5 \cdot 10^{32}$	2,9	0,17

  In this stage one can push a long way toward nominal configuration in terms of bunch currents and β^* before moving to excessive event rates, while keeping the total current at 10% to 15% of nominal.

- Stage 3
  In this stage it is foreseen to move the bunch spacing to 25 ns with the aim of moving to intensities around 4-6$\cdot 10^{10}$ particles per bunch. In phase 2 of this step a long shutdown for collimation and for the installation of additional beam dump dilutors is foreseen.

St 3	bunches	β^* $[m]$	bunch intensity	Luminosity $[cm^{-2}s^{-1}]$	event rate per crossing	% total I
start	2808 × 2808	4	$4 \cdot 10^{10}$	$1,7 \cdot 10^{32}$	0,32	0,35
end	2808 × 2808	0,55	$6 \cdot 10^{10}$	$2,8 \cdot 10^{33}$	5,2	0,52

- Stage 4
  In this stage design intensity and full squeeze will be reached with the nominal 25 ns bunch spacing.

St 4	bunches	β^* $[m]$	bunch intensity	Luminosity $[cm^{-2}s^{-1}]$	event rate per crossing
start	2808 × 2808	2	$8 \cdot 10^{10}$	$1,4 \cdot 10^{33}$	2,6
end	2808 × 2808	0,55	$1,15 \cdot 10^{11}$	$1,0 \cdot 10^{34}$	19,3

1.2 Physics at LHC

Search for the Standard Model (SM) Higgs Boson

The Higgs mechanism is a cornerstone of the Standard Model (SM) and its supersymmetric extensions. Due to spontaneous symmetry breaking the electroweak gauge bosons W and Z as well as the fermions acquire masses through the interaction with the Higgs field. In the Standard Model one weak isospin Higgs doublet is introduced and leads to the existence of one elementary Higgs particle. The Higgs couplings to the electroweak gauge bosons and all fermions grow with their masses. The only unknown parameter of the Higgs boson itself is the value of its mass m$_H$. Former particle physics experiments combined with theoretical considerations could only constrain the mass of the Higgs boson between 114,4 GeV/c^2 and 1 TeV/c^2 as summarised in [5]. The search for the Higgs boson is a crucial endeavour for establishing the standard formulation of the electroweak theory.

On the right side of Figure 1.4 the full QCD-corrected results for the gluon fusion $gg \to H$, vector boson fusion $qq \to VVqq \to Hqq$, vector boson bremsstrahlung $q\overline{q} \to V^* \to HV$ and associated production $gg, q\overline{q} \to Ht\bar{t}, Hb\bar{b}$ are shown. More details can be found in [6].

Depending on the Higgs mass m_H, different decay channels, as shown on the left side of Figure 1.4, can be exploited for a discovery as listed in table 1.2.

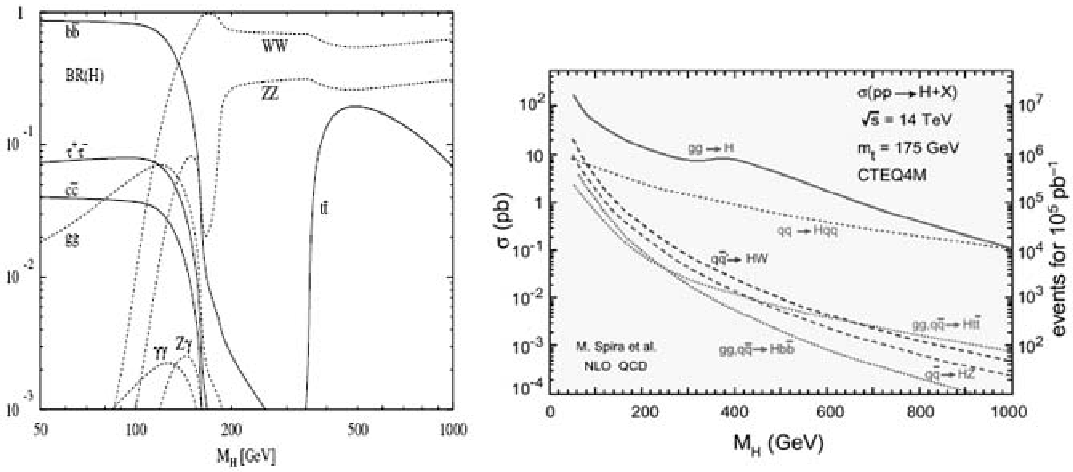

Figure 1.4: On the left side, the branching ratios of the dominant decay modes of the SM Higgs particle are shown. In this plot all relevant higher-order corrections are taken into account. The right plot shows the Higgs production cross sections at the LHC [$\sqrt{s} = 14\ TeV$] for the various production mechanisms as a function of the Higgs mass. [6]

Mass range	Decay channel
$100\ GeV \leq m_H \leq 150\ GeV$	$H \to \gamma\gamma$
$90\ GeV \leq m_H \leq 120\ GeV$	$H \to b\bar{b}\ in\ t\bar{t}H$
$130\ GeV \leq m_H \leq 200\ GeV$	$H \to ZZ^* \to 4l$ (e or μ)
$140\ GeV \leq m_H \leq 180\ GeV$	$H \to WW \to l\nu l\nu$
$200\ GeV \leq m_H \leq 750\ GeV$	$H \to ZZ \to 4l$
$500\ GeV \leq m_H \leq 1\ TeV$	$H \to ZZ \to 2l2\nu$
$m_H \approx 1\ TeV$	$H \to WW \to l\nu + 2Jets$
$m_H \approx 1\ TeV$	$H \to ZZ \to 2l + 2Jets$

Table 1.2: Experimentally accessible Higgs decay channels as function of mass. [7]

Search for Supersymmetric (SUSY) Particles

Supersymmetry (SUSY) is one of the best-motivated candidates for physics beyond the Standard Model. Low-energy SUSY is well-motivated since it stabilizes the electroweak scale. It provides quantitatively accurate unification of gauge couplings as well as a promising candidate for the cold dark matter theory. Moreover it is consistent with electroweak precision data. Since the mechanism of SUSY breaking is unknown, supersymmetric extensions of the Standard Model contain a large number of unknown parameters, alone 105 in the Minimal Supersymmetric Standard Model (MSSM). Specific assumptions on the SUSY-breaking mechanism, in particular about the unification of parameters at the grand-unification (GUT) scale, considerably reduce the number of free parameters. For example in the constrained MSSM (cMSSM) we end up with only four new parameters (and one sign) specified at the unification scale. Experiments at the Large Hadron Collider (LHC) will have not only to discover SUSY but also to determine precisely the underlying SUSY-breaking scenario with as few theoretical prejudices as possible. More information about the search of SUSY particles can be found in [8].

If SUSY particles exist, they will be produced and detected at the LHC. The lightest SUSY particle is stable but hardly interacts with matter. Therefore the search for supersymmetric particles will base itself on the hermeticity of the detectors and their ability to identify missing transverse energies.

Search for Extra Dimensions

Like described in [9] the Large Hadron Collider will be a black hole factory. TeV scale gravity scenarios predict a possibility of producing black holes and observing their decay products directly at the LHC. It is predicted, that such higher dimensional black holes could lead to spectacular decays involving the production of fundamental particles such as leptons, photons, neutrinos, W, Z, jets, etc. The resulting production and kinematic distributions could allow the determination of the Hawking temperature, the mass of black holes, the number of extra dimensions, etc.

CP Violation

Basically described, CP Violation is about the question why the universe exists out of matter and not out of antimatter. Experimentally we are sure that less than 0.01% of the universe consists out of antimatter. There must be a mechanism why there became more matter than antimatter. According to current thinking the surplus of matter could be explained if a very heavy gauge boson (the X boson) exists, which decays in a way that violates CP. In between parenthesis, this would also lead to a finite lifetime of the proton.

The LHC-b experiment is designed to perform high-precision CP violation measurements in the B-meson system. The tagging of neutral B mesons and to find their flavour at production is essential for many CP asymmetry measurements. A detailed summary of flavour physics and CP violation at LHC is given in [10].

Heavy Ion Physics

The colliding of heavy ions like lead will open the possibility to explore the regions of a new state of matter. The collisions will compress and heat the ion nuclei so that their individual protons and neutrons overlap. The high energy and particle density creates a local volume, where, for a short time, a relatively large number of unbounded quarks and gluons can exist. This form of matter, where no confinement exists, is called quark-gluon plasma. It is thought that this plasma has existed ten millionths of a second after the Big Bang, at a time before confinement and the baryogenesis started. In addition to simulating the very early Universe, more insight in the physics of high density stars can be gained by studying heavy ion collisions. While the quark-gluon plasma expands it cools down and hadronisation starts. During the hadronisation different kinds and ratios of particles than in normal collisions are produced. These signatures can be calculated in the Quantum Chromo Dynamic (QCD). A review of the physics prospects for relativistic heavy ion collisions at the LHC is given in [11].

Beyond the Standard Model

The LHC will also allow studies of QCD, electroweak, and flavour physics. Precision studies can give indications for physics beyond the SM, providing complementary information with respect to direct searches. As an example, extensive tests of QCD will be possible through the measurement of the production of jets and direct photons with transverse energies of up to 3-4 TeV. The validity of the QCD will be tested on the transition from soft to hard scattering of protons where at present mostly phenomenological models are used. Top quarks will be produced at the LHC with a rate measured in Hz as displayed in [12]. This gives the opportunity to test the SM couplings and the spin of the top quark and the ability to provide good identification of b-jets in the decays. Also the fermi coupling for the weak interaction can be derived at high precision when measuring the lifetime of muons. An elementary review of the models and phenomenology for physics beyond the Standard Model with an emphasis on LHC physics is given in [13]

Chapter 2

CMS Experiment

The Compact Muon Solenoid (CMS) shown in Figure 2.1 is designed as a multi-purpose experiment with an emphasis on Higgs research. The whole expected mass range of the Higgs from 80 GeV/c^2 to 1 TeV/c^2 will be covered by the experiment. Many experimental signatures are possible, involving high transverse energy muons, electrons, photons and jets. In order to cleanly detect these signatures the identification and precise measurement of them over a large energy scale and at high luminosities is essential.

The detector requirements for CMS to meet the goals of the LHC physics program is described in detail in [12] and can be summarized as follows:

- Good muon identification and momentum resolution over a wide range of momenta in the region $|\eta|$[1] $< 2{,}5$ with a good muon mass resolution of approximately 1% at 100 GeV/c^2. The ability to determine unambiguously the charge of muons with p < 1 TeV/c.

- Good charged particle momentum resolution and reconstruction efficiency in the inner tracker. Efficient triggering and offline tagging of τ's and b-jets, requiring pixel detectors close to the interaction region.

- Good electromagnetic energy resolution, good photon and electron mass resolution of approximately 1% at 100 GeV/c^2 within a wide geometric coverage of $|\eta| < 2{,}5$. Measurement of the direction of photons and/or correct localization of the primary interaction vertex, π^0 rejection and efficient photon and lepton isolation at high luminosities.

- Good missing transverse energy (E_T^{miss}) and jet mass resolution, requiring hadron calorimeters with a large hermetic geometric coverage ($|\eta| < 5$) and with fine lateral segmentation ($\Delta\eta \times \Delta\phi < 0.1 \times 0.1$).

[1]The parameter η is called pseudorapidity and defined by:

$$\eta = -ln\left(tan\frac{\alpha}{2}\right) \quad with \quad \frac{r}{z} = tan\alpha, \tag{2.1}$$

where $\alpha = 90°$ is perpendicular to and $\alpha = 0°$ coincides with the beam axis. r and z are the distances from the collision point as indicated in Figure 2.3.

The design of CMS, described in this chapter, meets these requirements. The main distinguishing features of CMS are a high-field solenoid, a full silicon-based inner tracking system, and a fully active scintillating crystal-based electromagnetic calorimeter.

2.1 CMS Detector Layout

CMS has a total mass of about 12.500 tonnes, which is double that of ATLAS, even though ATLAS has about 8 times the volume of CMS. Its Overall diameter is 15 m on a length of 21,5 m. But the outstanding attribute of CMS is its superconducting solenoid which supplies a maximum magnetic field of 4 Tesla .

CMS is divided in several subsystems that are arranged in an onion like structure around the collision point as displayed in Figure 2.1. The volume of the superconducting coil houses the tracker and the calorimeters, which consist of an electromagnetic part and a hadron part. An iron return yoke surrounds the coil and is interleaved with muon chambers. The very forward regions are also equipped with calorimeters.

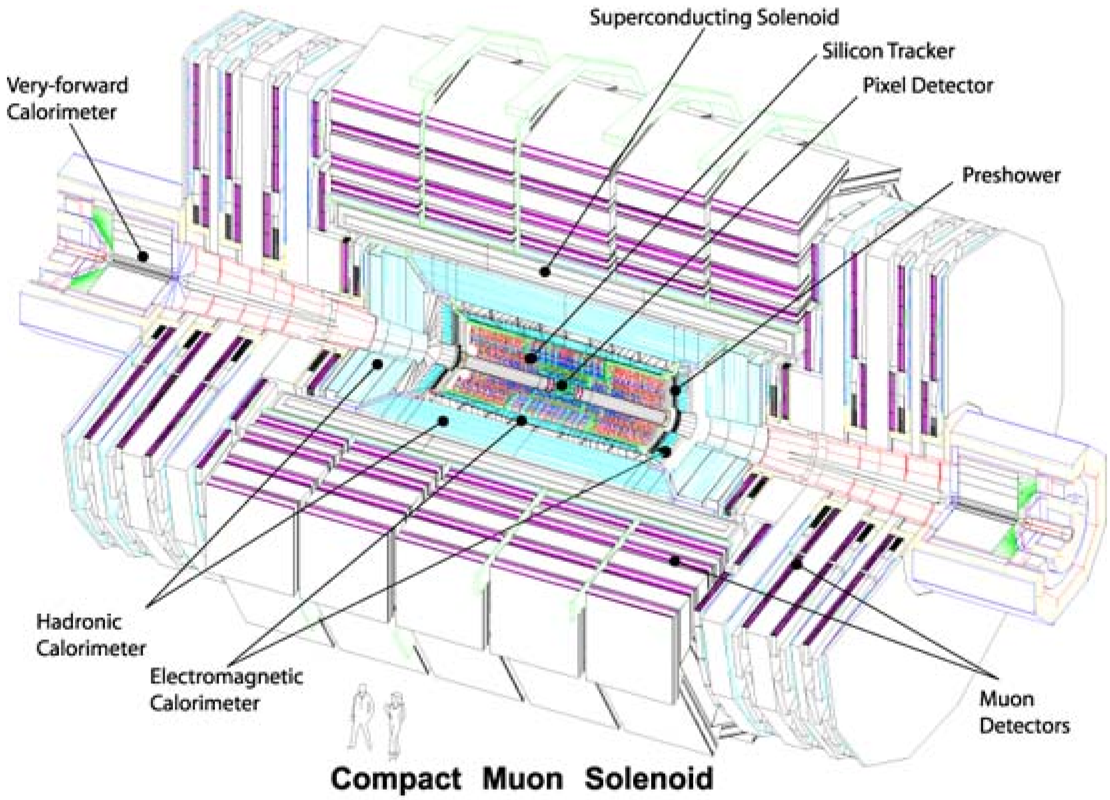

Figure 2.1: The Compact Muon Solenoid.

The CMS detector will identify the following particle types: electrons, photons, hadrons, muons, and neutrinos or neutrino-like particles. Table 2.1 gives an overview of the different subsystems and which particles they can detect. This is also graphically displayed in Figure 2.2. Neutrinos and neutrino-like particles,

	electrons	photons	pions	neutrons	muons
Tracker	×		×		×
ECAL	×	×	×		×
HCAL			×	×	×
Muon System					×

Table 2.1: Types of particles which can be detected by the differenct detector systems of CMS. ECAL and HCAL stand for electromagnetic and hadronic calorimeters, respectively.

for example neutralinos arising in supersymmetric theories, can only be observed indirectly, since they only interact very weakly with the detector material. Their presence can only be deduced when the so-called missing transverse energy (E_T^{miss}) differs from zero. This is the main reason, why a hermetic coverage of the detector systems is extremely important.

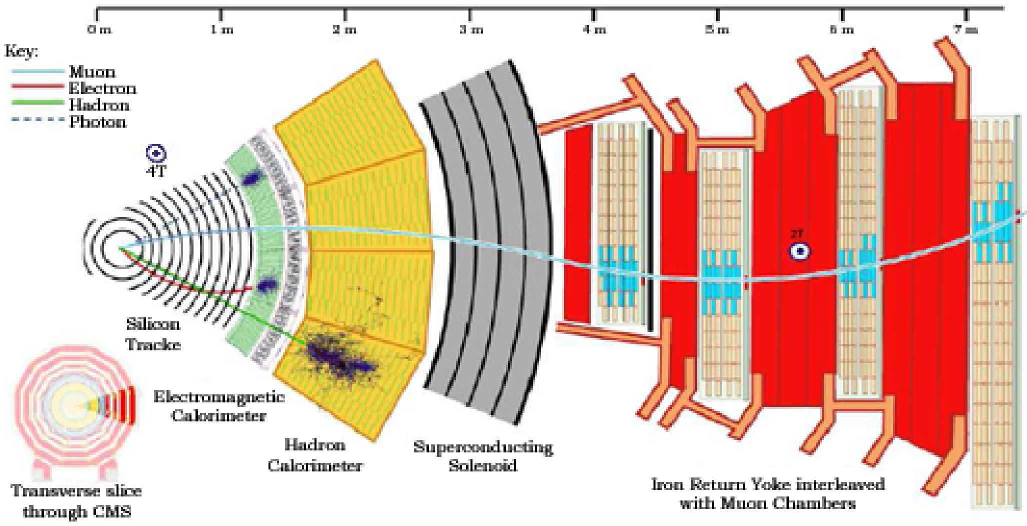

Figure 2.2: How the different particles pass through CMS.

2.2 Tracker

The Tracker is the innermost part of the detector. Its main function is to determine the trajectories of charged particles. Since the tracker sits inside the magnetic field of the detector, the Lorentz force curves the trajectories of charged particles moving through it. Out of the curvature the momentum and the electric charge of these particles can be derived. In addition, high resolution pixel detectors close to the collision point help to reconstruct the position of vertices. This helps to distinguish between primary and secondary vertices and is the only possibility to identify particles with very short lifetimes, which decay immediately after their genesis.

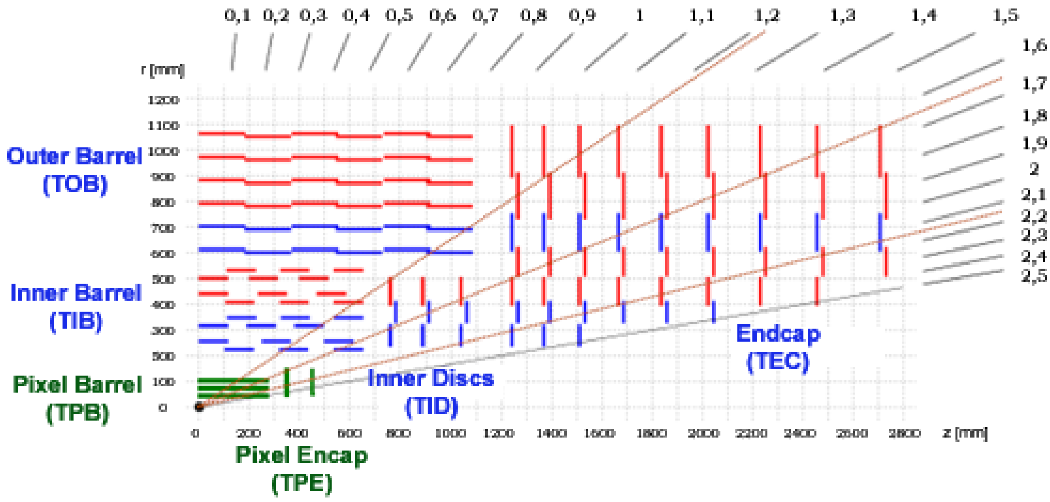

Figure 2.3: 1/4 of the z view of the CMS Silicon Tracker. On the plot's x-axis the z-axis of the detector in *mm* and on the plot's y-axis the radius in *mm* from the interaction point are indicated. The TOB consists of 6 layers including 5.208 silicon modules, the TID of 4 layers with 2.724 modules, the TID of 2×3 discs with 816 modules and the TEC consists of 2×9 discs containing 6.400 modules. In red singles sided and in blue double sided module layers are displayed.

The CMS collaboration decided to use an all-silicon solution for the tracker. In total the CMS tracker implements 24.244 silicon strip sensors covering an area of about 210 m^2. The sensors are connected to about 75.000 APV chips, which have to control approximately 9.600.000 electronic readout channels. All in all about 26 million microbonds are needed to connect these parts. More details and plots can be seen in [14].

One quarter of the detector layout can be seen in Figure 2.3. Close to the collision point, in the barrel region, 3 layers of hybrid pixel detectors are located at radii of 4, 7, and 11 cm. The size of the pixels is 100 × 150 μm^2. In the barrel part, the silicon microstrip detectors are placed at radii between 20 and 110 cm. The forward region has 2 pixel and 9 microstrip layers in each of the 2 endcaps (TEC for Tracker EndCap). The barrel part is separated into an inner barrel (TIB for Tracker Inner Barrel) and an outer barrel (TOB for Tracker Outer Barrel). To avoid very shallow track crossing angles, the TIB is shorter than the TOB, and there are an additional 3 inner disks (TID for Tracker Inner Disc) in the transition region between the barrel and endcap parts, on each side of the inner barrel. The different technologies used in the CMS Tracker to match the specifications for radiation hardness and detector occupancy are listed in Table 2.2.

Pixel Detector

The pixel detector provides high-resolution and three-dimensional patterns of space points using small silicon cells, the so-called pixels. It occupies the innermost region, close to the interaction point. It consist of three barrel layers and two

distance from beamline	fluence [$n_{eq}\ cm^{-2}$]	technology
<20 cm	10^{15}	n^+-type pixels on 270 μm thick n-type bulk, low resistivity (≈2 KΩcm), oxygenated
20 - 50 cm	10^{14}	p^+-type strips on 320 μm thick n-type bulk, low resistivity (≈2 KΩcm), pitch ≈80 μm
>50 cm	10^{13}	p^+-type strips on 500 μm thick n-type bulk, high resistivity (≈5 KΩcm), pitch ≈200 μm

Table 2.2: The different silicon technologies used in the CMS Tracker to match the specifications for radiation hardness and detector occupancy.

additional endcap discs on each side which cover the shallow angles as displayed in Figure 2.4. Each pixel module consists of a 250 μm thin, segmented sensor plate. The cell size in the pixel detector is 150 $\times$ 150 μm^2. The pixels are n^+ on n devices and are bump bonded to highly integrated readout chips as shown in Figure 2.5. The large Lorentz effect (in this region the Lorentz angle is 23°) improves the $r - \phi$ resolution through charge sharing in the two barrel layers. To benefit from the Lorentz effect the endcap discs are assembled in a turbine like geometry with blades rotated by 20°. The measured spatial resolution is about 10 μm for the $r - \phi$ measurement and about 20 μm for the z measurement.

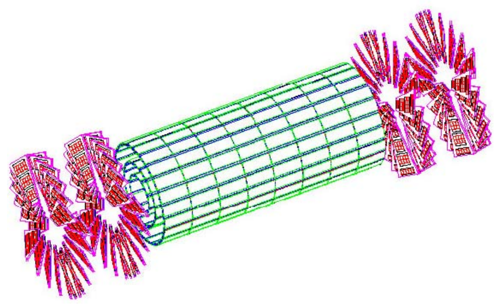

Figure 2.4: The pixel detector.

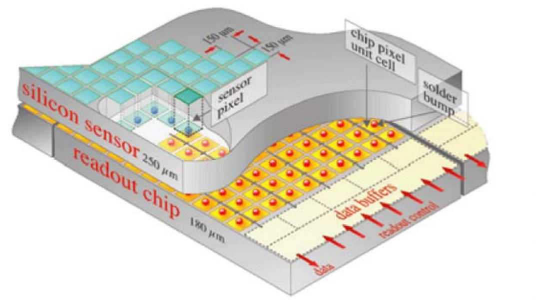

Figure 2.5: Schematic vie of a pixel detector element.

Microstrip Detector

Around the pixel detector, several layers of single- and double-sided silicon microstrip detectors will be mounted, see Figure 2.3. This enables to track the particles over a large volume with high accuracy. This outer part of the tracker will be discussed in detail in chapter 3.

Tracker Material Budget

The CMS Tracker consists of both, sensitive and non-sensitive volumes. To operate the Tracker for example low-voltage power is required and a huge amount of heat needs to be dissipated. Therefore, a large fraction of the tracker material consists of electrical cables and cooling services. The other non-sensitive parts are support structures, electronics, the beam-pipe and the thermal screen outside the tracker. All this accumulates so that the tracker material budget exceeds the equivalent of one radiation length for certain regions of η. This affects both hadron and lepton reconstruction. The decomposition of the tracker material in terms of radiation lengths and interaction lengths versus η for the different parts of the Tracker is shown in Figure 2.6.

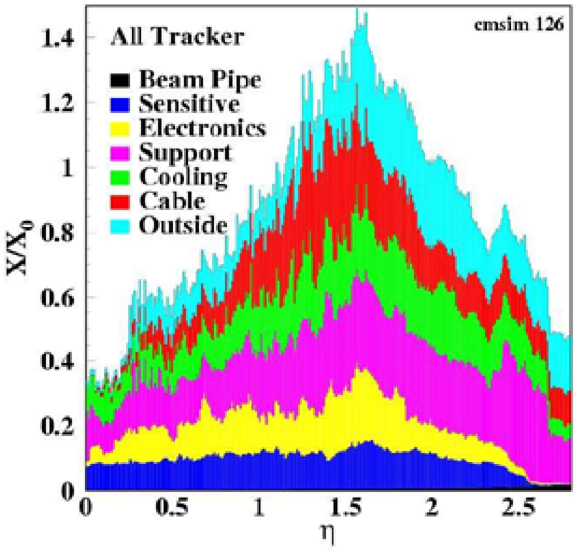

Figure 2.6: The sensitive volumes take a small part in the total Tracker material budged, which is dominated by services.

2.3 Calorimeter

The second closest subsystems to the beam are the Electromagnetic Calorimeter (ECAL) and the Hadron Calorimeter (HCAL). Except for a very small part of the HCAL, both are located inside the superconducting solenoid which surrounds the Tracker. The calorimeters will play a significant role in exploiting the physics potential offered by the LHC. Their main functions are to precisely measure the energy of photons, electrons and jets, and to provide hermetic coverage which is essential to measure the missing transverse energy. In addition, good efficiency for electron and photon identification as well as excellent background rejection against hadrons and jets are required. Furthermore a good separation of τ-hadronic decays from normal QCD jets is desired.

Electromagnetic Calorimeter

The Electromagnetic Calorimeter (ECAL) is a hermetic, homogeneous calorimeter which comprises 61.200 lead tungstate ($PbWO_4$) crystals in the central barrel part and 7.324 crystals in each of the 2 endcaps. It is designed to measure the energies of electrons and photons with high precision. All details of the ECAL can be found in [15]. Figure 2.7 shows the different systems of the ECAL.

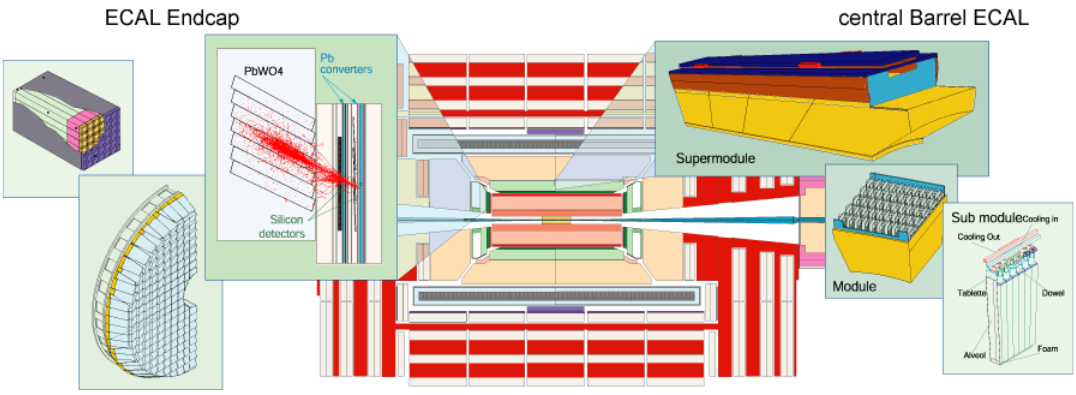

Figure 2.7: The CMS with an enlargement of the Electromagnetic Calorimeter.

The crystals, that were specially designed for the CMS ECAL, have a fast scintillation time of about 15 ns, a short radiation length of 0,89 cm, a small Molière radius of 2,2 cm and are very radiation hard. The small Molière radius allows a good separation of adjacent showers. The comparably small light yield is amplified by avalanche photodiodes in the barrel and vacuum phototriodes in the endcaps.

The ECAL plays an essential role in the investigation of the Higgs decay mode $H \rightarrow \gamma\gamma$, by detecting the two photons. This decay mode is most likely if the Higgs has a mass of less than 150 GeV/c^2, see Table 1.2. It is also important for the measurement of electrons and positrons of large transverse momenta, because these particles are clear signatures for many interesting decays (e.g. semi-leptonic t-quark decays).

Beam tests have shown that the energy resolution of the ECAL modules is excellent. Since there have been some contractual difficulties to obtain the full amount of the crystals within the time scale imposed by the LHC startup the endcap modules of the forward regions will not be included in the CMS experiment in 2007.

Hadron Calorimeter

The design of the Hadron Calorimeter (HCAL) is strongly influenced by the choice for the magnet parameters. As displayed in Figure 2.8, the HCAL is located inside the superconducting magnet and surrounds the ECAL system. Therefore not much space is available and additional scintillator layers have to be placed just outside the coil. The HCAL is made of active material inserted between copper absorber plates. The absorber plates are 5 cm thick in the barrel (HB) and 8 cm thick in

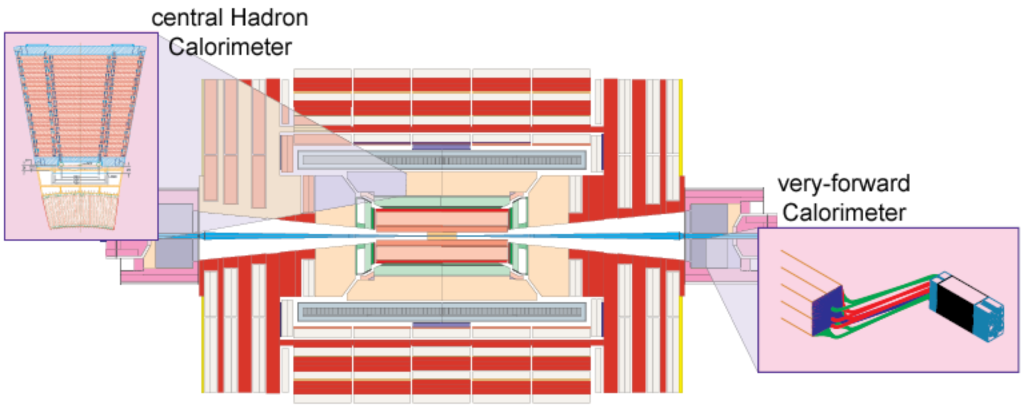

Figure 2.8: The CMS with an enlargement of the central HCAL (barrel and endcap) and the very forward calorimeter.

the endcaps (HE). The active elements of the entire central hadron calorimeter are 4 mm thick plastic scintillator tiles which are read out with wavelength-shifting plastic fibers that guide the signals to the readout electronic.

At each end of the CMS detector two additional very-forward calorimeters (HF) are located 6 m downstream of the HCAL endcaps. This region is a very high radiation and a very high rate environment. The HF covers the region 3,0 $< |\eta| <$ 5,0 and uses quartz fibers, embedded in a copper absorber matrix, as the active medium. Because of the quartz fibers it is predominantly sensitive to Cerenkov Light from neutral pions. This leads to its unique and desirable feature of a very localized response to hadronic showers.

The HCAL measures the energy and position of strongly interacting hadrons such as protons, neutrons, pions and kaons. Hadronic showers start to develop later and have larger longitudinal and lateral dimensions than electromagnetic ones. Therefore the HCAL has to be thicker than the ECAL to absorb the same amount of energy.

2.4 Superconducting Magnet

The single most important aspects of the overall detector design are the decisions on the magnetic field parameters, which are especially important for the measurement of muon momenta. The superconducting coil, displayed in Figure 2.9, surrounds the Calorimeters and the Tracker. The coil is 13 m long with an inner diameter of 5,9 m and consists of refrigerated superconducting niobium-titanium[2] filaments embedded in a matrix of solid copper. It is the largest superconducting magnet system ever build in the world, with a total weight of about 12.000 tons.

[2] Nb_3Ti is used as a type-II superconductor wire with a critical temperature of 10 Kelvin and a critical magnetic field of 15 Tesla. The niobium-titanium is formed into filaments finer than human hair and embedded in a matrix of solid copper. Fine filaments are advantageous because current flows only within a skin-depth of the surface of a superconductor. The copper matrix forms a solid mechanical structure which also carries the current, if the superconducting phase gets lost. More details about superconductors can be found in [17].

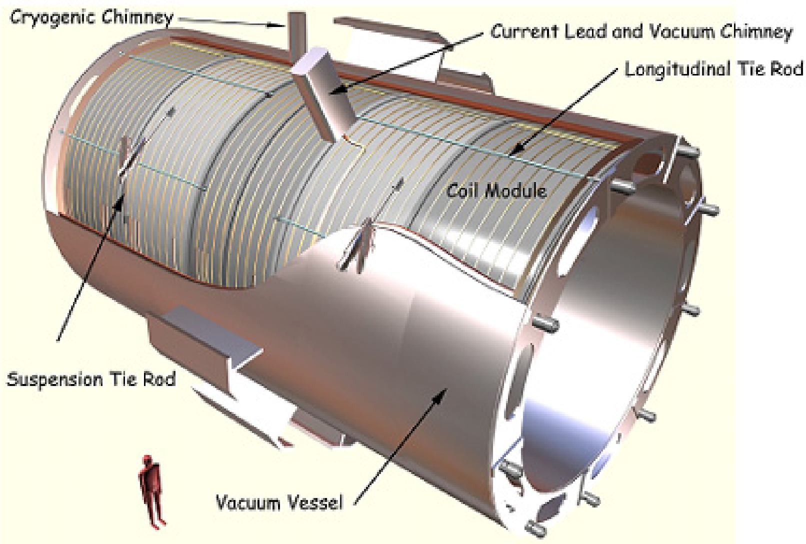

Figure 2.9: The CMS Superconducting Solenoid Coil.

In order to achieve good momentum resolution within a compact spectrometer, without making stringent demands on muon-chamber resolution and alignment, a high magnetic field of 4 Tesla was chosen. The reason for this is, that the measurement of the momentum of charged particles is based on the bending of their trajectories. The main parameters of the solenoid are given in Table 2.3.

Field	4 T
Inner Bore	5,9 m
Length	12,9 m
Number of Turns	2.168
Current	19,5 kA
Stored energy	2,7 GJ
Hoop stress	64 atm

Table 2.3: Parameters of the CMS Superconducting Solenoid.

Like in previous constructed large solenoids, e.g. ALEPH[3] and DELPHI[4] at LEP, a high-purity aluminium-stabilised conductor and indirect thermosiphon cooling, together with full epoxy impregnation, are used. Due to the large increase in some parameters as magnetic field, some changes were necessary. In particular a four-layer winding has been adopted, using a novel conductor with a larger cross-section, that can withstand an outward pressure (hoop stress) of 64 atmospheres. The conductor is a compound structure and carries a current of 20 kA. It is build of twenty continuous lengths, where each has a length of 2,65 km. Each of the 5 coil modules is made of four lengths wound together. These modules were assembled and connected together in the underground area at Point 5.

[3]ALEPH: Apparatus for LEP Physics at CERN

[4]DELPHI: DEtector with Lepton, Photon and Hadron Identification (http://delphiwww.cern.ch/)

2.5 Muon System

For the majority of the physics, LHC is designed to explore, Muons are a definite signature. Thus the ability to trigger on muons and to reconstruct their trajectories at the highest luminosities is central to the concept of CMS. There are four stations of muon chambers embedded in the 1,5 m thick saturated iron yoke. Particles arriving at the Muon System have already gone through at least 10 interaction lengths of material. Only muons and the almost non-interacting neutrinos are able to get that far.

Three different types of gaseous detectors are used to identify and measure muons, like described in detail in [18]. In the barrel region ($|\eta| < 1{,}2$) drift tube (DT) chambers are deployed. In the two endcaps ($1{,}2 < |\eta| < 2{,}4$) cathode strip chambers (CSC) are used. Additional resistive plate chambers (RPC) are positioned in both, the barrel and the endcap regions.

Drift Tubes

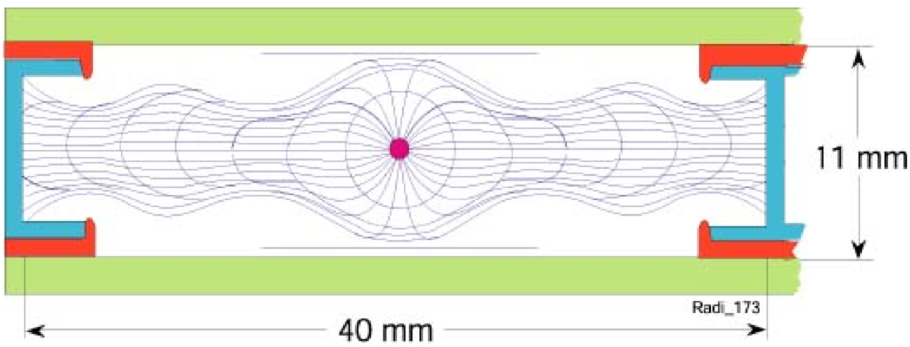

Figure 2.10: Schematic view of a Drift Tube with drawn field lines.

The 250 Drift Tubes (DT) used in the barrel region are organized in four layers. In this region the neutron induced background is small, the muon rate is low and the residual magnetic field in the chambers is low. Furthermore the Magnetic field is guided and almost fully trapped by the iron plates of the Magnet Yoke. When an ionizing particle passes through the 4 cm breadth tube it liberates electrons which move along the field lines to the wire, which is at positive potential. The exact coordinate of the particle is obtained with high precision time measurements.

Cathode Strip Chambers

In the two endcap regions of the Muon System, where the magnetic field, the muon rate and the neutron induced background rate are high, 468 Cathode Strip Chambers (CSC) are deployed. CSCs are multiwire proportional chambers in which one cathode plane is segmented into strips running across wires. Since the wires give the radial coordinate whereas the strips measure ϕ, the two coordinates can be obtained simultaneous. The third coordinate is given, because each CSC

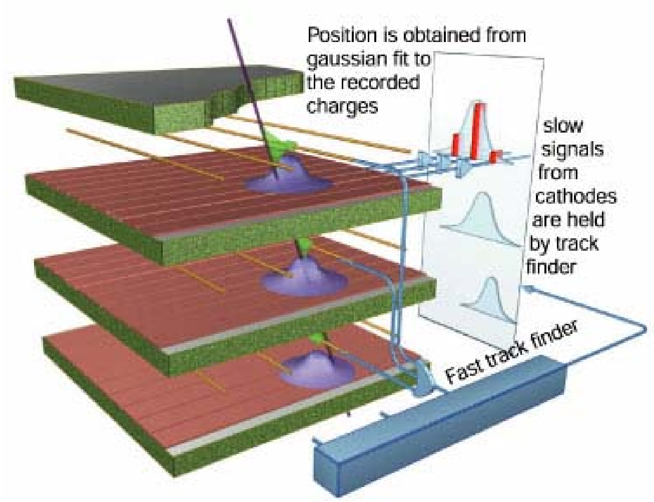

Figure 2.11: Schematic view of a CSC chamber, with a sketch of the mechanism of signal detection.

module contains six layers. Alongside a precise space and time measurement, the closely spaced wires make the CSC a fast detector suitable for triggering.

Resistive Parallel Plate Chambers

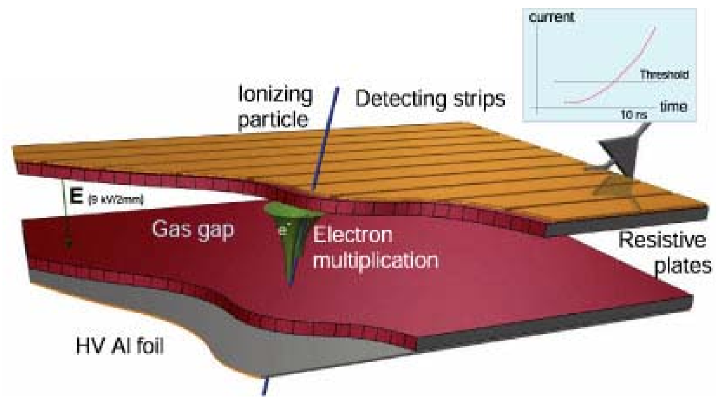

Figure 2.12: Schematic view of a RPC chamber, with a sketch of the signals time evolution.

Resistive Parallel Plate Chambers (RPC) are used in both the barrel and the endcap regions of the CMS Muon System. They are fast gaseous detectors which combine a good spatial resolution with a time resolution of 1 ns. To ensure good operation at high rates they are operated in avalanche modus. Since the RPCs are parallel plate counters with the two electrodes made of very high resistivity plastic material, the construction and operation of very large and thin detectors is possible. As one can see in Fig. 2.12 the signals are picked up by external strips.

Chapter 3

CMS Silicon Strip TEC Modules

At first the principle of silicon sensors and their main characteristics are described. Afterward a closer look at the design choices for the Tracker End Cap (TEC) silicon modules are given. A consolidated knowledge about the effects on silicon due to radiation damage is important to understand the change of the CMS silicon sensor's behavior during their life time in LHC. Also the different components which are gathered around the silicon to form the complete TEC-modules are introduced.

To complete the CMS Tracker End Caps 6.400 silicon microstrip modules in 10 different geometries, like displayed in Figure 3.1, are needed. Including spares, in total more than 7.200 TEC modules were built by 14 different institutes in Europe and the United States.

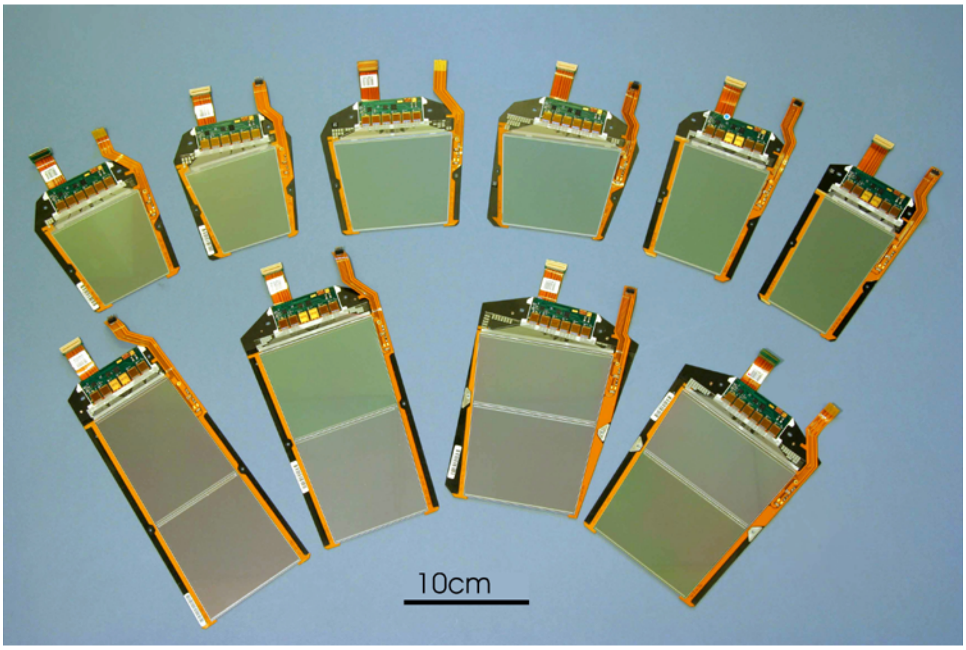

Figure 3.1: Picture of the 10 mechanically different TEC module geometries. Upper row from left to right: R1N, R1S, R2N, R2S, R3N and R4N (including alignment modules R4A); lower row from left to right: R7N, R6N (including alignment modules R6A), R5S and R5N. (R...Ring, N...Normal, S...Stereo, A...Alignment)

3.1 Silicon Sensors

3.1.1 Advantages and Disadvantages of Silicon

Compared with other materials, silicon has unique physical properties that makes it suitable for the use in high energy physics. The most important features of silicon, resp. silicon detectors, are summarized here:

- In average only the small energy of 3,65 eV is needed to create an electron-hole pair. This leads to a large number of charge carriers per unit length of silicon material created by an ionizing particle. This small energy is related to the value of the silicon band gap[1] of 1,12 eV at $300°K$, slightly increasing with lower temperatures. A Minimum Ionizing Particle (MIP) traversing 300 μm of silicon at $300°K$ produces about 22.500 electron-hole pairs. In comparison to gaseous detectors, in silicon the ionizing energy is an order of magnitude lower and the number of created carriers is substantially higher.

- Due to the high density of silicon (2,33 g/cm^3) a particle traversing the detector loses more energy per unit length than for instance in gaseous detectors. This allows to build thin detectors, that still produce large enough signals for a precise measurement, which minimises multiple scattering and the number of δ-electrons.

- The mobility of electrons (1.450 cm^2/Vs) and holes (450 cm^2/Vs) at room temperature is influenced by doping. This dependence is very moderate in a large range of concentrations where carriers can move almost as free particles inside the silicon. This effect results in rapid collection of charge carriers ($\approx$10 ns) and thus enables to use the detectors in such high-rate environments like the LHC.

- Silicon wafers are mechanically rigid, which easies the handling of the sensors a lot. A secondary advantage of this stiffness is, that no complex additional supporting structures, which would increase the Tracker material budget even more, are needed.

- Another advantage of silicon is its radiation hardness, which enables the use of the silicon tracker that close to the collision point.

- The biggest disadvantages of silicon is its high cost.

[1]The band gap, or energy gap is the energy difference between the top of the valence band and the bottom of the conduction band in insulators and semiconductors.

3.1.2 Energy Loss

A particle crossing matter interacts with the electrons and the nucleons of its atoms. This is the fundamental principle of all particle detectors. In the case of silicon detectors the energy loss of charged particles due to the excitation of atomic electrons is used. The energy loss of moderately relativistic charged particles in matter was first described by H.A. Bethe and F. Bloch as displayed in [19]:

$$-\frac{dE}{dx} = Kz^2\frac{Z}{A}\frac{1}{\beta^2}\left[\frac{1}{2}ln\left(\frac{2m_ec^2\beta^2\gamma^2T_{max}}{I^2}\right) - \beta^2 - \frac{\delta}{2}\right] \tag{3.1}$$

$$K = 4\pi N_A r_e^2 m_e c^2 \tag{3.2}$$

$$T_{max} = \frac{2m_ec^2\beta^2\gamma^2}{1 + \frac{2\gamma m_e}{M} + \left(\frac{m_e}{M}\right)^2} \tag{3.3}$$

N_A, Z and A are the Avogadros constant, the atomic number and the atomic mass of the traversed matter, m_e and r_e are the electron mass and its classical radius and z_e is the incident particles charge. T_{max} is the maximum kinetic energy which can be imparted to a free electron in a single collision, I is the mean excitation energy, $\beta = v/c$, $\gamma = (1-\beta^2)^{-\frac{1}{2}}$ and M is the mass of the incident particle. δ represents the correction to the density effect[2].

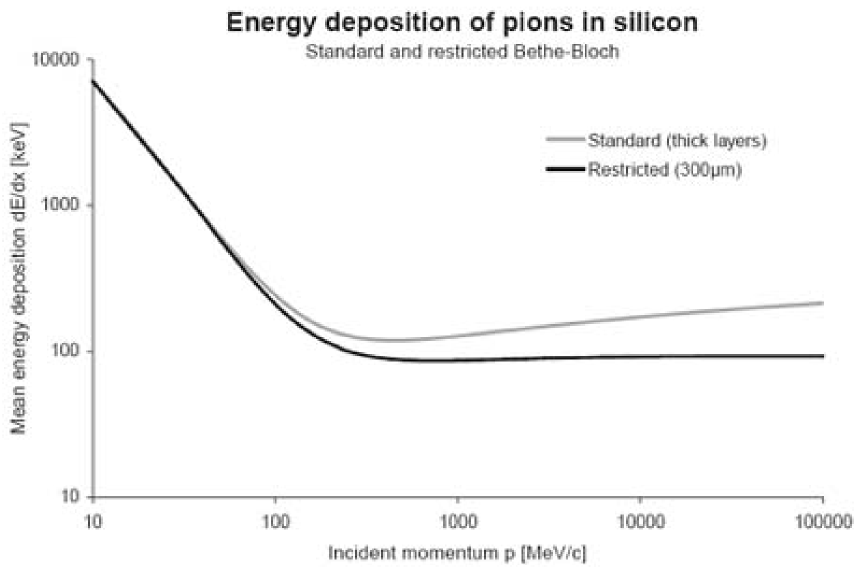

Figure 3.2: Energy deposition of pions in silicon. While the standard Bethe-Bloch theory covers thick layers, restrictions apply to thin layers as shown for 300 μm to account for energy carried off by energetic knock-on electrons. [20]

Silicon with a thickness of 300 to 500 μm is considered as a thin layer and fluctuations in energy loss are mainly due to the production of a few high energy knock-on electrons. In addition practical detectors often measure the energy deposited, not the energy lost. So it is more appropriate to consider the mean energy

[2]The electric field of an incident particle results in polarisation of individual atoms of material, which in turn shields the electric field of the particle.

loss excluding energy transfers greater than some cutoff T_{cut}, when a fraction of the energy is carried off by high energetic knock-on electrons:

$$-\left.\frac{dE}{dx}\right|_{T<T_{cut}} = Kz^2\frac{Z}{A}\frac{1}{\beta^2}\left[\frac{1}{2}ln\left(\frac{2m_ec^2\beta^2\gamma^2T_{upper}}{I^2}\right)-\frac{\beta^2}{2}\left(1+\frac{T_{upper}}{T_{max}}\right)-\frac{\delta}{2}\right] \quad (3.4)$$

$$T_{upper} = MIN(T_{cut}, T_{max}) \quad (3.5)$$

T_{cut} depends on the material and the incident particle momentum. In the low energy range, there is no difference between standard and restricted forms, since knock-on electron production is improbable. However, in the regime of a few hundred MeV/c, there is already considerable deviation as viewed in Figure 3.2. As described in more detail in [20], the standard theory predicts a MIP at 450 MeV/c, while the restricted energy loss states 750 MeV/c. Moreover, the relativistic rise at high energies is quite flat in the restricted model due to energy carried off by knock-on electrons.

The number of produced free charge carriers n, including electrons and holes with an energy of E_{eh} in the case of semiconductors, depends on the total energy loss E_{loss}. In the case of silicon it can be calculated via:

$$n = \frac{E_{loss}}{E_{eh}} \qquad (E_{eh} = 3,65eV\ for\ silicon) \quad (3.6)$$

3.1.3 Carrier Transport Phenomena

In semiconductor materials various transport phenomena are responsible for the movement of the charge carriers. The most important are the drift, the diffusion process and the Lorentz shift.

Drift

The drift describes the movement of electrons and holes under the influence of an external electric field $\vec{E}$. For weak electric fields, the drift velocity is linearly proportional to the applied field:

$$\vec{v} = \mp\mu\vec{E} \quad with \quad \mu_{e(h)} = \frac{1}{2}\frac{q\widehat{t}}{m^*_{e(h)}} \quad (3.7)$$

where μ is the mobility of the charge carriers which is constant in the case of weak electric fields: $\mu_e = 1.350\ cm^2/Vs$ for electrons and $\mu_h = 480\ cm^2/Vs$ for holes. q denotes the elementary charge, $\widehat{t}$ equals the average time between two collisions and $m^*_{e(h)}$ the effective mass of electrons and holes, for silicon: $m^*_e = 1{,}09m_e$ and $m^*_h = 0{,}56m_e$ whereas $m_e = 9\cdot 10^{-31}kg$.

In higher fields (above $10^4\ V/cm$) the velocity dependence on the intensity begins to depart from the linear relationship. For sufficient strong external electric fields the increasing number of collisions between the charge carriers and the crystal lattice atoms lead to a saturation of the average velocity, as displayed in Figure

3.3. As described in [21] empirical functions have been found for electrons and holes in silicon:

$$\vec{v}_e = \frac{\mu_e \vec{E}}{\sqrt{1 + (\frac{\mu_e \vec{E}}{v_{e,sat}})^2}} \tag{3.8}$$

$$\vec{v}_h = \frac{\mu_h \vec{E}}{1 + \frac{\mu_h \vec{E}}{v_{h,sat}}} \tag{3.9}$$

where $v_{e,sat} = 1,1 \cdot 10^7 cm/s$ and $v_{h,sat} = 9,5 \cdot 10^6 cm/s$ represent the saturation velocities for electrons and holes.

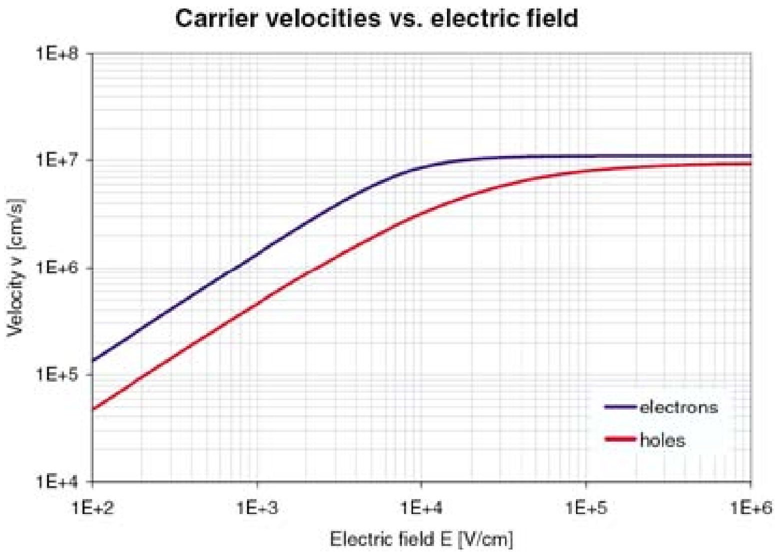

Figure 3.3: Electron and hole velocities vs. the electric field strength in silicon. [20]

Diffusion

The diffusion process is caused by existence of spatial variations of carrier distribution inside the silicon. Both electrons and holes tend to move from a region of high concentration to a region of low concentration, creating a diffusion flux, that can be expressed one dimensionally as:

$$\frac{dn}{dt} = -D_n \frac{dn}{dx} \tag{3.10}$$

where the diffusion coefficient or diffusivity D_n is related to the mobility by the Einstein relation:

$$D_n = \frac{k_B T}{q} \mu \tag{3.11}$$

In the two equations above, n stands for the number of electrons in the conduction band per unit of volume, and can be calculated via:

$$n = N_e e^{\frac{E_F - E_C}{k_B T}} \tag{3.12}$$

where N_e is the density of electrons in the conduction band, E_F represents the energy of the Fermi level, E_C the lowest energy level of the conduction band, T the temperature and k_B the Boltzmann factor.

Lorentz Shift

A magnetic field $\vec{B}$ applied to a semiconductor through which current is flowing generates an electric field perpendicular to the direction of the current flow and the magnetic field. This so called Hall effect is graphically displayed in Figure 3.4. As measured in [22], typical position resolutions of silicon strip detectors are in the order of μm, while the Lorentz shift in a 4 Tesla magnetic field reaches 200 μm for electrons inside a 300 μm thick detector. This causes an offset between the particle track and the measured position.

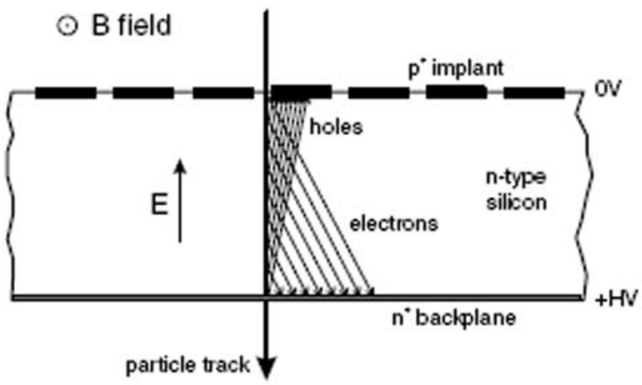

Figure 3.4: If a magnetic field perpendicular to an electric field is present the charges are deflected from their track. Since there is up to a factor of three, between electron and hole mobilities, the Lorentz angle is different for holes and electrons.

The movements of the charge carriers result in a change of their direction, described by the Lorentz angle ϑ_L:

$$tan\vartheta_L = \mu_H B \quad with \;\; \mu_H = \mu \cdot r_H \tag{3.13}$$

The Hall mobility μ_H differs from the conduction mobility μ by the Hall scattering factor r_H. Inside a CMS-like magnetic field of 4T, Lorentz angles of 31° and 8° have been measured for electrons and holes respectively in a silicon detector of 300 μm thickness, values from [22]. Also to mention is, that as a consequence of the not constant electric field near a pn-junction, the Lorentz angle changes from point to point inside the detector and the charge carriers drift along curved paths.

In practice, the relevance of the Lorentz shift is minimized by mechanically tilting the detectors so that the target areas on the electrodes, for both electrons and holes, coincide. For example in the barrel region of the CMS Tracker a tilt angle of 11,5° is used. This effect was also considered during the design of the Pixel detector as mentioned in section 2.2.

3.1.4 p-n Junction

To get a signal, the electron hole pairs created by a traversing particle have to be transformed into a current. At 300°K there are about $1,08 \cdot 10^{10}$ intrinsic charge carriers per cm^3 of silicon. This is much higher than the 22.500 electron hole pairs created by a MIP traversing 300 μm of silicon. This leads to a very bad signal to noise (S/N) ratio. This problem is avoided by reverse biasing a introduced pn-junction inside the detector. The pn-junction is the interface of p-doped and n-doped silicon:

- p-doping: A silicon atom is replaced with an acceptor atom, an atom with only three valence electrons. Thus one electron is missing in the covalent bonds and a hole is created. This change of the lattice structure is accompanied by the creation of localised energy levels in the band gap. For p-doping the energy level is found just above the valence band.
- n-doping: Replacement of a silicon atom by a donator, an atom with five valence electrons. This occurrence of an additional valence electron is called n-doping. The donor energy level is found just below the conduction band.

Via the reverse biasing a depleted zone is established, where nearly no intrinsic charge carriers are left inside the silicon. So the whole diode can be used to detect particle tracks. Typically high-resistive reverse biased diodes can be fully depleted with approximately 30 V to 600 V. After depletion free charge carriers only appear from particles ionizing this area. Now the S/N ratio is at reasonable values and the generated charge can be measured via the induced current from the charge carrier drift to the electrodes.

The full depletion voltage V_{dep} scales with the square of the detector thickness D and the inverse resistivity ρ of the silicon. When the sensor is fully depleted, the electric field is zero at the backplane and linearly increases to its maximum E_{max} at the frontside,

$$V_{dep} = \frac{D^2}{2\rho\mu_e\epsilon} \tag{3.14}$$

$$E_{max} = \frac{eND}{\epsilon} \tag{3.15}$$

where e stands for the elementary charge, N for the bulk donor density and ϵ for the dielectric constant. When the sensor is not fully depleted, the space charge zone and the electric field do not extend over the whole bulk and the charge collection is inefficient.

3.2 Radiation Damage and Type Inversion

Damage caused by radiation can be divided into two groups, surface damage and bulk damage. The energy loss by interaction of an incoming particle with matter can be divided into two parts: ionizing and non-ionizing energy loss (NIEL). Due to fast recombination of charge carriers the ionizing energy loss does not lead to long term bulk damage. NIEL contains displacements of lattice atoms and nuclear reactions, where both can result in long term bulk damage.

3.2.1 Bulk Damage

The bulk damage in silicon is mainly caused by displacements of silicon atoms in the lattice due to the non ionizing energy loss (NIEL) of hadrons and high energetic leptons respectively gammas. These displacements are for example interstitials, which are atoms between regular lattice sites, and vacancies, which are empty lattice sites. In addition, nuclear interactions like neutron capture and nucleus transmutation, secondary processes from high energetic displaced lattice atoms and defect clusters from cascade processes cause changes to the silicon lattice of the sensors. The exact damage mechanisms in silicon are mainly understood and are, for different particles, directly proportional to the amount of their non ionizing energy loss (NIEL scaling), which is displayed in Figure 3.5. Numerous experimental observations have led to the assumption, that damage effects in the silicon bulk by different energetic particles can be described as being proportional to the displacement damage cross section D. D is normally quantified in $MeVmb$, whereas the NIEL-value is given in $keVcm^2/g$. For silicon, which has an atomic mass of 28,086 g/mol, the relation between D and NIEL is: 100 $MeVmb$ = 2,144 $keVcm^2/g$. More details can be found in [25]. Both, the displacement damage cross section D and the NIEL value, are depending on the particle type and energy.

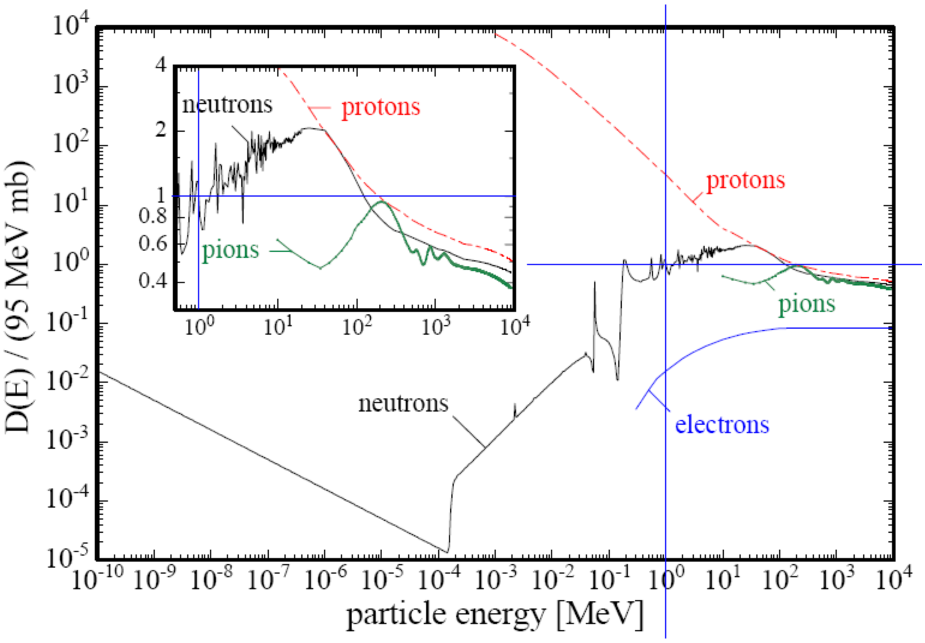

Figure 3.5: Non ionizing energy loss (NIEL) for different particles. The normalized NIEL values are plotted as function of energy. According to an ASTM (American Society for Testing and Materials) standard, the displacement damage cross section for 1 MeV neutrons is set as a normalizing value: $D_n(1MeV) = 95\ MeVmb$, marked with the blue cross. [25]

Long term effects of bulk damages can seriously threaten the operation of silicon detectors in a high radiation environment like the LHC. The three main effects of radiation damaged silicon due to non-ionizing energy loss are an increase of the leakage current, a change in the effective impurity concentration and a loss in the charge collection efficiency:

Increase of Leakage Current

The increase in bulk leakage current after radiation exposure, as displayed in Figure 3.6, is caused by an additional generation of electron-hole pairs due to bulk damages. For the operation of detectors the control of the leakage current is important in two aspects, one is the resulting higher shot noise contribution with higher leakage currents and the other is the increased heat production in the silicon bulk at increased currents. The later can lead to a thermal runaway if the silicon detector is not properly cooled. The bias leakage current I after irradiation is:

$$I = I_0 + \alpha \Phi A d \tag{3.16}$$

where I_0 is the leakage current before irradiation, α is the "current related damage rate", usually normalized to 20°C and Φ is the particle fluence given in particles per cm^2. A is the detector area and d its thickness. If temperature normalized, the damage rate α is a universal constant, not depending on the material type or the irradiating particles. Therefore α is often used to reliably monitor the accumulated particle fluence.

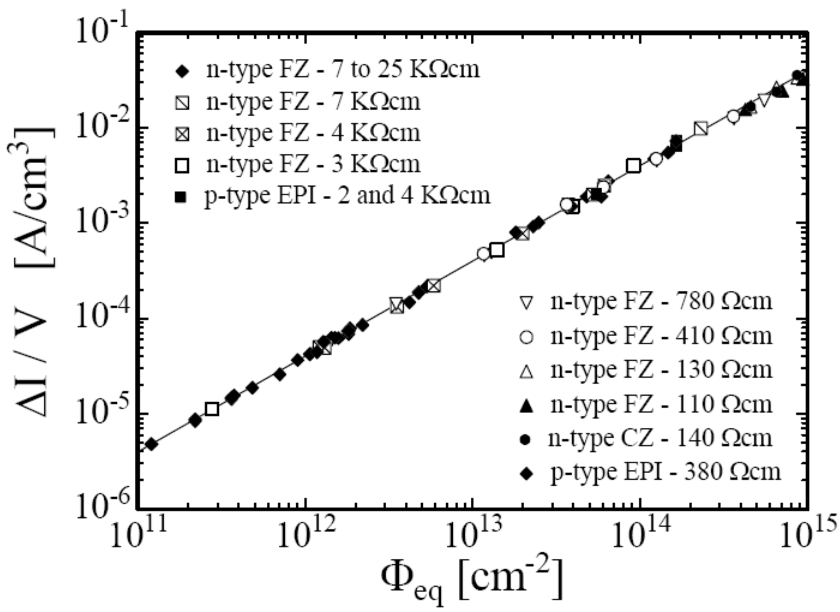

Figure 3.6: Damage induced bulk current as function of particle fluence for different detector types. [26]

Change in the Effective Doping Concentration

The effective impurity or doping concentration is:

$$N_{eff} = \frac{2\epsilon\epsilon_0}{q_0 d^2} V_{dep} \tag{3.17}$$

This equation applies not only for the original n-type silicon (donor doped) but also after irradiation when the effective doping concentration changes its sign by increased generation of 'acceptor like' defects. The change of the depletion voltage can always be described by the related change in $|N_{eff}| = |N_d - N_a|$ with N_d and N_a as the positively charged donor and negatively charged acceptor concentration.

The change of N_{eff} measured as a function of the particle fluence for n-type starting material of the thickness d = 300 μm is shown in Figure 3.7:

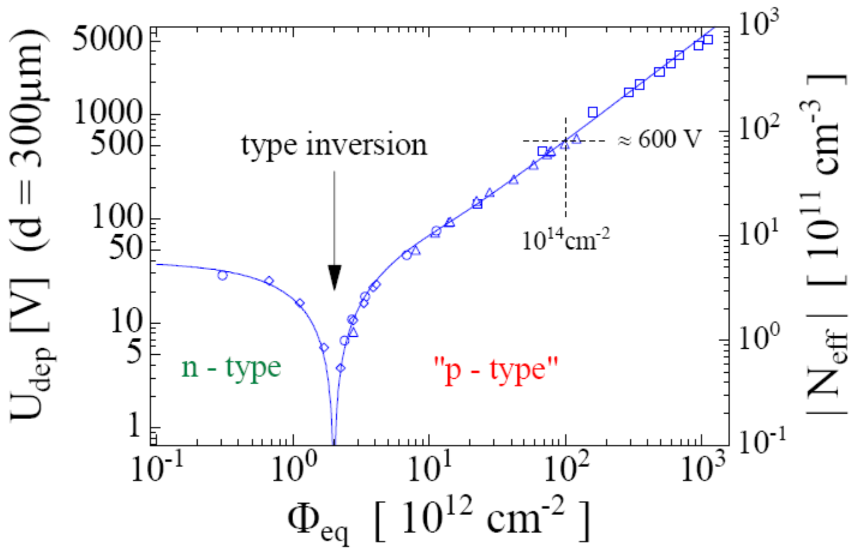

Figure 3.7: Typical evolution of the effective doping concentration in n-type silicon, as a function of the fluence. [27]

Under fluence the effectve doping concentration decreases until the donor concentration equals the acceptor concentration or until the depletion voltage V_{dep} is almost zero, indicating intrinsic material. Exposed to higher fluences, the effective concentration starts to increase again and shows a linear rise of acceptor like defects. This so called 'type inversion' from n-type to p-type material has been confirmed by many experimental groups. The current parameterization of this evolution is known as the Hamburg model, developed by the RD48 collaboration. The next equation shows the Hamburg model, with all effects and including annealing [28]:

$$\begin{aligned} N_{eff}(\Phi_{eq}, t_a, T_a) &= N_{eff,0} \cdot \left(1 - r\left(1 - e^{-c\Phi eq}\right)\right) - \\ &- \Phi eq \left(g_c + g_a e^{-\frac{t_a}{\tau_{T_a}}} + g_y \cdot \left(1 - e^{-k_{T_a} t_a}\right)\right) \end{aligned} \tag{3.18}$$

The first term represents the initial doping concentration minus the donor removal due to radiation, where the donor removal rate is proportional to the donor concentration. The second term represents the fluence-proportional contributions of:

- stable damage
  quantified by an introduction rate g_c
- beneficial annealing
  g_a quantifies the introduction of damage that will beneficially anneal out, this annealing also presents an exponential time dependence whose time constant depends on the temperature at which the device is stored
- reverse annealing
  g_y is the introduced rate and the time dependence is again influenced by the temperature

Loss in the Charge Collection Efficiency

The Charge Collection Efficiency (CCE) describes the ratio of the produced charge, by a traversing particle, and the charge, that can finally be measured at the electrodes. The primary mechanism leading to a decrease in the CCE is charge trapping at defect sites. It reduces the number of charge carriers $N_{e,h}$, for electrons and holes respectively, before they can be collected at the strips in the time t_c. The number of charge carriers is reduced by:

$$N_{e,h}(t_c) = N_{e,h}(0)exp\left(\frac{-t_c}{\tau_{eff}}\right) \tag{3.19}$$

where $N_{e,h}(0)$ is the initial number of charge carriers, t_c donates the collection time of the carriers, which is mainly given by the electric field and the mobility. $1/\tau_{eff}$ is the effective trapping probability which depends linearly on the fluence. According to [29], $1/\tau_{eff} = \gamma_{e,h} \cdot \Phi$, where the charge trapping constant γ has a value of about $4 \cdot 10^{-7}cm^2/s$ for electrons and about $6 \cdot 10^{-7}cm^2/s$ for holes, up to fluences of $\Phi = 2 \cdot 10^{14}cm^{-2}$.

Nevertheless, the Charge Collection Efficiency can partially be restored by applying a higher bias voltage, which results in shorter drift times. This is the reason why, compared to non irradiated detectors where the efficiency curve reaches its plateau at the depletion voltage, irradiated sensors need considerable over biasing beyond the depletion voltage. In practice, this over biasing beyond the depletion voltage in order to reach the efficiency plateau is limited by the high voltage breakdown.

Annealing and Reverse Annealing

Defects caused by radiation can roam around in the silicon lattice, which leads to an initially not stable effective doping concentration. Two effects, annealing and reverse annealing, with different time behaviors and temperature dependence, take place. With time constants in the range of a view days, a decrease in the radiation induced changes occurs soon after irradiation. This short term annealing lessens the type inversion process and manifests itself in terms of decreasing the number of electrically defects created due to irradiation. Consequently it has beneficial impacts on the leakage current, the depletion voltage, etc.. But the transforma-

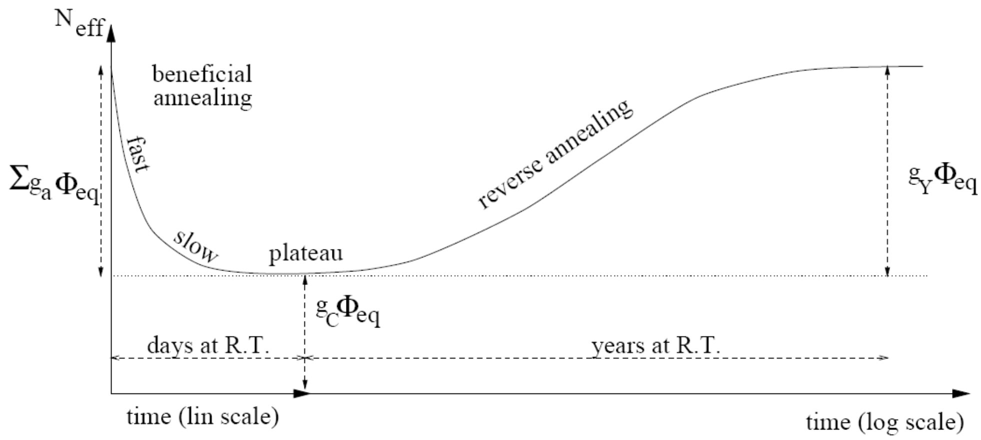

Figure 3.8: Schematic plot of time development of N_{eff}. All three phases are shown with introduction rates for responsible defects. Note that reverse annealing is shown in the logarithmic time scale. [30]

tion of defects in the silicon continues such, that on a timescale of weeks, the irradiation introduced doping concentration increases again. This effect is called reverse annealing and impairs the detector performance. It can be suppressed by cooling the detector to below 0°C and by minimizing the maintenance periods of the silicon detectors at room temperature.

Figure 3.8 shows a schematic plot of the time development of the three irradiation induced defects, sumarised as:

- defects stable in time:

$$N_c = g_c \phi_{eq}$$

- electrically active defects that change to non-active ones (annealing):

$$N_a = g_a \phi_{eq}$$

- electrically non-active defects that change to active ones (reverse annealing):

$$N_y = g_y \phi_{eq}$$

3.2.2 Surface Damage

Typically, radiation induced effects by ionizing particles either at the surface or the Si/SiO_2 interface lead to a charge accumulation at the silicon-oxide interface, resulting in a decrease of the inter-strip isolation. This causes unwanted signal charge sharing. Additionally it leads to an increase in the inter-strip capacitance, which is a major factor when determining the electronic noise of the system. Also an increase of the surface currents has been observed after irradiation, which happens because of the creation of additional surface states, which act as generation centers.

The surface damages due to radiation induced effects are strongly dependent on many design parameters and on the exact processing of the detectors. The capacitive coupling between each strip and its neighbors is dominated by the quality of the oxide at the interface, which is process-dependent, and by the ratio of strip width to strip pitch. It is possible to reduce the damage-induced coupling by substantially over-depleting the device. This produces high fields on the strip side and confines the oxide charge in the region between the strips, thus reducing the capacitance. However, all these surface effects tend to saturate after a few $MRad$, because the concentration of oxide charges does not exceed a certain limit, compare [29]. This saturation of the surface damage lies in sharp contrast to the bulk damage.

3.3 Design of the CMS Silicon Sensors

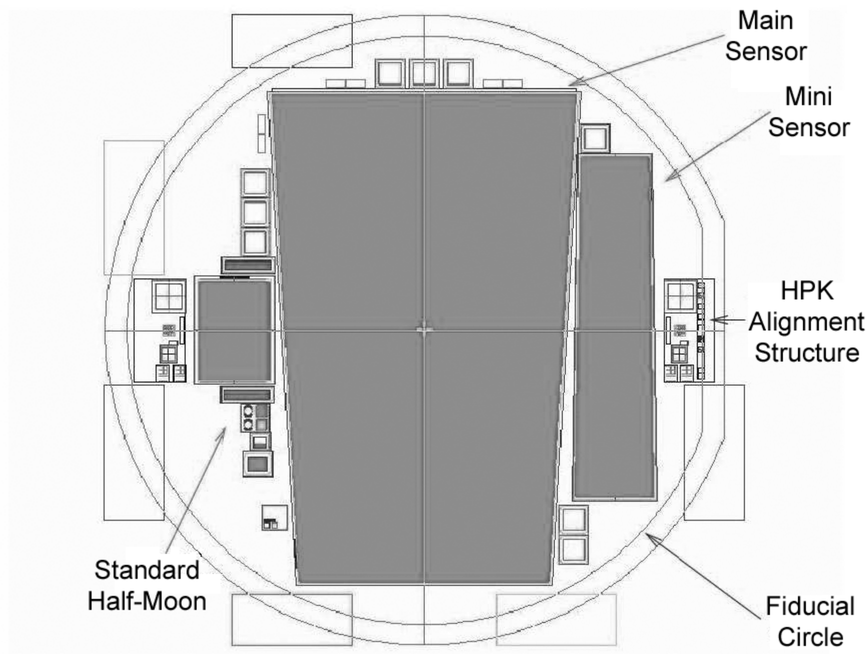

Figure 3.9: Layout of the HPK wafer for a Ring 4 Normal module.

In the CMS silicon tracker 15 different sensor geometries are used: two rectangular types for the TIB, two for TOB and 11 wedge-shaped sensors for TID and TEC. The 10 different TEC sensor geometries can be seen in Figure 3.1. All TEC sensors are manufactured using 6" technology, with the standard planar process usually employed in the Integrated Circuit (IC) industry. As shown in Figure 3.9 each wafer contains one single sensor which is requested to lie inside a fiducial circle with a diameter of 13,9 cm. The exact geometrical properties of the TEC sensors can be found in [31].

Figure 3.10 displays a schematic design of a silicon microstrip sensor. The sensors are single-sided, with p^+-strips on a n-type substrate. p-on-n silicon was chosen, because the effective doping concentration changes during irradiation, where additional acceptor defects are produced. For a n-type substrate material the ef-

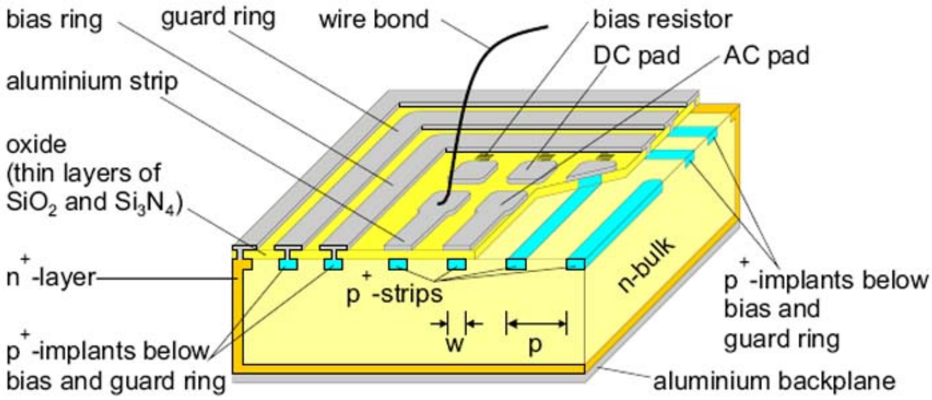

Figure 3.10: Schematic design of a silicon microstrip sensor as used in the CMS experiment.

fective doping concentration decreases with irradiation, till the type inversion is reached and the material becomes effectively a p-type. Further irradiation lead to an increase of the effective doping concentration, as displayed in Figure 3.7. Since the depletion voltage scales with the effective doping concentration, n-type substrates will result in a lower depletion voltage after irradiation then p-type.

The necessary ohmic contact between the bulk and the aluminium backplane is provided by an uniformly metallised n^+-layer on the back side, where the positive high voltage for the reverse bias is applied. This n^+-layer is also present over the entire cutting line of the sensor to keep the space charge region away from the not always perfect cut edges.

The aluminium readout strips on the sensor surface are separated from the p^+-strips below by multiple layers of SiO_2 and Si_3N_4, providing the dielectric for the capacitors made of each pair of p^+- and aluminium strips. These capacitors serve as coupling capacitors for the signal, induced by the movement of the charge carriers in the sensor. These aluminium strips are about 15% wider than the p^+-implants in order to shift regions of high electric fields away from the low resistivity n-bulk to the highly resistive oxide layer, which reduces the risk of electrical breakdowns.

The bias- and the guard-ring surround the sensitive area and are both rings of p^+-implants covered with an aluminium layer. The bias ring is connected to ground and biases each implanted p^+-strip via a metallised DC pad. To put the bias ring and each strip at the desired potential polysilicon resistors are deposited between them. The guard ring is left floating and helps to degrade the electric field between the n^+-implantation at the sensor edges and the bias ring. The round corners of the rings, as seen in Figure 3.11, help to avoid discharges when the the device is operated at high voltages.

Two different thicknesses of 320 μm (low resistivity of 1,5 - 3 $k\Omega cm$) in the inner layers (including TEC Ring1 to Ring4) and 500 μm (high resistivity 3,5 - 7,5 $k\Omega cm$) in the outer layers (including TEC Ring5 to Ring7) are used. Their strip pitches vary between 80 to 158 μm for the 320 μm thick sensors and 122 to 205 μm for the 500 μm thick sensors. Table 3.1 gives a summary of the properties of the different sensor geometries.

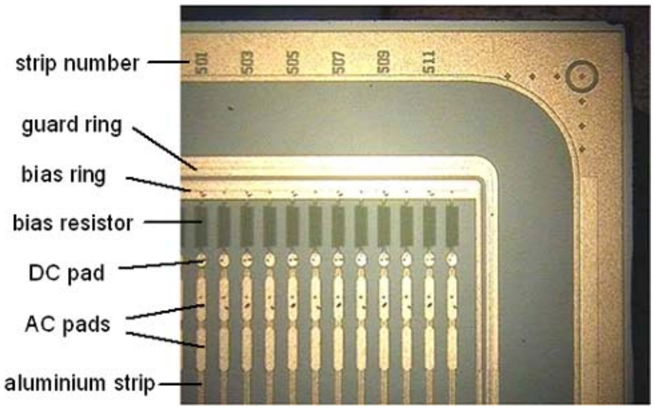

Figure 3.11: Picture of a sensor edge. The marks on the upper right are positioning marks for the sensor assembly. The scratches are from contact needles, which have been used during the sensor quality assurance tests.

Type	Length [mm]	Height [mm]	Pitch [μm]	Strips	Quantity
W1	64,6 / 87,9	87,2	81-112	768	288
W2	88,1 / 112,2	90,2	113-143	768	864
W3	64,9 / 83,0	112,7	123-158	512	880
W4	59,7 / 73,2	117,2	113-139	512	1.008
W5a	98,9 / 112,3	84,0	126-142	768	1.440
W5b	112,5 / 122,8	66,0	143-156	768	1.440
W6a	86,1 / 97,4	99,0	163-185	512	1.008
W6b	97,5 / 107,5	87,8	185-205	512	1.008
W7a	74,0 / 82,9	109,8	140-156	512	1.440
W7b	82,9 / 90,8	98,8	156-172	512	1.440

Table 3.1: Properties of the CMS TEC strip sensors. All together 10.816 silicon strip sensors are needed to accomplish the two Tracker EndCaps. The thickness of the sensors is 320μm for the sensor types W1 to W4 and 500μm for the sensor types W5 to W7. [32]

The main strategies of the CMS Collaboration to ensure the radiation hardness of the silicon sensors consist of reducing the surface damage, delaying the bulk type inversion and using stable sensors with respect to high voltage. Stability with respect to high bias voltages of up to 500 V is ensured by a implementation of a metal overhang over the p$^+$-strips, which improves the field configuration. The use of low resistivity silicon delays the type inversion point and secures a lower depletion voltage after ten years of LHC operation. The sensor bulk consists of n-type, phosphorus doped, <100> silicon, which compared to the standard <111> configuration, minimizes the number of dangling bonds on the surface[3]. This leads to a suppression of the surface damage, resulting in a reduced increase of the interstrip capacitance [23], i.e. capacitive noise after irradiation, which is the

[3]Silicon with the configuration <100> has 10^{10} unbound valence electrons per cm^2 while <111> silicon has 10^{11}.

main noise contribution at a working temperature of -10°C. This temperature was chosen to secure the survival of the silicon detectors in the harsh LHC radiation environment. Only in short maintenance periods they will be exposed to room temperature. For example the leakage current in silicon due to the generation of electron hole pairs is strongly temperature dependent. The ratio of currents at two temperatures T_1, T_2 is given by:

$$\frac{I_2(T_2)}{I_1(T_1)} = \left(\frac{T_2}{T_1}\right)^2 exp\left(-\frac{E_g}{2k_B}\frac{(T_1 - T_2)}{T_1 T_2}\right) \tag{3.20}$$

Cooling to -10°C typically reduces the leakage current to 1/16 of its value at $20°C$. Formula and values from [24].

3.4 Components of the TEC Modules

As displayed in Figure 3.1, the TEC modules consist of one or two sensors and the associated front-end readout electronics. They are mounted on light carbon fibre based support structures. Apart from the different sensor geometries and number of sensors, all modules share the same basic components as shown in Figure 3.12.

Support Structure

The support structure carries the sensors and the readout electronic, which is mounted on the front end hybrid. To keep the material budged of the Tracker as low as possible a minimum of material is used. For two sensor modules the main support structure is formed of two carbon fibre legs glued on a graphite cross piece. One sensor modules consist only of one U-shaped frame of graphite. Graphite is superior to other materials because of its high stiffness at low mass and its efficient removal of heat, generated from the sensors and the front end electronics. In addition it has approximately the same thermal expansion coefficient as silicon and the small differences get compensated by a silicon glue. Also a very important criteria is its sufficient radiation hardness.

To provide extra stability to the silicon sensors, during the production and especially when the sensors gets bonded, one or two rigidifiers serve as supporting structure between pitch adapter and sensor and between sensor and sensor.

Kapton Foil

The thin metallised kapton foil is located between the frame and the sensors. It is glued on the frame with an araldite glue[4] and the sensors are glued to it with a silicon glue. The kapton foil brings the bias voltage to the backplane of the sensors. This connection is accomplished with the conductive glue EPO-TEK EE129-4. Some additional components ensure the stability of the bias voltage and two thermistors provide temperature feedback of the module. The return line of

[4]Epoxy AW 106: 2011 ARALDITE, Huntsman

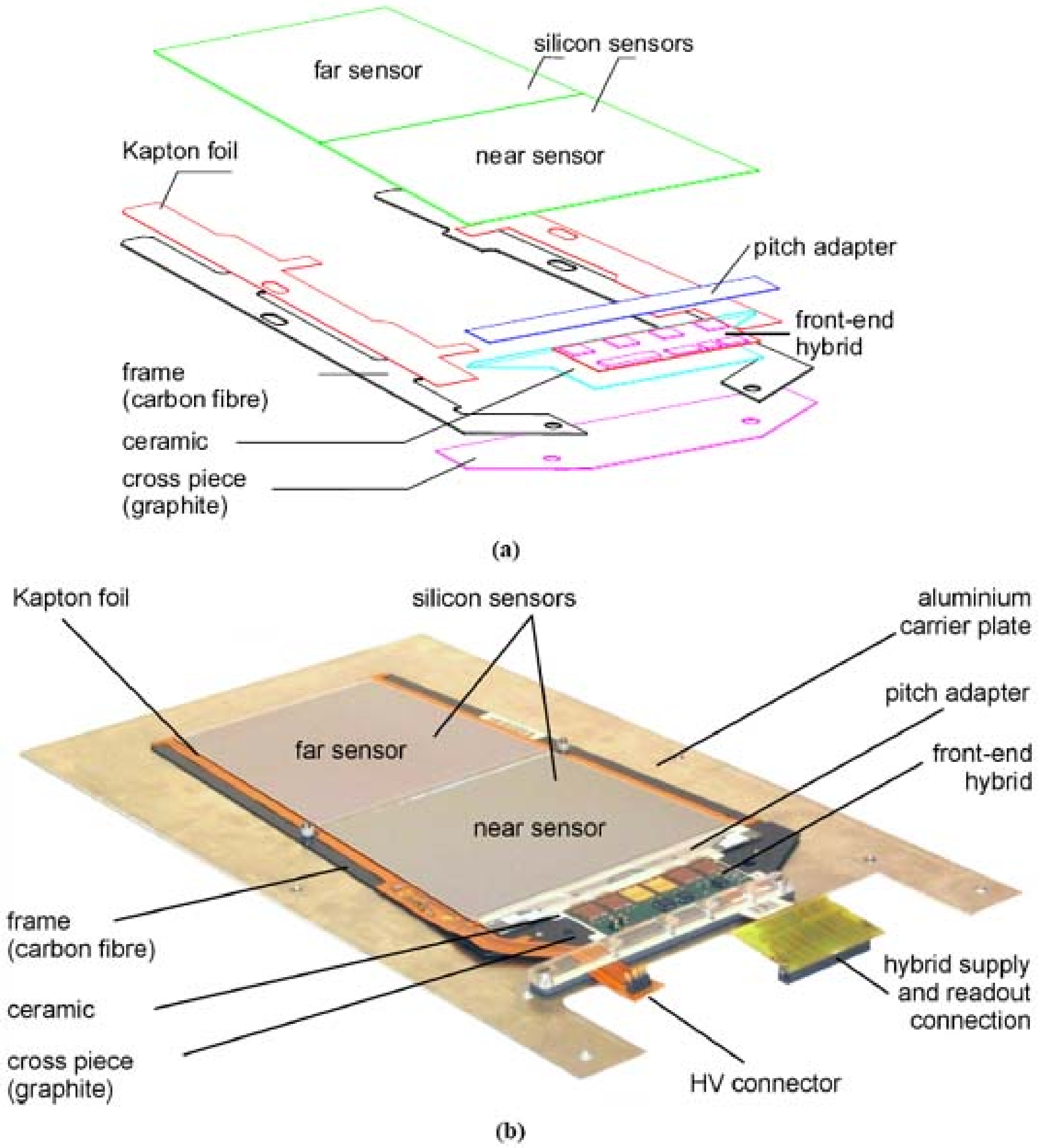

Figure 3.12: (a) Exploded view of a ring 6 TEC module. (b) Photograph of a ring 6 TEC module mounted on an aluminium plate, the so called transport plate, which eases the transport and the handling of the modules.

the high voltage is a thick line on the pitch-adapter connecting the bias ring on one side and the hybrid ground on the other side. This line can be seen in Figure 3.13 at the upper right of the pitch adapter.

Front-End Hybrid

The hybrid houses the front-end readout electronics of the detector modules. It is composed of a four layer circuit in kapton technology and brings power and control lines to the integrated electronics. Its heart pieces are four (on modules with 512 readout channels) or six (on modules with 768 readout channels) analogue pipeline voltage (APV) chips. The other electronics mounted on the hybrid are a 2:1 multiplexer (MUX), a phase locked loop (PLL) chip and a detector control unit (DCU) chip, as marked in Figure 3.13. All chips can be programmed and red out via an I^{2}C interface.

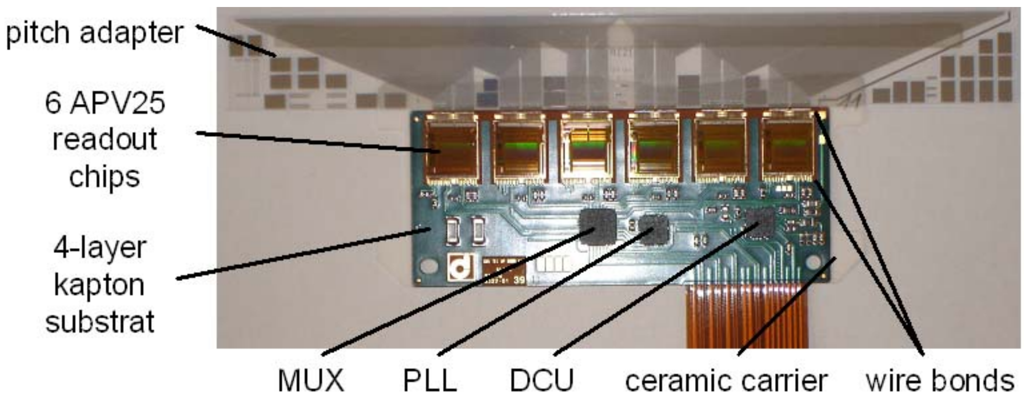

Figure 3.13: Picture of a front-end hybrid with pitch adapter.

APV Chip

The APV25 chip is a 128-channel analogue pipeline chip and the heart piece of the readout electronics of the silicon microstrip detectors. Each channel comprises a low noise amplifier, a 192-cell analogue pipeline and a deconvolution readout circuit as shown in Figure 3.14. Via an analogue 128:1 multiplexer the output data of each APV is transmitted on a single differential current output. For a proper operation the APV requires a connection to a 40 MHz clock line and two operation voltages of 1,25 V and 2,5 V (plus ground). The used standard 0,25 μm CMOS technology guaranties low noise and power, a high circuit density and a high radiation tolerance. A description of the design and results from measurements prior to irradiation are presented in [33].

Multiplexer

The MUX chip is a 2:1 multiplexer which multiplexes the output of two APV chips together into a single output line in order to minimize the number of readout channels.

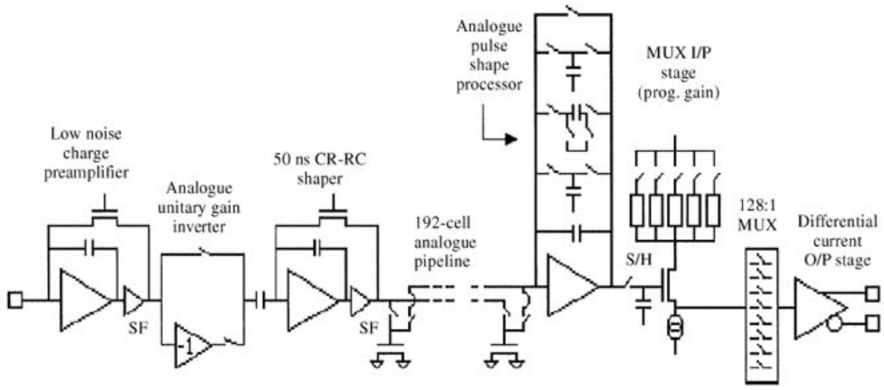

Figure 3.14: Block diagram of one channel of the APV25.

Phase Locked Loop Chip

The PLL chip decodes the signal containing the clock and the level 1 trigger information for the MUX and the APV chips. For an accurate measurement of the analog data from the APV chip it is crucial that the time jitter does not exceed 0,5 ns. Additionally to clock recovery and trigger decoding the PLL chip can also compensate clock delays, which can be introduced by the different runtime of signals in cables of different lengths or the different times of flight of particles from the interaction point.

Detector Control Unit

The DCU chip monitors the sensor temperatures, the leakage current and the low voltages (1,25 V and 2,5 V) for the APV chips and the hybrid. In addition, the DCU possesses a uniquely 24 bit identifier, intended to allow the safe identification of each single module inside the tracker. The leakage current of the sensors is monitored with the help of a resistor. The APV power supply voltages $V_{1,25}$ and $V_{2,50}$ are maintained using two external resistive dividers. The hybrid temperature is measured inside the DCU and the sensor temperature with two external thermistors on the kapton bias circuitry.

Pitch Adapter

The pitch adapter is made out of a glass substrate where 1,5 μm thick aluminium strips, with bond pads at each end, are superimposed. They connect the APV chips, where the pitch of the input channels is 43 μm, with the aluminium strips on the sensor, where the pitch is 61 to 254 μm. Besides that it increases the distance between the heat producing electronics and the sensors.

Chapter 4

Quality Assurance

4.1 Tracker Data Base

To make the whole CMS Tracker Project possible, it was essential to collect all informations about all parts at every time and to give access to that data to all parties participating in the CMS experiment. This was accomplished with a central Oracle based database system build up at CNRS Lyon. In this so called TrackerDB (for Tracker Data Base [34]) every single part of the CMS Tracker is registered. All measurements and all test results on these parts are included. The history of each object, including shipments, is monitored. Handling of the data is endowed via the so called BigBrowser, a java-based program, which allows easy insertion, viewing and extracting of the data. Without the TrackerDB it would have been impossible to organize the production of the CMS Tracker, with all the participating institutes, spread all over the world, working within the CMS collaboration.

4.2 Sensor Quality Control

On account of the large number of silicon sensors in the CMS Tracker, a sophisticated quality assurance scheme was essential to ensure that the silicon detectors meet the required specifications. Additionally it was very important to have continuous information about the quality of the sensors during the long production of the Tracker. To ensure this, everything that happens with a sensor is recorded in the TrackerDB. The flow of the sensors from the manufacturers to the module assembly centers is described in detail in [35] and can also be seen in Figure 4.1.

CERN received and registered all sensors from the two fabrication centers, Hamamatsu, Japan and ST-Microelectronics, Italy, and shipped them afterward to the five Quality Test Centers (QTC). The QTCs were responsible for the overall sensor quality. On a small percentage of the sensors further tests were made in the Irradiation Qualification Centers (IQC), 1% of the sensors, and in the Process Quality Centers (PQC), 5% of the sensors.

The production of the sensors was split into two stages. In the first phase, the pre-series, 5% of all sensors were produced and each of these sensors was elec-

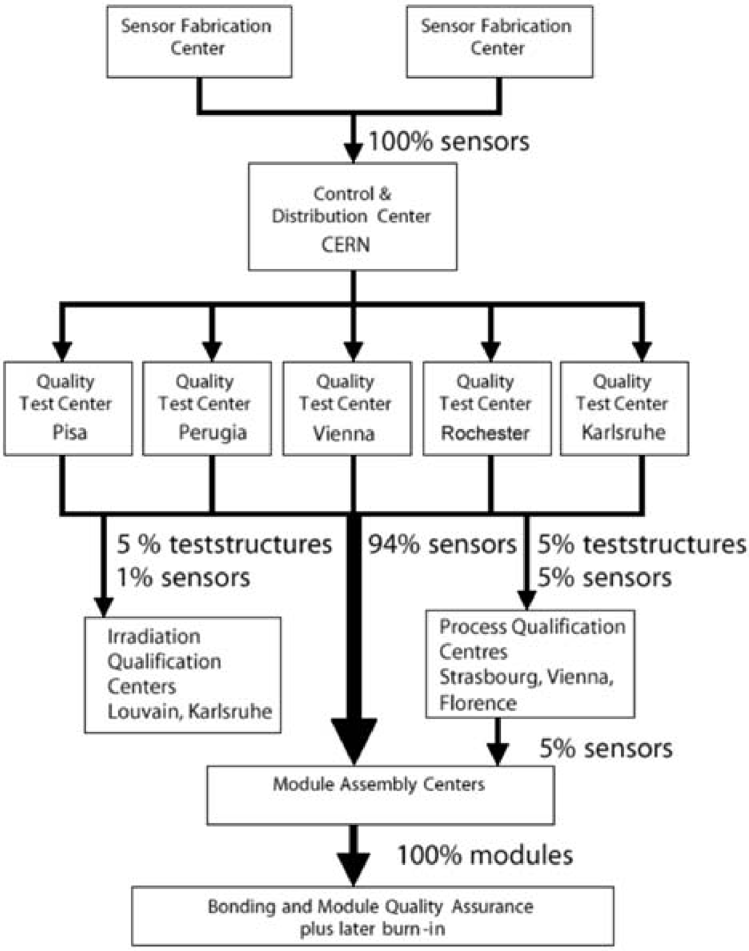

Figure 4.1: Logistics for the CMS Quality Assurance.

tronically tested like described in more detail in [32]. In the second phase, the full production phase, the quality was monitored on a sample basis of about 5%, with the goal to verify the measurements done from the production companies. In addition the manufacturing process was constantly monitored with standardized measurements on the test structures in the Process Quality Centers during the whole production. A picture of a test structure can be seen in Figure 4.2. Independently from the different production phases, 100% of the sensors were optically inspected with a microscope for mechanical defects like broken edges or scratches.

4.2.1 Quality Tests

As mentioned above, samples of sensors were electrical characterized in the Quality Test Centers (QTC). For the sensor quality tests a computer controlled set-up including a probe-station, a high voltage supply, an electro meter, a capacitance meter and a switching device were used in a humidity and temperature controlled environment. Depending on the number of sensor strips, a complete electrical test needs about 3-4 hours. It consists of two global (IV, CV) and four strip-by-strip (I_{strip}, R_{poly}, I_{diel}, C_{AC}) tests:

- IV Curve
  During this test the leakage currents at reverse bias voltages of 0 V to 550 V are measured. The specifications for this test are:
  - leakage current at 300 V of less than 5 μA
  - leakage current at 450 V of less than 10 μA
  - maximum current increase in the range of 450 V to 550 V of less than 10 μA
- CV Curve
  With this measurement the depletion voltage of the sensor can be verified. The total capacitance of the sensors is measured from 0 V to 350 V reverse bias.

The goal of the strip-by-strip tests, which were all performed at a bias voltage of 400 V, was to identify defect strips. The upper limit for the number of bad strips per sensor is 1%.

- Single Strip Current(I_{strip})
  Strips with a leakage current above 100 nA are marked as leaky (noisy) strips.
- Poly-Silicon Resistance (R_{poly})
  As shown in Figure 3.10 and Figure 3.11, each poly-silicon or bias resistor connects one readout aluminium strip to the bias ring of the sensor. The resistor values must be 1,5 ± 0,5 $M\Omega$ and not outside ± 0,3 $M\Omega$ with respect to the average sensor value.
- Dielectric Current (I_{diel})
  While applying a small voltage between the DC pad (p^+ implant) and the aluminium readouts, for an intact SiO_2 layer, there should exist no measurable current. A current above 100 nA is an indication of a pinhole, which is an undesired connection between the implanted p^+-strip and the aluminium readout strip.
- Coupling Capacity (C_{AC})
  The measurement of the coupling capacitor is a check for pinholes and monitors the uniformity of the oxide layer. In addition shorts between two strips can be detected since the measurement is made between two adjacent DC pads shorted together and the corresponding central AC pad.

4.2.2 Process Quality Control

Apart from the sensor, each wafer contains additional devices, as displayed in Figure 3.9. The so called half-moon, see Figure 4.2, was designed to enable the monitoring of the stability of the sensor production process. This is possible, because the sensor and its appropriate test structures are from the same wafer, and therefor have met the same circumstances during the manufacturing. The

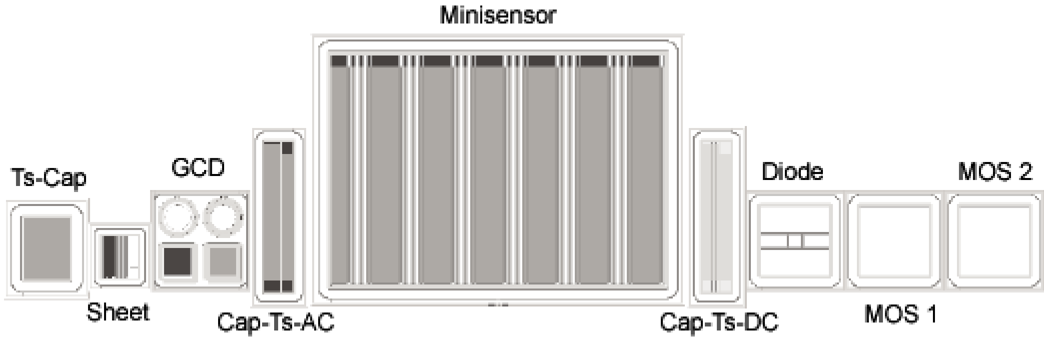

Figure 4.2: The standard set of nine structures which is placed inside the fiducial region on each wafer (called half-moon because of its shape).

design of these nine structures is identical for all sensor geometries and for both suppliers. From left to right the half-moon contains:

- Ts-Cap
  This structure is an array of 26 strips connected directly to the bias ring without any poly-silicon resistor. At the end of each strip an AC pad for readout is placed. The dielectric structure is the same as for the main detector: multiple layers of SiO_2 and Si_3N_4. With the TS-Cap the Coupling Capacitance (C_{ac}) (limits: 16 $pF < C_{ac} <$ 20 pF for STM and 18 $pF < C_{ac} <$ 25 pF for HPK) and the Dielectric Breakdown Voltage (V_{diel}) (limits: $IV_{diel} <$ 10 nA and $V_{break,diel} >$ 120 V) can be measured.

- Sheet
  The Sheet is build of nine superficial structures to measure some important resistances. It contains three implanted p$^+$-strips (limit: $\rho_{p^+} < 400\ \Omega/sq$), three aluminum strips (limit: $\rho_{Al} < 30\ m\Omega/sq$) and three poly-silicon resistors (limit: $1 < R_{poly} < 2\ M\Omega$). All of them lie directly on the n-doped bulk.

- GCD - Gate Controlled Diodes
  This structure hosts two circular and two square formed gate controlled diodes. The GCDs are build of comb shaped p$^+$-implanted strips alternated with strips made of MOS material. From the measurement conclusions about oxide contaminations can be drawn.

- Cap-Ts-AC
  This device is build of nine strips with the same structure as the main sensor. The outermost set of three strips on either side of the structure is connected to ground. It is used to measure the Interstrip Capacitance (limit: $C_{int} <$ 1,3 pF) which provides conclusions about detector noise and signal to noise ratio.

- mini-sensor
  The mini-sensor has an active area of 2,3 $\times$ 1,6 cm^2 and comprises 192 strips

with a pitch of 120 μm. Here an IV curve from 0 V to 700 V is taken which leads to the breakdown voltage and the current value at 450 V. This values are compared with the limits of $V_{break} > 500\ V$ and $I(450V) < 1\ \mu A$.

- Cap-Ts-DC
  This structure is similar to the Cap-Ts-AC, with the difference that the strips are not connected to the bias ring, either directly nor through a bias resistor. Additionally the dielectric layer is missing in the strips and the p^+-implant can be contacted all over their length. On this device the interstrip resistance R_{int} can be measured between the central strip and its two neighbours (which are tied to ground). Since the interstrip resistance should be high $R_{int} > 1\ G\Omega$, a very low current across the strips of a few pA should be measured.

- Diode
  With the help of this simple diode, which is surrounded by a guard ring, it is possible to determine the wafer thickness and the silicon resistivity through a CV curve. Furthermore the depletion voltage (limit: $V_{depl} < 100\ V$) of the sensor (taking an geometric factor into account) and the depletion depth can be determined.

- The two MOS devices
  The dielectric composition corresponds, for both MOS devices included in the HPK structures and for the first MOS in STM wafers, to the thick oxide layer that is present in the interstrip region in the main detector. The second MOS on each STM sensor contains a dielectric layer which follows the structure of the decoupling capacitance in the detector strips. The first MOS is used to measure the Flatband Voltage (V_{fb}) (limit: $V_{fb} < 2\ V$) by applying a rising bias voltage to the backplane. Via the Flatband Voltage the trapped positive charges in the oxide and the thickness of the oxide can be calculated.

The measurement analysis and data acquisition is made by a computer running Labview. The tests on all test structures are made simultaneously in a light tight probestation. The set up and the results of these measurements with a detailed interpretation of them can be found in [36].

4.2.3 Long Term Tests

Since the access to the sensors installed in the CMS detector is very limited, it is very important to ensure the long term stability of them. Long term tests were done for a small, but representative sample of all sensors delivered by the two suppliers. A typical long term measurement takes between three and five days at room temperature and is performed in a light-tight and humidity controlled environment (Relative Humidity (RH) between 10% and 30%). A very small part of the sensors was even long term tested at the CMS operation temperature of -10°. In these tests a reverse bias voltage of 400 V is applied to each sensor with a serial connected 470 $k\Omega$ resistor. Via the voltage drop on the resistor the dark current can be measured. A computer running Labview controlls the tests and saves the temperature, the relative humidity of the environment and the sensor currents, derived from the voltage drops, every minute. The specified limit for the dark current is 10 μA at 400 V. Results of these measurements and a detailed interpretation of them can be found in [36].

4.2.4 Irradiation Tests

Irradiation experiments with the sensors are important to ensure their required radiation hardness. These experiments were performed with neutrons at the Louvain-la-Neuve cyclotron at the Universite catholique de Louvain[1], the results obtained on CMS sensors from 2002 to 2004 are presented in [28]. In addition irradiation tests with protons were performed at the cyclotron of the Institut für Experimentelle KernPhysik (EKP) at the University of Karlsruhe[2], as presented in [37]. Since these are destructive tests, mainly test structures and only a small number of sensors (about 1%) were used. Before and after the irradiation the CV and IV characteristics, the interstrip resistances and capacitances, the bias resistors, the dielectric current and the coupling capacitances were measured.

4.3 Hybrid Quality Control

The production of the hybrids took place in several steps. After each production step various tests were performed to control the quality. The 24 different pitch adapters were produced by two firms, RMT and Planar. The bare hybrid production was also shared by two firms, Cicorel produced the circuits and HybridSA loaded and tested them. Simultaneously samples of each batch were sent to Strasbourg for quality control. In addition irradiation tests of some hybrids were performed, which showed that the hybrid will still proper operate after 15 years inside the LHC environment. Only after Strasbourg gave the OK for each batch of hybrids it was free for the further production. Then each single hybrid was visual inspected at CERN. Afterward the hybrids were tested with the so called Front-end Hybrid Industrial Tester (FHIT) which is described in [38]. With the FHIT it is possible to fulfill a simple electrical and continuity test in about one minute. Additionally a full functionality test, including read-out, is performed in this test station. Also a calibration of the ADCs in the DCU is performed. Then again an optical inspection was performed, after the pitch adapter was assembled to the bare hybrid by a robot. Qualified hybrids were bonded by semi-automatic bonding machines at both sides of the APVs, like shown in Figure 3.13 and on test pads on the hybrid and the pitch adapter. On a part of these test bonds pull tests were performed to controll the pull force of the bonds. The remaining test bonds were ignored at first and later they had to be removed by the module bonding

[1] Sensors and test structures were irradiated up to $2.1 \cdot 10^{14}\ n_{eq}/cm^2$.

[2] The irradiation was performed up to $3 \cdot 10^{14}\ n_{eq}/cm^2$ and $0.9 \cdot 10^{14}\ n_{eq}/cm^2$ for the HPK and STM sensors respectively (derived from leakage current measurements).

centers. In addition five thermal cycles where done on each hybrid[3]. As the last quality control step, before the hybrids were shipped to the module assembly and module bonding centers, an electrical test with an APV readout controller (ARC) system (compare chapter: 4.4.4) was performed for each hybrid. In the following module production, the hybrid got repeatedly optical inspected and its functionality was tested at each of the following ARC tests. More details of the hybrid quality control can be found in [39] and [40].

Conclusion

Some problems appeared during the hybrid production which lead to a huge delay in the complete module production. The hybrid production rate became the limiting factor. This delay was mainly caused by the so-called via-problem. This fault was not found until the module long-term tests. At some hybrids the 100 μm vias contact broke. All modules with hybrids from these batches were immediately set to faulty and their sensors recuperated wherever possible. To solve this problem the hybrid had to be redesigned as displayed in Figure 4.3. The vias were increased to 120 μm and an additional kapton layer was introduced.

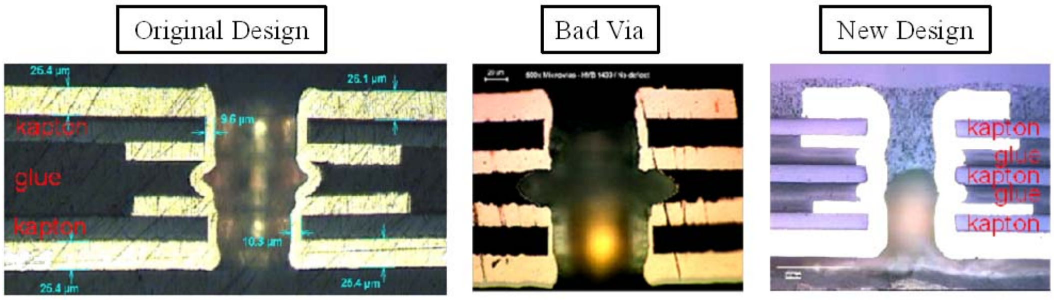

Figure 4.3: Between the original and the new design of the via contact a broken via contact of the old design is displayed. The vias were increased to 120 μm and an additional kapton layer was introduced.

All together 325 modules were build with hybrids from bad batches or prototype components. These modules were completely removed from the module production and are therefore not included in all the numbers and plots of the module production quality as listed below. 166 of these modules were disassembled and their sensors reused to build new modules.

4.4 Module Quality Control

In the following section, the module quality control and the final quality of the CMS TEC module production are presented. Each production step, including the appropriate quality assurance schemes, is described like they were accomplished in the High Energy Physic Institute (HEPHY) Vienna.

[3]The hybrids were alternative cooled down to $-30°C$ (five times) and heated to $80°C$ (four times).

4.4.1 Module Assembly

In total six Gantry centers were involved in the TEC module production, listed in Table 4.1.

Center	Assembled Geometries
Brussel	R3, R5N, R5S, R6, R6A
Fermilab	R7
INFN	R3, R4, R4A
Lyon	R1N, R1S, R3, R4, R4A, R7
UCSB	R5N, R5S, R6, R7
Vienna	R2N, R2S

Table 4.1: List of the different TEC Gantry Centers and the ring geometries they assembled (R stands for Ring; N for normal, S for stereo and A for the optical alignment modules). A picture of the different TEC module geometries can be seen in Figure 3.1.

The total numbers[4] of assembled TEC modules are shown in Figure 4.4. In addition to these 7.228 assembled TEC modules, 325 modules were build with prototype components or with hybrids from bad batches. These were more or less evenly distributed over all geometries, and are not included in this and all following plots and numbers in this chapter.

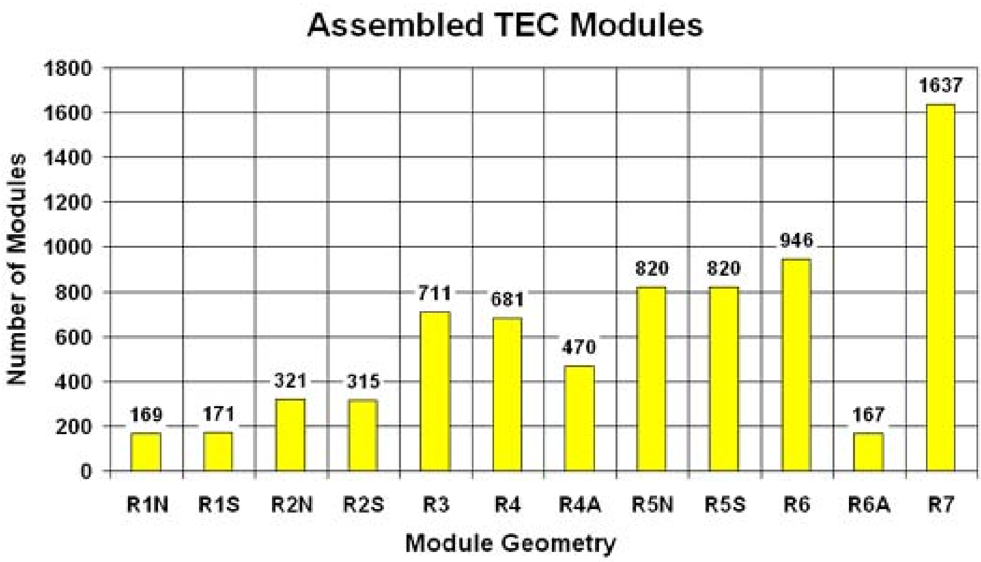

Figure 4.4: Total assembled TEC modules separated by their geometries.

As viewed in the Table 4.1, in Vienna all TEC ring 2 modules were assembled. In numbers 321 ring 2 stereo (R2S) and 315 ring 2 normal (R2N) were build. Unlike in the other TEC Gantry centers, where fully automated gantry robots

[4]These, and all following numbers are from September 2006. Afterward some small changes due to the production of spare modules and the ongoing petal-disassembly might have occurred.

were used, in Vienna all modules were assembled by hand. This production step has been very delicate, since the sensor alignment has to be within tough limits as shown in Table 4.2.

Pre-Assembly

Before the modules were assembled, each component, by name: the tested sensors (compare chapter: 4.2), the carbon frames containing the tested kapton foil (as described below) and the ARC tested front- end hybrids which were already glued and bonded to the pitch adapter (compare chapter: 4.3), had to be optical inspected.

For each carbon frame the parameters of the resistances, thermistors and capacities on the included kapton circuitry were checked as shown in Figure 4.5. In Vienna only two of more than 650 frames had to be excluded. Both had a too low capacitance between Pin 1 and Pin 5 (less than 13 nF instead of 15 nF).

1) Thermistors
- a) Resistance (Pin 12 - Pin 10): 10 kΩ
- b) Resistance (Pin 11 - Pin 9): 5 kΩ

2) HV - Bias
- a) Resistance (Pin 1 - Detector-Pad): 13 kΩ
- b) Capacitance (Pin 1 - Pin 7): 22 pF
- c) Capacitance (Pin 1 - Pin 5): 15 nF
- d) HV-Test (Pin 1 Pin - 5): 600 V dc
- e) HV-Test (Pin 1 Pin - 7): 600 V dc

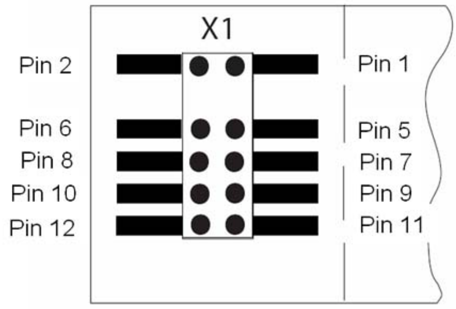

Figure 4.5: Values inspected during the pre-assembly test of the kapton foil. The drawing on the right represents the contact pins of the kapton foil.

Assembly

As mentioned above, in Vienna the module assembly was made manually. The whole assembly was performed in a clean room. Since the other five gantry centers used fully automated gantry robots the assembly procedure in those centers was different from the procedure used in Vienna, compare [42].

To make the needed high precision in the range of μm possible, compare Table 4.2, a coordinate measuring machine from Mitutoyo, shown in Figure 4.6, and three precision tables[5] as shown in Figure 4.7 were used.

As reference system two pins inserted into the table and two reference marks glued on each of the precision tables were used. The carbon frame got plugged on the table via its high precision holes on the two pins. On the precision table, all module parts, see Figure 4.7, are adjusted with the help of the coordinate measuring machine, with a maximum accuracy of a few μm, and held by vacuum. The adjustment is performed via a high resolution camera connected to a screen and

[5] These precision tables were designed and build by the HEPHY workshop.

Figure 4.6: The coordinate measuring machine from Mitutoyo used in Vienna to make a proper alignment of the individual components on the module possible. The high resolution camera is implemented in the gantry arm. Two precision tables and the top vacuum gantry can be seen on the gantry table.

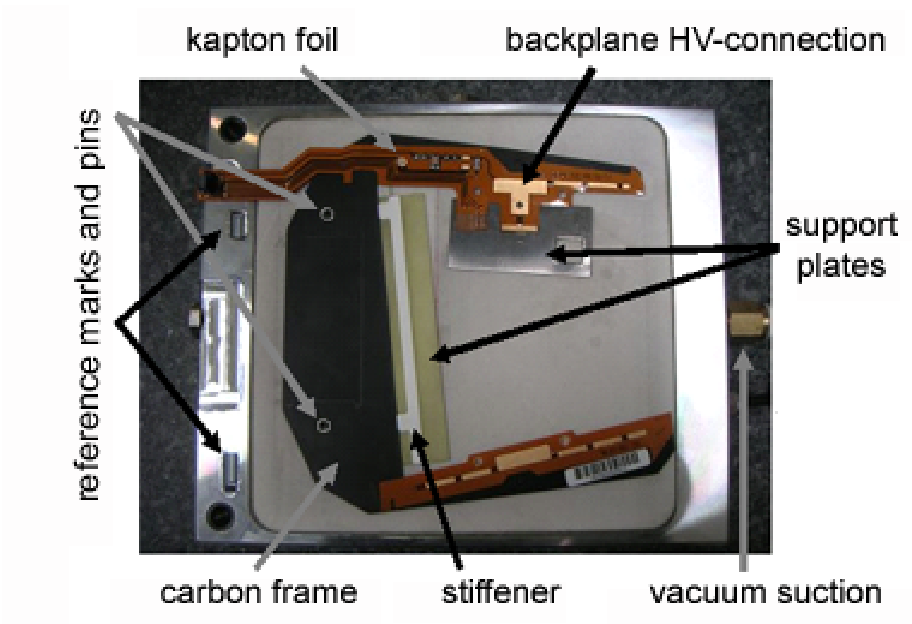

Figure 4.7: A zoom in on one of the three precision tables with all components of a R2S module, except for the sensor, fixed to it.

value	limits
delta X	-39 μm to +39 μm
delta Y	-65 μm to +65 μm
silicon1-silicon2 angle	-20 $mdeg$ to +20 $mdeg$
silicon-frame angle	-30 $mdeg$ to +30 $mdeg$

Table 4.2: The finalised cuts for the gantry precision. All the deviations are respectively to the nominal values.

specification	faulty modules
S1 delta X	19
S2 delta X	11
S1 delta Y	6
S2 delta Y	7
S1-S2 angle	15
S1-frame angle	3
S2-frame angle	0
# of modules	36
unknown	16

Table 4.3: Number of modules outside the different assembly specifications. All together 36 modules are outside the cuts and an additional 16 modules got faulty during the assembly due to other reasons. (S1 ... first sensor, S2 ... second sensor)

to a computer, which runs the program COSMOS[6]. Then a glue[7] for electronically connecting the HV-connection of the kapton to the sensor backplane and another glue[8] to fix the sensor on the frame are applied. Afterward the sensor, hold from above via vacuum, is positioned with the help of two micrometer screws. A third glue[9] is used to attach the stiffener and the hybrid on the carbon frame. The drawings for the glueing scheme can be found in [43]. After the assembly, a position measurement for the sensor and the hybrid is done and the measured data is written to a .xml file which can easily be uploaded to the TrackerDB. Then the module parts are left held by vacuum to the precision table overnight, so that the glues can cure. In the morning of the next day a second positioning check, still under vacuum, is performed and the data written to the same .xml file. Then the module gets released and transported to the bonding room. Beginning in the middle of 2006 an additional glue reinforcement was introduced to the backplane-HV connection. The reasons for the introduction of this additional reinforcement are described in chapter 4.4.3. A complete set of procedures to follow during the module assembly in a CMS Gantry Center to ensure uniform procedures and assembly quality is given in [41].

[6]This is an easy to use software package delivered with the coordinate measuring machine.
[7]conductive glue EPO-TEK EE129-4
[8]DOW CORNING, 3140 RTV COATING; non-corrosive Silicon Rubber, flowable
[9]Epoxy AW 106: 2011 ARALDITE, Huntsman

Results

The next three plots, Figures 4.8, 4.9 and 4.10, show the distribution of the geometrical precision for all TEC modules. In total only 36 out of the 7.228 assembled modules[10] lie outside the specifications (see Table 4.2) as shown in Table 4.3. These are an amazing 99,5% good assembled TEC modules. In this number only modules are included, which have an uploaded second positioning check in the TrackerDB. Modules which for example mechanically broke or where the positioning check was not uploaded to the TrackerDB are apparently not included. Considering these 16 modules, which got additionally faulty during the assembly, due to broken sensors or frames, overall 7.176 modules (99,28% of the assembled modules) could be bonded.

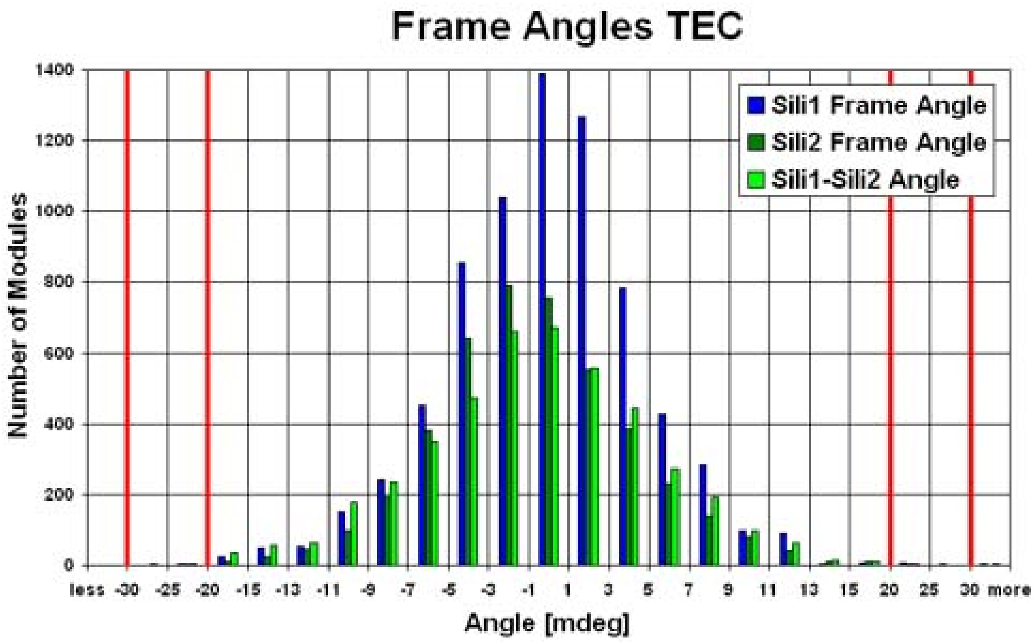

Figure 4.8: Module assembly precision angles of all produced TEC modules. An angle of 0 *mdeg* means no deviation from the nominal value. 15 modules have a deviation outside ±20 *mdeg* for the silicon1 to silicon2 angle and 3 modules are outside ±30 *mdeg* for the silicon1 to frame angle and are therefore considered as faulty. Not a single module lies outside the specification for the silicon2 to frame angle.

[10]Status September 2006, afterward a few more modules got assembled with the goal to produce spare modules out of the surplus material.

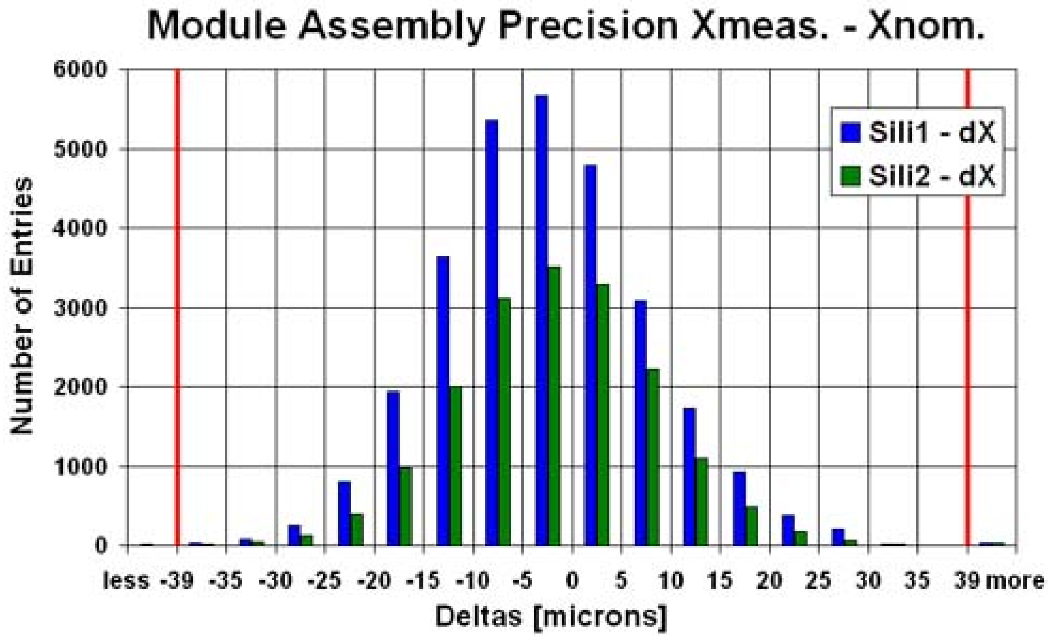

Figure 4.9: Deviation of the X values which arose during the module assembly shown for all produced TEC modules. 24 modules have a delta X value outside ± 39 μm and are therefore considered as faulty.

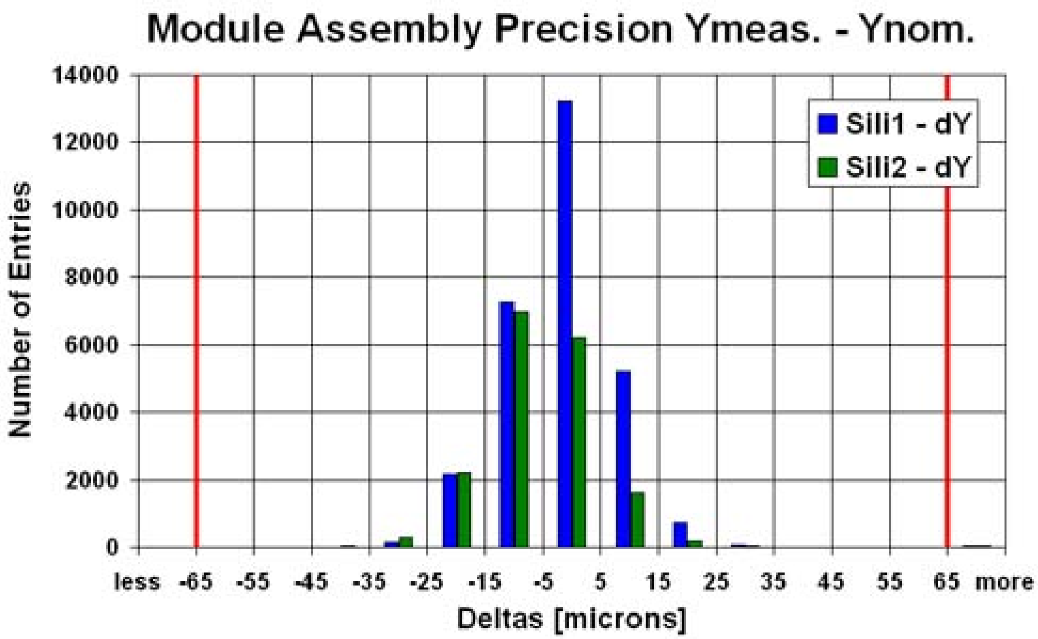

Figure 4.10: Deviation of the Y values which arose during the module assembly shown for all produced TEC modules. Only 7 modules contain a delta Y value outside ± 65 μm and are therefore considered as faulty.

Conclusion

My overall impression is, that the number of faulty modules due to the assembly precision from the TrackerDB are a lower limit. This comes from the fact, that the second sensor position check (final check after curing of the glue) was performed while the sensor was still fixed on the assembly table via vacuum. After releasing of the modules from the vacuum, the sensor might have slightly moved. In addition the precision holes in the carbon frame are not 100% perfect and so the position of the frame slightly differs when using different positioning pins. In Vienna precision measurements after removing the sensor from the assembly table slightly differed from the values taken for the same sensor before this removal, but only in the order of a few μm. It is also possible that the position of the sensors slightly changed during transport and the upstanding storage in the transport boxes, but an additional positioning check after transport and storage was not foreseen.

4.4.2 Bonding

After the module assembly, the modules were electrically finalised during the bonding procedure in the Bonding Centers (BC). In these centers the electronic connections between pitch adapter and sensor1 and between sensor1 and sensor2 were established. This was accomplished by ultrasonic wire bonding, which is a procedure where small 25 μm diameter aluminium wires, including 1% silicon, get soldered to the designated bonding pads. The TEC module bonding was done in 9 different Bonding Centers, listed with the appropriate geometries in Table 4.4.

Center	Bonded Geometries
Aachen-1	R5N, R5S, R6, R6A
Fermilab	R7
Hamburg	R1N, R1S, R3, R7
INFN	R3, R4, R4A
Karlsruhe	R5N, R5S
Strasbourg	R7
UCSB	R5N, R5S, R6, R7
Vienna	R2N, R2S
Zürich	R4, R4A, R7

Table 4.4: List of the different TEC Bonding Centers and the appropriate ring geometries they bonded.

In Vienna all TEC ring 2 modules were bonded. For the first production run a Kulicke & Soffa bonding machine was used. Since January 2005 a Delvotec 6400 automatic bonding machine, shown in Figure 4.11 and 4.12, was available. From the HEPHY workshop three different bonding jigs were built, one for each ring 2 normal and ring 2 stereo modules and one to support the modules during the backplane bonding. While it took about two hours to do the 768 strip- and the 5 HV-bonds with the Kulicke & Soffa bonding machine, with the Delvotec 6400 the time to bond one module was reduced to about 15 minutes.

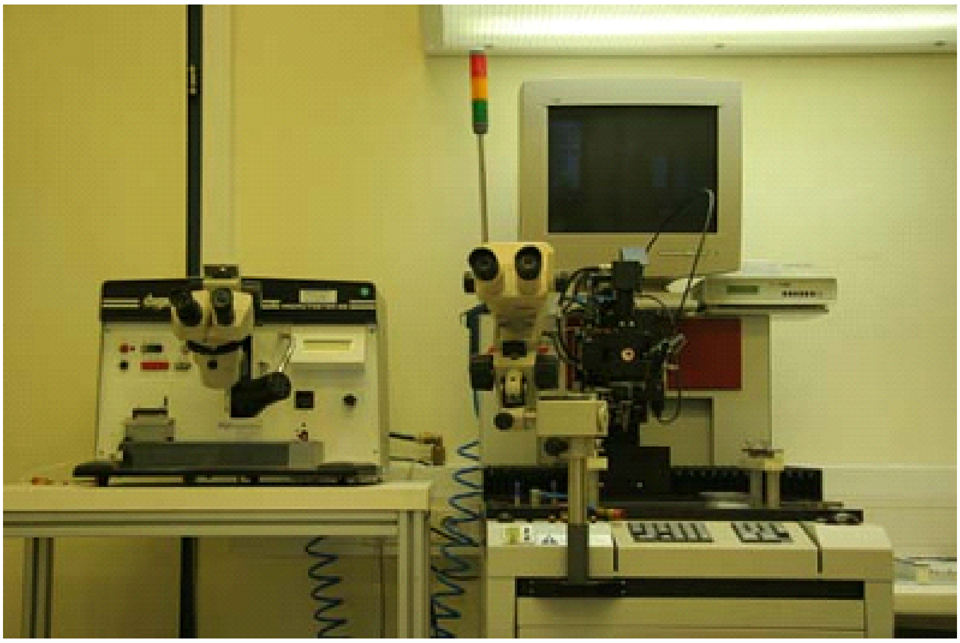

Figure 4.11: The pull force tester used in Vienna on the left and the Delvotec 6400 wire bonding machine on the right.

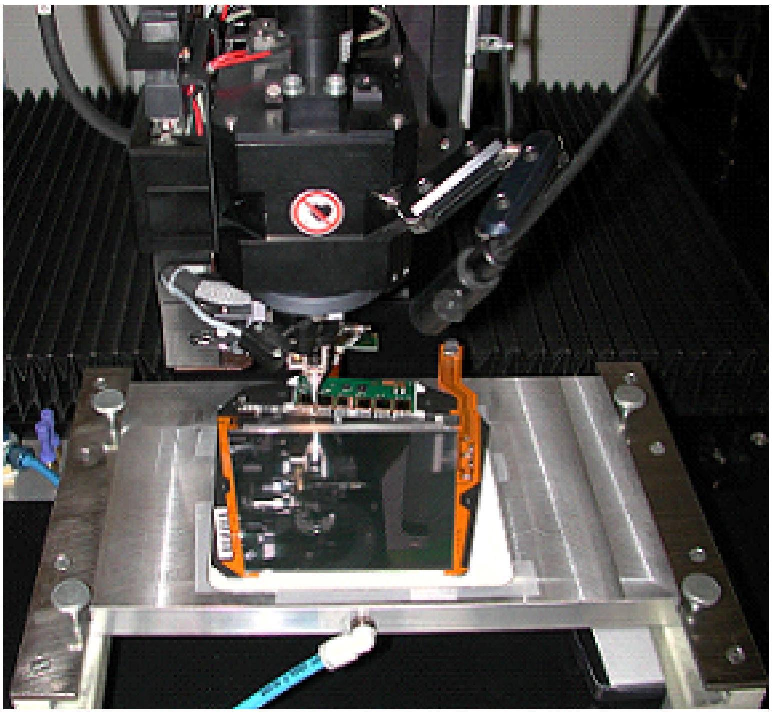

Figure 4.12: A zoom in on the bonding needle and a R2S module on the appropriate jig.

At startup a pull force test was performed for each module, meaning that a destructive pull test was done for every 50^{th} bond. These open connections were certainly rebonded afterwards. After ideal bonding machine settings were found, pull force tests were performed only on a sampling basis (about 1 module/week). It was agreed that the pull strength of each bond has to be above $6g$ with a standard deviation of smaller than 20%.

Results

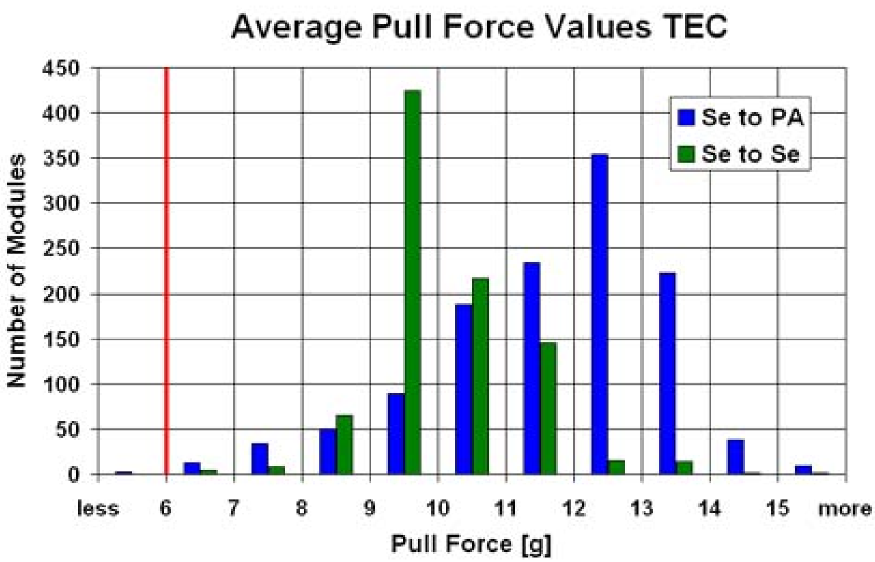

Figure 4.13: Average pull force values of the 1.234 pull tested TEC modules with the according entry in the TrackerDB. Each entry represents the mean value, from all tested bonds, of one module. Modules with an average pull force below $6g$ are considered faulty.

Figure 4.13 shows a plot of the mean values of the pull forces of the TEC modules. Of the 1.234 modules, for which a pull force test was performed and uploaded to the TrackerDB, only 2 modules, 0,16%, have a smaller average pull force than $6g$.

Altogether 36 modules (0,5% of the valid assembled modules) got faulty during the module bonding. 34 of these faulty modules, which are, according to the TrackerDB, not outside the pull force specification, got faulty due to improper handling or had an average pull force below $6g$ but their test was simply not uploaded.

Conclusion

I think that there were far more pull tests performed than uploaded to the TrackerDB. But since the bonding process is highly understood, for me these numbers appear representative. A detailed document that describes the procedures to bond all types of CMS Tracker Modules, including exact informations about bond loop hight and bond length, can be found in [44]. In addition the exact specifications for the jig layouts and the pull tests can be found there.

4.4.3 Backplane Bonding

During the first half of the production an incredible malfunction of the conductive glue was discovered. While measuring the resistance of the connection between the HV bias pad on the kapton foil and the aluminium backplane of the sensor, at some modules resistances above 1 $M\Omega$ were discovered. Intensive tests of these connections were done in Vienna. In a lot of cases the values for the resistance got even worse with thermal cycles, performed as described in the subsection Coolingbox of section 4.4.4. In Figure 4.14 some of these results are displayed.

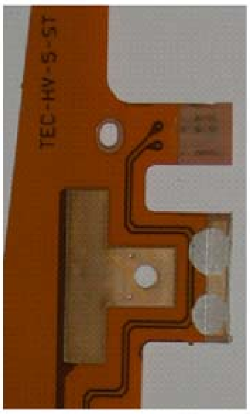

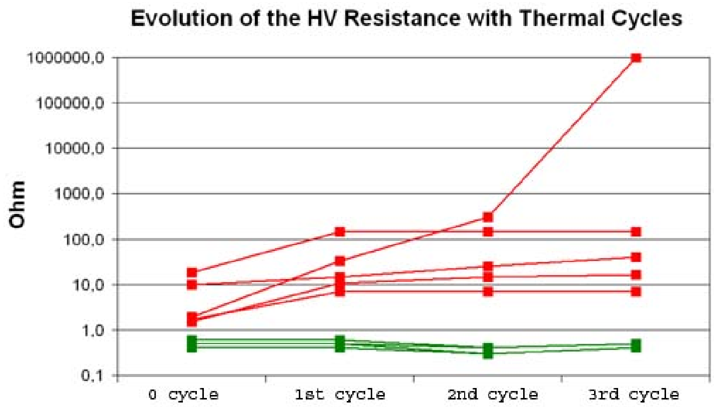

Figure 4.14: On the left picture the originally foreseen small spots of conductive glue between the HV bias connection on the kapton foil and the sensor backplane is shown. This photo was taken from a bad connection after breaking the kapton away from the backplane. Therefore the initial small dots of glue got squeezed very flat. On the right side the resistances of some modules after zero, one, two and three thermal cycles are shown. The red measurements are from modules without glue reinforcement and the green ones from modules with glue reinforcement. The huge resistance increase for the modules without glue reinforcement can easily be seen.

The reason for this problem is the insulating oxide layer on the aluminium surface[11]. Besides the bad electrical contact, there could be a time effect due to oxygen diffusion, which would even worsen the contact. This could, in the worst case scenario, lead to a complete loss of the connection. From the beginning it was obvious, that bonding would be the best thing to ensure a proper connection between the kapton HV pad and the backplane, later called backplane bonding. But the TEC community wanted to be certain, that there exists no other possibility to fix this problem, before introducing the huge additional effort of backplane bonding into the production.

[11]Aluminium in contact with air oxidises and within some minutes an insulating aluminium-oxide layer arises.

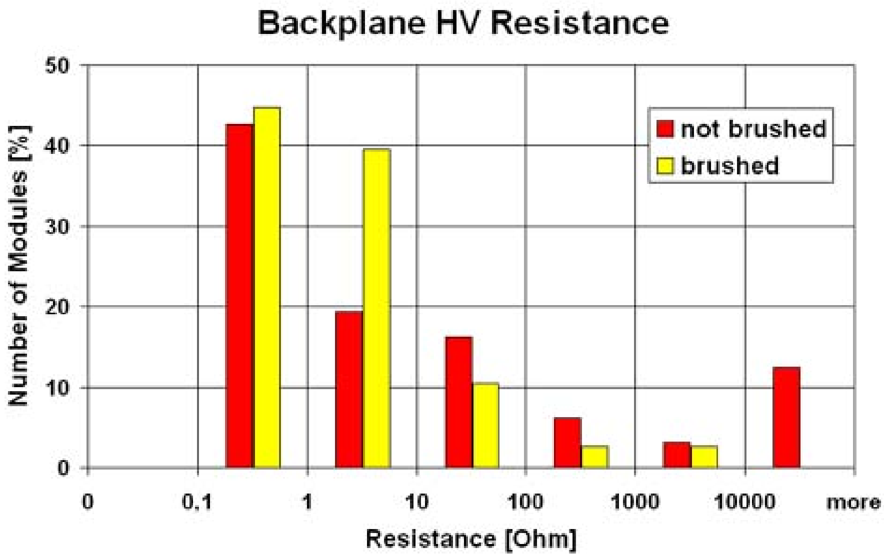

Figure 4.15: Resistance measurements between the sensor backplane and the kapton HV pad. Modules where the aluminium of the backplane was brushed before the conductive glue was applied are shown in yellow. The measurements on the not brushed modules are indicated in red. In this statistic 171 modules are included. On 4 of the not brushed modules, which are not included in this plot, no connection at all could be measured. The backplane resistances of the 2,5% brushed modules with resistances above 1 $k\Omega$ where all below 2 $k\Omega$.

A first attempt was to brush the oxide layer away from the aluminium backplane on the area where the conducting glue should establish the connection. This so-called backplane brushing was performed with a hard paint-brush. A comparison of the brushed and not brushed HV-connection is shown in Figure 4.15, in which 171 modules are included. As displayed in the plot, this procedure did lessen the resistance, but thermal cycles did show, that this improvement was not perfect, since a few of these resistances still increased.

Since backplane brushing did not solve the problem a new procedure was developed, the so called glue reinforcement which is displayed in Figure 4.16 (left). After first problems with the exact procedure, for example it is essential to 'rub the glue into' the aluminium at the backplane, this reinforcement proofed to establish a good connection with low resistances. Certainly this was extensively tested, shown in Figure 4.17, which includes 1.305 resistance measurements of the HV connection with glue reinforcement. Even modules which already had been assembled on a petal were dismounted again to introduced this glue reinforcement retrospectively.

At a later date, the TEC community decided to introduce backplane bonding, as displayed in Figure 4.16 (right), as a standard production step for the remaining modules which where not already mounted on petals. It turned out, that this additional production step was not that delicate and complex as feared. Later on it was even decided to dismount modules from petals for backplane bonding. This was a huge effort, because the modules had to be disassembled in the Petal

Figure 4.16: The left picture shows the HV pad of the capton foil glued to the aluminium backplane of the sensor. The glue reinforcement can easily be seen on the upper edge of this pad. At a later date it was decided to additionally make backplane bonds in the hole of the kapton HV pad, as shown on the right picture.

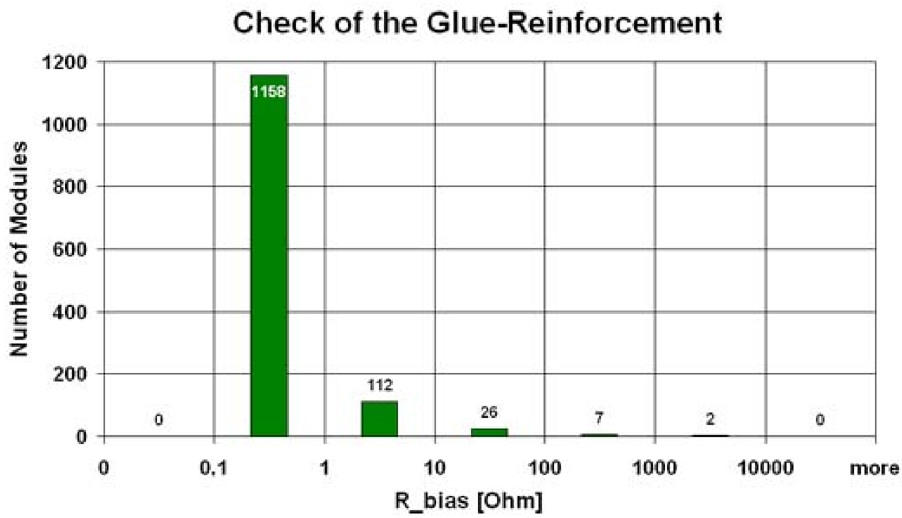

Figure 4.17: This diagram shows 1.305 resistance measurements of the HV connection with glue reinforcement. Most of these connections were at least in one thermal cycle and only 2 of them have values above 1 $k\Omega$ (1,2 $k\Omega$ and 3 $k\Omega$).

Assembly Center by hand and sent back to a Bonding Center where the backplane bonding could be done. Certainly, after this additional bonding a Fast Test and a IV-Curve had to be done with the ARC system for each module before they could be sent back again to the Petal Assembly Centers.

The two finalised TECs contain about 355 TEC modules without backplane bonds, see [45]. Since this number is from September 2006 and in the meantime it was decided do disassembly even more petals, I think that this number will finally be even smaller.

4.4.4 Electrical Tests

The completed modules were tested for various parameters. These tests, as described in the following sections, find faults that are mainly generated by mishandling, during assembly, bonding or shipment and also detect fluctuations in the manufacturing process that did not already show up in earlier quality assurance tests.

ARC System

Functional tests on hybrids and modules are done with the APV Readout Controller (ARC) system. The ARC system was specially developed for the tests of CMS tracker hybrids and modules by the III. Physikalisches Institut B, RWTH Aachen. It provides full hybrid support like power, trigger, clock and slow control and was distributed among all institutes involved in module production. Since all sites used identical testing systems, the uniformity of the test results was improved greatly. A very detailed description of the ARC System is given in [46].

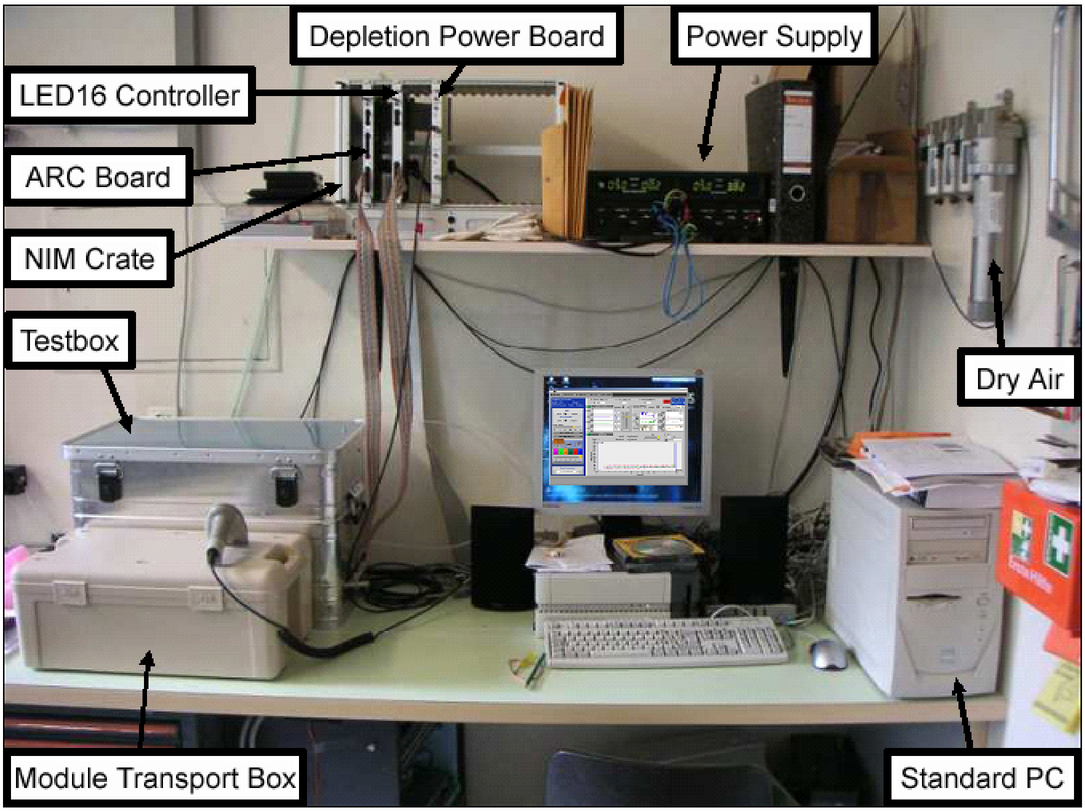

Figure 4.18: This picture displays the ARC test setup as used in Vienna. Its parts are labeled here and seperately described in this section.

Hardware

The test setup as used in Vienna is shown in Figure 4.18 and is composed of:

- APV Readout Controller board
  It is the heart piece of the ARC System and houses the core electronics for the tests. This six layer printed circuit board in double euro format (160 $\times$ 233 mm^2) can be placed into a 19" crate. It is supplied by two voltages, -5 V and +5 V, from a standard power supply and requires currents of approximately 60 mA and 1,4 A, respectively. It digitizes the analog data from the APVs, provides clock and trigger signals and monitors and controls all the chips on the hybrid via several I^2C controller. It is possible to control two modules simultaneously with one board.

- PCMIO Interface Card
  This card serves as the interface between the ARC board (flatband cable) and a PC (standard ISA slot) running the ARC Software.

- Front End (FE) Adapter
  This board is connected to the hybrid via the Hybrid-to-VUTRI adapter card on one side and to the ARC board via a 26 pin flat cable on the other side. It is located directly inside the test box and houses all components of the readout and slow control that would suffer from voltage drops along the supply lines.

- Light Emitting Diode (LED) System
  This system provides the opportunity to test modules with externally generated signals. Signals are created via infrared light which generates electron-hole pairs in the detector volume. It consist of three parts, a LEP16 board, a LED box and an emitter. The LEP16 board fits into a 19" crate and requires the same power supply as the ARC board. It controlls the LEDs which can be either continuously powered or pulsed. The LED box houses 16 infrared LEDs where each is coupled to four optical fibers. This 64 optical fibers are supported by the emitter in a pitch of 2 mm directly above the sensor.

- Depletion Power (DEPP) board
  It also fits into a 19" crate and requires the same power supply as the ARC board. It supplies the modules with the high voltage of 400 V required to deplete the silicon strip sensors. It enables to adjust and make measurements with voltages in steps of 0,15 V in a range of 0 V to 600 V.

- NIM Crate
  A standard Nuclear Instrumentation Module (NIM) crate serves as a save place to store the ARC board, the LED16 controller and the DEPP power supply.

- Power Supply
  A standard power supply (in Vienna of the type EA-PS 2316-050) is used to power the three needed boards (ARC-, DEPP- and LED-board).

Figure 4.19: The left picture shows a look inside the Vienna ARC Testbox containing a R2S module mounted on a transport plate, the LED emitter and the front-end adapter. The right picture shows a look inside the Vienna Coolingbox where the simultaneous thermal cycling of up to 9 modules is possible.

- PC
  A standard windows PC which provides a ISA slot and runs the ARCS Software.
- Testbox
  This box has to be absolute light tight and humidity controlled. It serves as electromagnetic shield and needs a proper grounding scheme, so that the noise level of the test boxes from different institutes is comparable. It houses the module on its transport plate, the LED emitter and the front end adapter, as displayed in Figure 4.19 (left).

Coolingbox

In addition to the hardware above, each testing facility is equipped with a Coolingbox to perform thermal cycles. A picture of the Vienna Coolingbox can be seen in Figure 4.19 (right). A thermal cycle includes at minimum three alternative coolings to -15$°C$ and heatings to +40$°C$. The main purpose was to make sure, that the modules can withstand the thermal stress put on them, when they are cooled down to the operation temperature of the Tracker of -10$°C$ and the heating back to room temperature during service intervals. In the startup phase each module was ARC-tested before and after the thermal cycle, mainly to see if bonds get loose due to the thermal stress. Early in the production problems with the conductive glue appeared: when there was not enough glue between the silicon backplane and the carbon fiber it happened that the backplane connection completely broke off. Then, later in the production, the Coolingboxes were extensively used to perform the tests on the backplane-glue-reinforcement and then again to test the backplane bonds.

Software

The APV Readout Controller Software (ARCS) is a Labview 6i application that serves as graphical user interface in the module and hybrid test setup. It is able to read all information provided by a module via the I^2C bus, to run several measurements on the module, to interpret the results and to write these results in an *.xml*-file which allows an easy upload to the TrackerDB. To interpret the results different fault finding algorithms are implemented. The ARC Software provides the opportunity to run a quick Fast Test or a Deep Test. A detailed description of the ARCS Software can be found in [47].

Module Tests and Failures

With the help of the ARC System, module failures can easily be detected. The required tests for the module qualification and fault finding are the following [48]:

- Fast Tests
  This is a row of short measurements to check the functionality of all ICs on the hybrid (APV, DCU, MUX and PLL) described in section 3.4. To get a correct output, this test has to be performed at 400 V. Any failure would indicate a major problem for an entire chip.

- IV Test
  This test takes an IV curve of the module. The sensor bias voltage gets ramped up to 450 V at a rate of 10 V/s. Problems with the HV supply line and in the silicon itself can be revealed. Every module with a leakage current at 450 V above 10 μA per sensor is considered as unusable.

- Pedestal & Noise Test
  This test has to be performed in all four modes, Peak Inverter Off, Peak Inverter On, Deconvolution Inverter On and Deconvolution Inverter Off. At first the pedestals (the electrical zero point) for each channel is measured several times and the average gets calculated separately. Then the noise picked up by each channel for 2.000 events must be taken in each mode. Afterward the Common Mode (CM) correction is applied to the data. During this correction, the average noise of a bunch of 32 adjacent channels is calculated and the result subtracted from the noise of each channel respectively. This eliminates influences that effect several channels. To be considered a good test, the common mode subtracted noise in Peak Inverter Off mode must be less than 0,4 ADC counts[12] for one- and less than 0,5 ADC counts for two-sensor modules. With this test Opens, Shorts, Pinholes, noisy channels and saturated channels can be detected.

- Pulse Shape Test
  In this test the amplitude and peaking time of the calibration pulse for each channel is measured separately. This is done via APV intern charge injections into one channel at a time. For channels with bigger capacities

[12] Measurements in Vienna showed that 1 ADC count corresponds approximately 770 electrons.

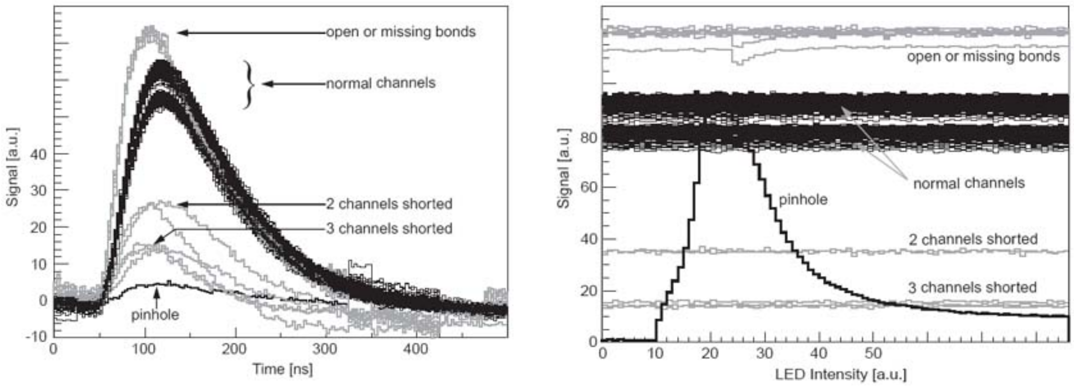

Figure 4.20: The left plot shows a Pulse Shape Test of a two-sensor-module with the behaviour of different faults. On the right side the Pinhole (LED) Test of the same module is given. These plots are taken from [49].

the pulse height is reduced and the peak time, the time to reach its maximum pulse hight, is extended. It is also performed in all four modes at 400 V. A Pulse Shape Test of a module with different faults can be seen in Figure 4.20 (left). Opens have a higher pulse height and a faster rise time, Shorts have approximately half the nominal pulse height and Pinholes or saturated channels show almost no response to charge injections.

- Pinhole (LED) Test
  This test is only performed in Peak Inverter Off mode. APVs connected to a pinhole have a virtual ground at the voltage of the p^+-implant. In the pinhole test, the LED array is used to induce an increasing leakage current in the bulk, which increases the voltage drop over the external resistors in the HV power return line and the poly-silicon resistors. With the proper leakage current, no current flows out of the APV and the pinholed channel becomes unsaturated. At this point, the channel will have a normal response to the internal calibration circuit which means that the calibration pulse height matches that of a normal channel. At higher LED intensities the channel becomes saturated again and a lower calibration injection is seen. The signal of a Pinhole and of various other faults is displayed in Figure 4.20 (right).

- Pipeline Test
  It is sufficient to perform this test in Peak Inverter On mode. The APV pipeline test has the potential to find bad pipeline capacitors which, for example, could be responsible for noisy channels.

During all these tests the relative humidity (RH) should not be greater than 30%. This specification was provided by the sensor group because any test performed above 30% RH can have surface current effects which can cause extremely large noise and/or currents.

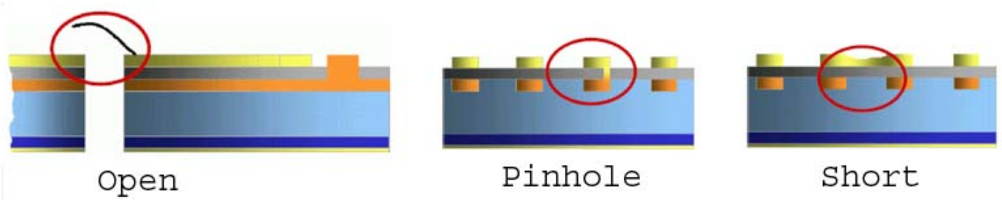

Figure 4.21: Drawings of an open channel, a pinhole and a short between two channels. The illustrated short is between two aluminium readout strips, but can also exist between two implanted p$^+$-strips. The n-bulk is colored in blue, the p$^+$ implants in orange, the SiO_2 layer in gray and the aluminium readout stripes in yellow.

With the help of these tests, as shown in Figure 4.20 for the Pulse Shape Test and the Pinhole (LED) Test, the following faults can be detected:

- High Bias Current
  This defect can be seen in the IV test and can be caused by defects in the bulk material or scratches on the sensor surface.

- Open Channels
  In general opens are considered as channels which are not (fully) connected to the readout electronics, either due to a missing bond, sketched in Figure 4.21, or to substantial damage of a readout strip (e.g. a scratch that cuts the aluminium). Open channels put a significantly reduced capacity load on the APV, and since the noise of the channel increases linearly with the load capacitance, they can easily be detected. In addition smaller capacitances induce faster rise times and higher pulse heights. In the case of two sensor modules, opens can be classified as sensor-sensor-opens and pitch adapter-sensor-opens.

- Pinholes
  These are shorts between the p^+-implant and the aluminium readout strip, as outlined in Figure 4.21. Thus the APV input line is resistively coupled to the p^+-implant. These defects in the insulation layer can be generated during the manufacturing process, by scratches on the sensor or during bonding with wrong bonding parameters. Via a pinhole the load of the sensor signal is directly put on the corresponding APV. The whole APV can be saturated when it is connected with too many pinholes. A pinhole has a very low (nearly zero) noise and calibration injection pulse height.

- Shorted Channels
  Shorts are electrical contacts between two readout channels. This can be caused by a defect in the insulation layer between p^+-implants or a connection between two aluminium strips, as displayed in Figure 4.21. Other reasons are twisted bonds, dirt (i.e. glue), or scratches on bond pads and strips. Shorted strips share the APV intern charge injections, that are injected into one channel at a time during the Pulse Shape test, among them. Thus a short of two channels will reduce the normal signal height to one half and

a short of three channels to one third. In addition the noise for each of the shorted strips is reduced and has a very similar value for all channels within one short.

- Dead Channels
  Dead channels act in many aspects like pinholes as they show no response to any charge signal. The main difference to pinholes is, that they also show no response to a calibration signal at any leakage current.

- Defect Inverters
  As shown in Figure 3.14, the inverter is part of every single APV channel. Defect Inverters become obvious, as they show a different behaviour in tests that are performed once with activated and once with deactivated inverter. This defect can easily be seen by a significant difference in the Pulse Shape test.

- Defect Pipeline Cells
  Even one single defect pipeline cell, i.e. a defect pipeline capacitor, out of the 192 cells belonging to one channel, can be detected via the pipeline test.

- Noisy Channels
  These are channels with an increased noise. Special noise cuts were introduced for APV edge channels, which often have a slightly increased noise due to crosstalk effects between adjacent APV edge channels. Although channels with an increased noise can be used for readout, they are counted toward the total number of faulty strips of a module.

- Micro-Discharges
  A channel with micro-discharges creates a very large noise above a certain bias voltage applied to the sensor. This noise is attributed to localized peaks in the electric field which can cause avalanche effects. The influence of such a noisy strip is not limited to its neighbours, even the noise of the whole APV can be effected. This makes the task of identifying these strips quite difficult, but after the appropriate bond is removed, the noise of the other channels normalize in most cases. In addition the total leakage current of the module can hugely be increased by a saturated channel, like shown in Figure 4.22.

- Unknown Faults
  Any conspicuousness that can not be associated to types of faults mentioned above, is listed by the ARC System as an 'unknown fault'. For example a low or high pulse height or peak time due to a failed fit or a channel with a low noise in only one of the APV operation modes without any further conspicuousness. For modules with these faults the test operator has to decide individually the further procedure.

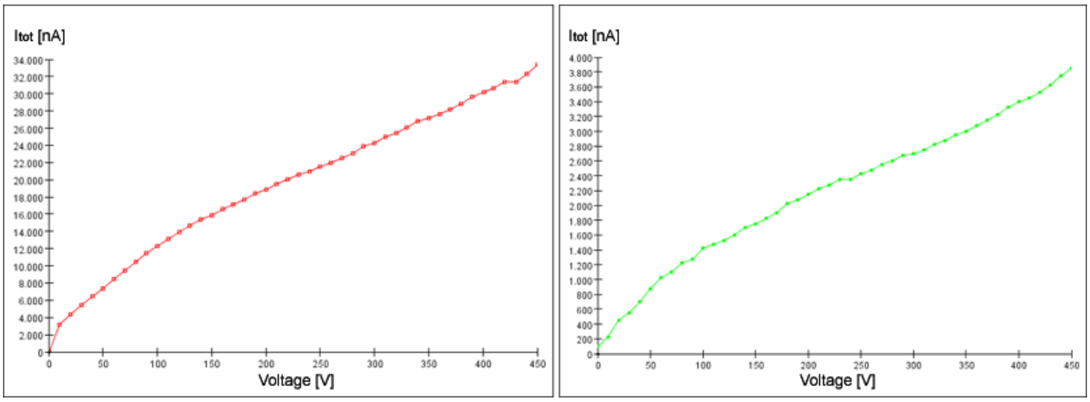

Figure 4.22: These two plots show the IV-curve of the R7 module 30200020010689 before (left) and after (right) the removal of the pitch adapter to sensor bond of the saturated channel #136. The leakage current at 450 V was 33,4 μA when the saturated channel was electronically connected to the APV and after the removal of the appropriate bond it decreased to 3,9 μA.

Results

Here the statistic of the faulty modules after the module production, before the modules were sent to the Petal Assembly Centers, are presented.

The specifications for the electrical tests are:

- Modules with a leakage current at 450 V above 10 μA per sensor are considered bad (Grade C). In numbers: 10 μA for one-sensor-modules and 20 μA for two-sensor-modules.

- Modules with a number of bad channels (like pinholes, opens or dead channels, noisy channels, shorted or saturated channels, ...) above 2% of the total number of module channels, are faulty (Grade C). In numbers, more than 2% bad channels for a module containing 4 APVs (512 channels) is 11 or more and for a module with 6 APVs (768 channels) is 16 or more.

- In addition to the two cuts for faulty modules, another Grade was introduced to mark spare modules: Grade B. These are modules with a number of bad channels between 1% and 2% and a leakage current at 450 V between 3 μA and 10 μA per sensor. But due to maintenance problems during the module production, mostly because of delays in the hybrid manufacture, and the huge number of modules that got faulty after the production, some Grade B modules were mounted on petals.

Figure 4.23 and Figure 4.25 display all TEC modules with an appropriate TrackerDB entry. The numbers in these plots do not represent the finalised TEC module production. The reasons, why not all ARC tested modules are included in the plots, are:

- incomplete ARC tests
  Especially in the startup, some institutes had problems with the upload of

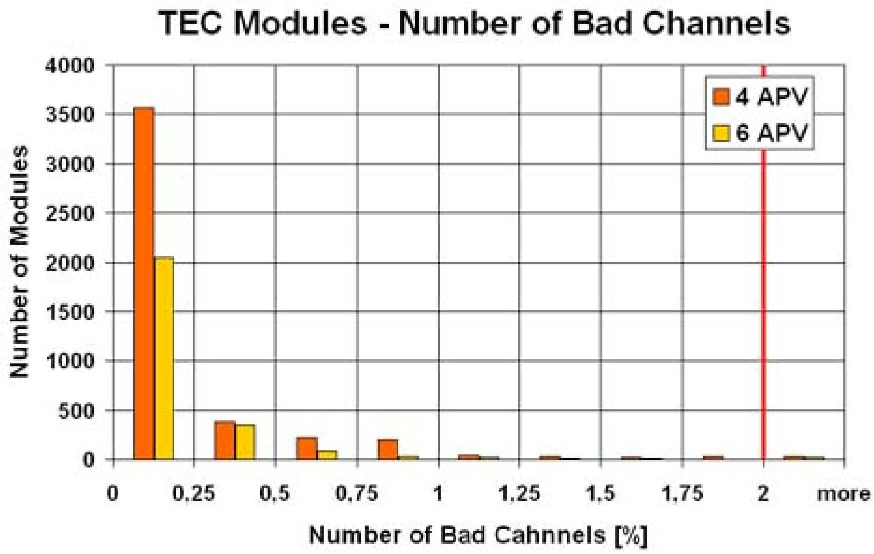

Figure 4.23: Number of TEC modules containing the different percentages of bad channels. This plot displays the 7.120 modules, which have a 'number of bad channels'-entry in the TrackerDB after the last module production step (before they were shipped to the Petal Assembly Centers). At this stage only 57 modules, 0,8 % of the modules with a TrackerDB entry, had more than 2% bad channels, and were therefore considered Grade C. In orange modules with 4 APVs (512 readout channels) and in yellow modules with 6 APVs (768 readout channels) are displayed.

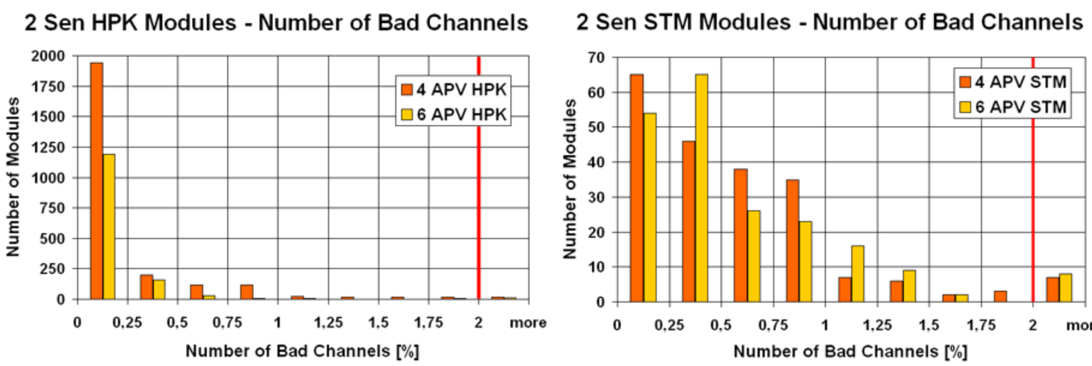

Figure 4.24: Percentage of bad channels displayed only for the two sensor modules. The quality difference for modules containing HPK-sensors (left) and for modules containing STM-sensor (right) is immense.

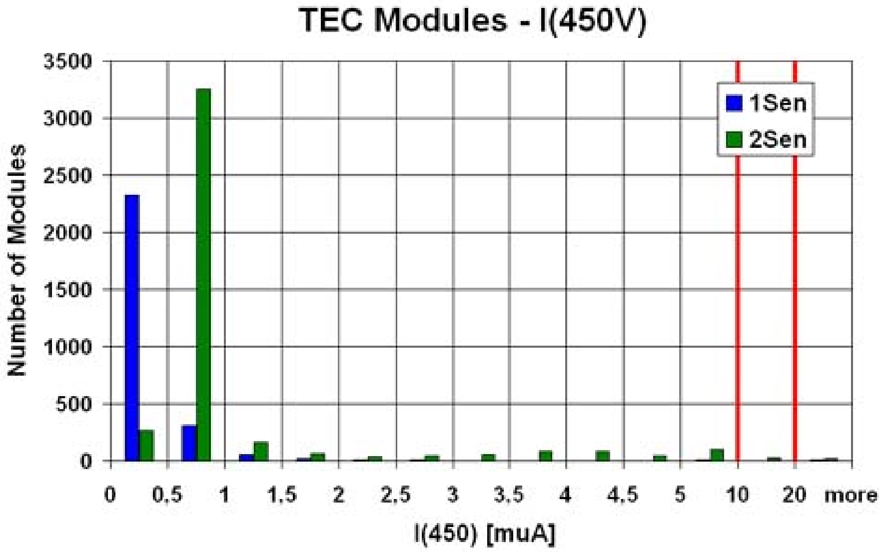

Figure 4.25: Diagram of the leakage currents at 450 V of the TEC modules. This plot displays the 7.002 modules, which have a 'I(450 V)'-entry in the TrackerDB after the last module production step (before they were shipped to the Petal Assembly Centers). At this state only 31 modules, 0,44 % of the modules with a TrackerDB entry, had a too high leakage current at 450 V, and are therefore considered Grade C. In blue modules containing one sensor (cut at 10 μA) and in green modules with two sensors (cut at 20 μA) are displayed.

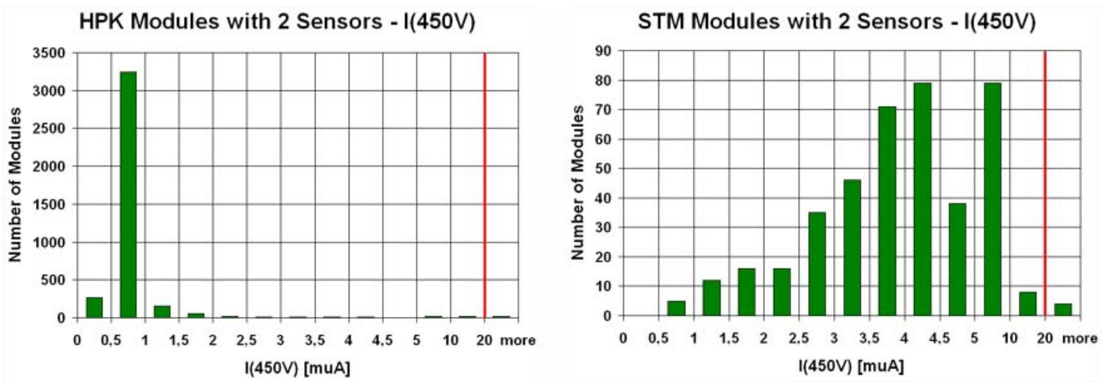

Figure 4.26: Leakage currents at 450 V displayed only for the two sensor modules. The quality difference for modules containing HPK-sensors (left) and for modules containing STM-sensor (right) is again immense.

the complete ARC-test data. For example the *.xml*-file generator of the ARC software prior to version 7.2 did not work proper and the *.xml*-files had to be created with an additional software like xFLAG.

- Fast Test fails
  It is possible, that some institutes did not perform the ARCs Deep Test, after a Fast Test in advance failed. When only the Fast Test is uploaded to the TrackerDB, no values for the 'Number of bad channels' and the 'current at 450 V' exist.

- complete current breakthrough
  A module has a complete breakthrough, when its leakage current reaches more than 50 μA before the voltage was ramped up to 450 V. In this case the ARCs Deep Test stops and no continuative tests are performed. Then no information about the current at 450 V and the number of bad channels is written to the *.xml*-file and in consequence the appropriate values do not exist in the TrackerDB.

- faulty electronics
  Possible problems with some hybrid parts can make a module faulty. For example with a failure in the I^2C communication no proper ARC test can be performed.

- via problems
  Modules with via problems, like described in chapter 4.3, were tested normally before this problem was detected. These modules are not included in all statistics presented in this thesis.

From the two Plots, Figure 4.24 and 4.26, it can easily be seen, that the quality of the modules containing HPK-senors is much better than that of modules containing STM-sensors. Since STM-sensors were only used to build two sensor modules in these plots only the HPK modules with two sensors are considered. 0,96% of the two sensor modules containing STM-sensors and only 0,39% of the two sensor modules containing HPK-sensors were outside the specification for the leakage current (I(450V) < 20 μA). The same is true for the specification for the number of bad channels (< 2%), where 3,17% of the two sensor STM modules and only 0,64% of the two sensor HPK modules lie outside. This reflects the minor quality of the STM-sensors, which led to problems during the module production. In the middle of the production, the sensor manufacturing of most sensors was moved from STM to HPK. Thus only about 400 modules have been build with STM sensors.

Out of the 4.091.392 readout channels, which are on the 6.762 good ARC tested modules, only 8.263 or 0,2% channels are considered bad. This can be seen in Figure 4.27 where the noise of every readout channel of all TEC modules is displayed[13]. A huge part of these bad channels consists of noisy channels, which are not completely useless. Since, in this number even spare modules are included,

[13]This plot also includes the faulty modules.

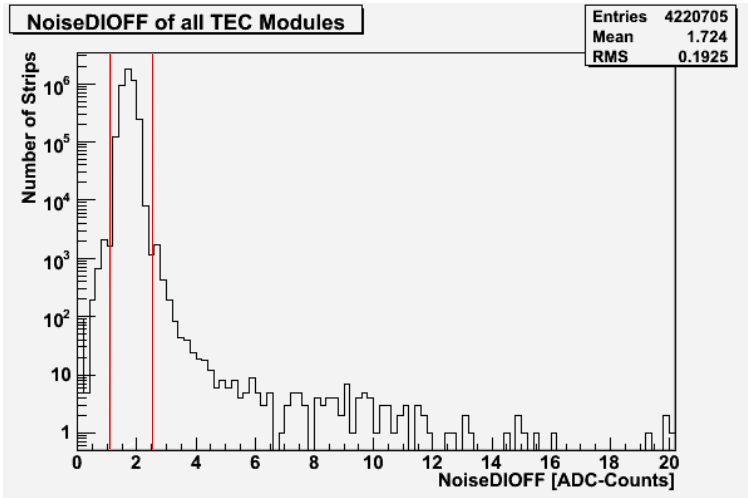

Figure 4.27: Noise of all single TEC module strips in Deconvolution Inverter On mode. The red lines indicate the mean-values of the noise cuts, which are slightly different for each module geometry. Strips with a noise below the left cut are with decreasing noise: opens between sensor and APV, opens between two sensors and pinholes. Strips with a noise above the upper cut are with increasing noise: noisy channels and saturated channels. Above 20 ADC counts only a few isolated entries exist. As mentioned before, 1 ADC count corresponds approximately 770 electrons.

which generally are of inferior quality, the finished Tracker End Caps do contain for sure less than 0,2% bad readout channels.

The final numbers of the TEC module production are given in Table 4.5. Out of the 7.140 modules, which have at least one uploaded ARC-test, only 7.120 have a 'number of bad channels'-entry and only 7.002 have a 'I(450 V)'-entry in the TrackerDB. Thus only 80 modules are electronically faulty in the TrackerDB; 57 for their number of bad channels and 31 for their too high current at 450 V (8 modules are outside both specifications). Thus 298 faulty modules are missing in the two plots.

Conclusion

As mentioned above, some data in the TrackerDB is incomplete or missing. The reason for this is, that the usage with and the concept of the ARC-system and the TrackerDB was not always ideal. At the startup of the module production, huge problems existed with the upload of the data, since the upload of the $.xml$-files was quite complicate. An improvement, especially for this statistic, would have been some general rules for putting additional information into the data base. Another problem was the impossibility to change existing tables or to implement new ones so that structural deficits could have been corrected.

In order to produce a statistic on faulty modules an additional data base, the so-called Faulty Modules Database, with more detailed information had to be generated at HEPHY Vienna, see Section 5.1.

4.5 Summary of the Module Production

Here the finalised numbers of the module production are given. The final results of the TEC module production are excellent and it could be finished in September 2006. It was accomplished to produce the targeted 6.781 good TEC modules (6.400 needed plus 6% spares) to build the two Tracker End Caps. This would have never been possible without the accurate quality assurance procedures for the single module parts before their assembly and the exact defined procedures for each production step.

The numbers of the module production (status September 2006) are summarised in Table 4.5. It can again be seen that for some modules the information

status	number of modules	
assembled	7.228	
outside specs (DB)	36	(0,50%)
total lost during assembly	52	(0,72%)
bonded	7.176	(99,28%)
outside specs (DB)	2	(0,03%)
total lost during bonding	36	(0,50%)
ARC-tested	7.140	(98,78%)
good ARC tested	6.762	(93,55%)
bad for IV (*)	31	(0,43%)
bad for NBadChan (*)	57	(0,79%)
total faulty (ARC)	378	(5,23%)
total good	6.761	(93,54%)
total bad	467	(6,46%)
TEC needed (must)	6.400	
+ 6% SPARES	6.781	

Table 4.5: The final numbers after the module production. In brackets the percentage from the total 7.228 assembled modules is given. In September 2006 the goal to produce a total of 6.781 good TEC modules (including 6% spares) could be achieved. ((*)...8 modules are outside both specifications)

why they got faulty is missing. I think that most of these modules which got faulty by other reasons than lying outside the specifications, got faulty due to improper handling. The most probable reasons for these undefined faulty modules from the different production steps are described in the appropriate sections above.

4.6 Petal Integration

In total 288 substructures, the so called petals, are needed to finish the two Tracker End Caps. Figure 4.28 displays a Side A of a front petal. The modules got mounted on these petals in the six TEC Petal Integration Centers (PICs) which were located in Aachen, Brussels, Karlsruhe, Louvain, Lyon and Strasbourg. Each of the PICs took the responsibility for one of the six groups of petals. These groups consist of front or backside petals for the carbon fibre discs 1-3, 4-6 and 7-9. Figure 4.29 shows a technical drawing of one of the nine discs needed to complete one TEC.

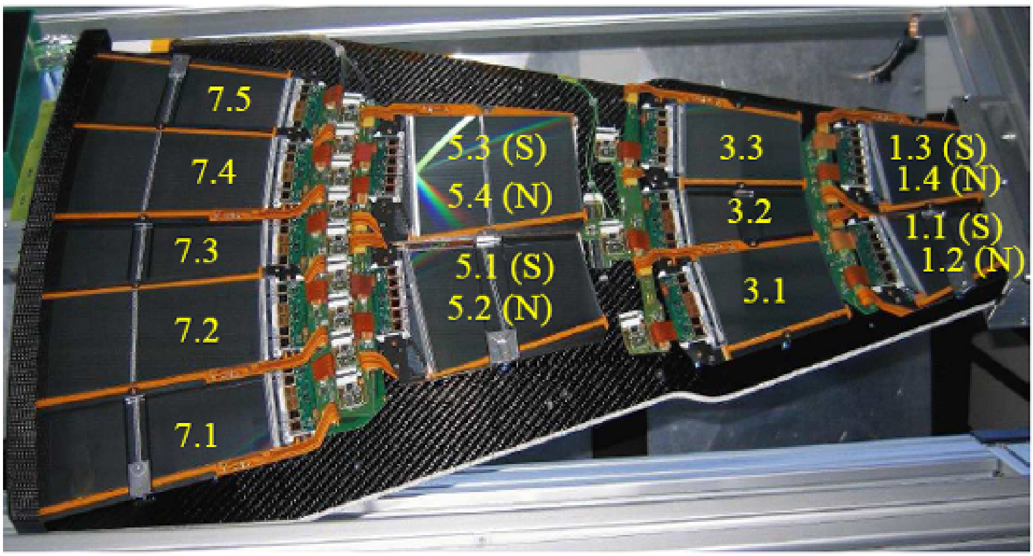

Figure 4.28: Side A front petal including the numbering scheme of the silicon strip modules. From the double sided modules the stereo module is visible with the normal module underneath.

4.6.1 Parts of a Petal

Each petal consists of about 400 single pieces (including bridges, washers, screws, distance pieces, ...). Its main components are:

- Digital Opto-Hybrid Modules (DOHM)
  Via the DOHMs, the digital informations like clock, trigger and slow control are brought from the outside of the Tracker to the communication and control units (CCU) on the petals.

- Communication and Control Units (CCU)
  With the help of the CCUs the analogue data is transmitted unidirectional. They are organised in a ring like architecture so that a set of CCUs can share one DOHM.

- Analogue Opto-Hybrids (AOH)
  They convert the analogue output of the modules into optical signals for off

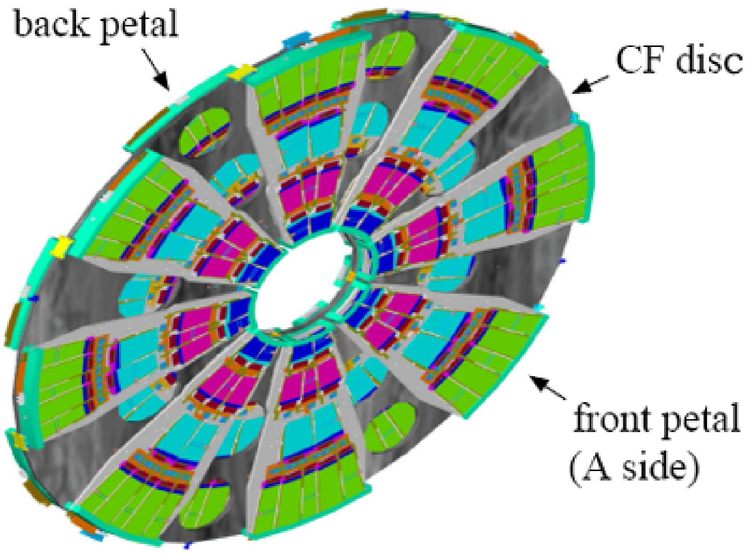

Figure 4.29: Technical drawing of one disc of the TECs with the interaction region to the right. Here only the ‘A side’ of the front petals, with ring 1 (dark blue), ring 3 (purple), ring 5 (light blue) and ring 7 (green) is visible.

detector digitization. They where designed and tested by HEPHY Vienna and produced by KAPSCH in Vienna. For each petal up to 28 AOHs are needed.

- Modules
  They are described in detail in the sections above. As displayed in Figure 2.3 the inner module rings are not present on all discs. Only discs 1 to 3 carry all seven rings as listed in Table 4.6. On the discs 4 to 6 ring 1 is missing, on discs 7 and 8 the rings 1 and 2 are missing, and on disc 9 only rings 4 to 7 are present. Front petals (FPs) are a bit broader and carry up to 28 modules, back petals (BPs) carry up to 23 modules.

  To obtain tracking information in the radial direction, double-sided modules are used for rings 1, 2 and 5. Each of these consists of a normal module (with the strips running in radial direction) and a stereo module. The two modules are mounted back to back such that the strips of the stereo module are rotated by 100 $mrad$ with respect to the strips of the normal module.

- Support Structure
  The silicon modules are mounted onto wedge shaped carbon fiber support plates, so-called petals, for a more easy handling and mounting on the carbon fibre (CF) discs. On each of the CF discs, eight front petals are mounted on the side that faces the interaction region, while eight back petals are mounted in the ϕ-gaps between the front petals on the other side of the disc.

- Cooling Pipe
  Each petal contains a 7 m long thin walled titanium cooling pipe (coolant: C_6F_{14}). With their help the modules get cooled down to the operational

	front petal		back petal	
modules	Side A	Side B	Side C	Side D
R1N	2	-	1	-
R1S	2	-	1	-
R2N	-	2	-	1
R2S	-	2	-	1
R3	3	-	2	-
R4	-	4	-	3
R5N	2	-	3	-
R5S	2	-	3	-
R6	-	4	-	3
R7	5	-	5	-
maximum	15	12	15	8

Table 4.6: Number of modules per ring needed for both sides of front and back petals. As mentioned in the text only the petals of discs 1, 2 and 3 carry all rings. (R...Ring, N...Normal, S...Stereo)

temperature of -10°C. Each module is directly mounted onto the cooling pipe via four aluminium pins. This provides the mechanical precision for each module on the petal, with a maximum deviation of 5 μm, and the thermal contact of the modules to the pipe.

- The Inter Connect Board (ICB)
  This motherboards are mounted on both sides of the petal and bring power, timing and control signals to the electronic devices (e.g. modules, AOHs, CCUMs).

4.6.2 Functionality Tests

The first thing, the Petal Integration Center had to do after receiving the already tested modules from the Bonding Centers, was to take an IV-curve of the module and to perform a Fast Test with the ARC System. During the assembly of the different parts on the petals various functionality tests had to be performed. Because of the high density of fragile components these tests were done after the mounting of each single component. At first the CCUMs and Opto-hybrids were mounted and tested. Then the non-overlapping modules of each ring got installed and an I^2C scan, a pedestal and a noise analysis were performed, before the second module layer got mounted. This procedure was repeated till a power group was completely installed and tested. Then the integration of the next power group started following the same procedure. Afterward a long term test inside a dry storage, including several thermal-cycles, was performed for each completed petal.

4.6.3 Beam Tests

In May/June 2004, a full TEC control loop, consisting of a front and a back petal (together including 51 silicon modules), was operated and tested in muon and pion particle beams at CERN. During these tests, performed both at room temperature and at temperatures comparable with the CMS operating conditions, the control loop showed an excellent performance. The setup and the results for these tests are described in detail in [50].

4.6.4 Conclusion

Although a lot of modules got faulty during the petal integration, in the end the two TECs could be finished. The majority of these modules got faulty due to touched bonds and could, with a huge effort, be repaired. More about the faulty modules is presented in chapter 5.

In the moment cooling tests are performed on the two Tracker End Caps in the Tracker Integration Facility (TIF) at CERN. When everything goes well, they will be integrated into the Tracker in February 2007. Then finalising tests on the whole system will be performed, before it will be lowered into the CMS cavern and installed in the heart of the Compact Muon Solenoid.

Chapter 5

Faulty Modules

Out of the 7.228 produced modules[1] 809 (11,2%) have at least one repair entry in the TrackerDB. The huge amount of time and effort which was invested to recover the faulty modules gets obvious in Figure 5.1, where the percentages of faulty modules is shown on a weekly basis. In the end of the petal production 467 modules, 6,5% of the assembled modules, remain faulty after all repair actions. 222 of these faulty modules have been disassembled again, the sensors were recuperated and they were used to build new modules. Hence only 3.4% of the assembled sensors were lost in faulty modules.

5.1 Faulty Modules Database

To make a correct analyse of the problems during the module production, it is essential to know the exact reason, why the different modules got faulty. It was not possible to extract this information out of the TrackerDB, because such an analysis was not foreseen during the construction of the TrackerDB. A first approach to handle this issue was done by Salvatore Costa, who created the 'CMS Tracker Module Failure Report User Interface', which allows to report failures and to publish diagnoses into the TrackerDB. In addition it enables to easily retrieve these informations again from the database. The big problem of the interface is, that not all institutes were willing to use this interface properly, and the failures were not consistently described. All together 461 modules got at least one entry via this failure interface.

To get a clue and to properly perform an analysis about the faulty TEC modules Thomas Bergauer and Marko Dragicevic created a MySQL data base. In this so-called Faulty Modules Database every single faulty module was allocated by hand into the different categories and was flagged at least with one problem out of the list below. The Faulty Module Categories give an overview about the number of usable modules and the different Faulty Modules Problems give a deeper insight into the reasons why the different modules got unusable. Again, modules containing hybrids with via problems and from bad batches are not considered.

[1]Modules containing hybrids from bad batches or via problems are not included.

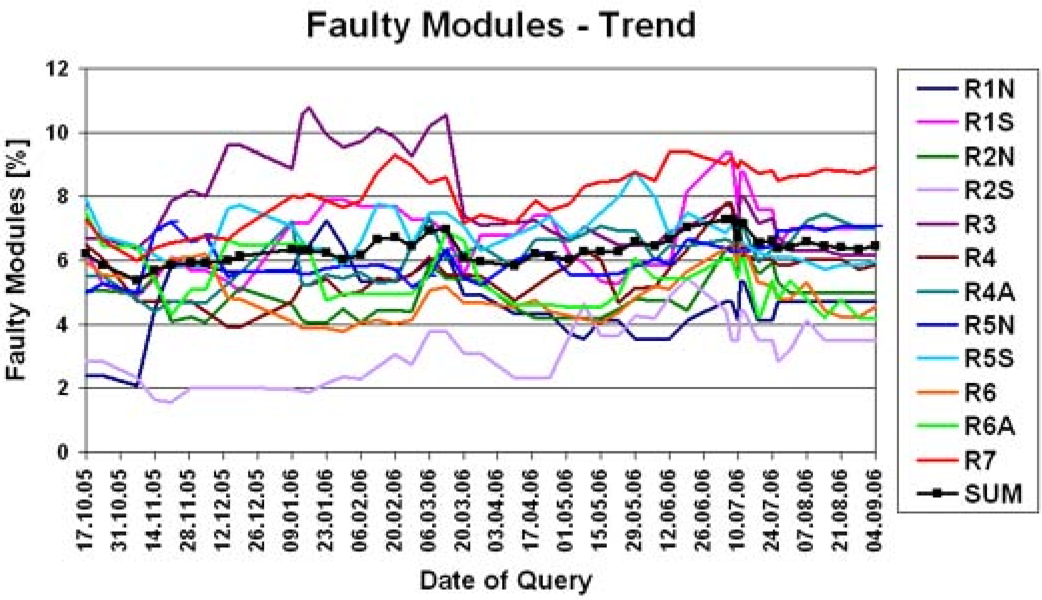

Figure 5.1: The evolution of the faulty module percentages separated for each TEC geometry. The x-axis shows the date when the data was extracted from the TrackerDB. From the up and down of each line a feeling about the huge effort, which had to be done for repairs, gets obvious. The reason why not a single geometry is stable below 4% is, that even the disassembled modules, where the sensor could be recycled, are included. (For example the huge correction of the R3 modules in the week between 13.03.06 and 20.03.06 was achieved, because Wolfgang Braunschweig was able to repair 17 R3 modules with cracks in the carbon frame positioning holes.)

Faulty Modules Categories

The Faulty Modules Categories were introduced to provide a quick overview of the number of usable modules out of the Faulty Modules Database. This information was essential for the last possible order of HPK-sensors, which had to be done while the module production was not finished.

- Soft Problem
  Modules slightly out of cuts, e.g. slightly outside the gantry mounting specifications or sensors with a leakage current slightly higher than 10 μA at 450 V. Modules with an ARCs readout problem possibly caused by a specific ARCs setup or modules containing sensors with a too high leakage current due to humidity problems. The main character of these faulty modules is, that they are not complete losses and usable as spares.

- Repairable
  Modules that have a good chance to be repairable, e.g. some broken or twisted bonds. The repair of these modules needs some time consuming action and mostly includes shipments. The idea was to store these modules and to only repair them if urgently demanded.

- Sensor Recuperation
  Modules containing a mechanically or electronically broken hybrid and/or frame. Since the amount of sensors was the limiting factor of the module production, it was decided to unmount and reuse sensors of faulty modules wherever possible.

- Hybrid/Frame Recuperation
  Modules with a mechanically or electronically broken sensor. This category only was created for the case of a shortage of hybrids and frames, which fortunately never occurred.

- Lost
  Modules where every single part is completely lost. All modules of this category, which are optically ok, are used as exhibition samples. Even two complete exhibition petals could be assembled out of these lost modules.

Faulty Modules Problems

Altogether 475 module faults, the so-called module problems, could be identified. This number is slightly higher than the total 467 faulty modules because some modules got flagged with more than one problem, like for example modules with touched hybrid and touched sensor bonds. Also keep in mind, that 222 of these modules were disassembled and their sensor recycled. The final number of faulty modules after the petal production including all repairs are listed below. In Figure 5.2 and in the list below the number of modules, faulty because of the specific reason, is given in brackets.

- IV Problem (108)
  Modules with too high leakage currents (sometimes even complete IV break-throughs) or a strange IV behaviour. Some of the modules with this fault could be repaired when the reason of the fault was not the sensor, e.g. a faulty capacitor on the kapton circuit or a too high leakage current due to a humidity problem. Since all the sensors were tested prior to the module assembly, this number clearly points to mishandling during module production and during petal assembly.

- Touched Bonds Hybrid (78)
  Modules with touched or broken hybrid to APV or APV to pitch adapter bonds. This problem simply appeared due to careless handling and the reason, why so many modules were lost due this reason is described in section 5.2. The majority of these modules got disassembled.

- Hybrid Component (72)
  Modules which contain a hybrid with a confirmed electronic problem of at least one component, e.g. APV, DCU, MUX. Most of the sensors contained on this modules got recycled successfully.

- Bad Strips $> 2\%$ (50)
  This is in most cases again a handling issue. According to the ARC-tests

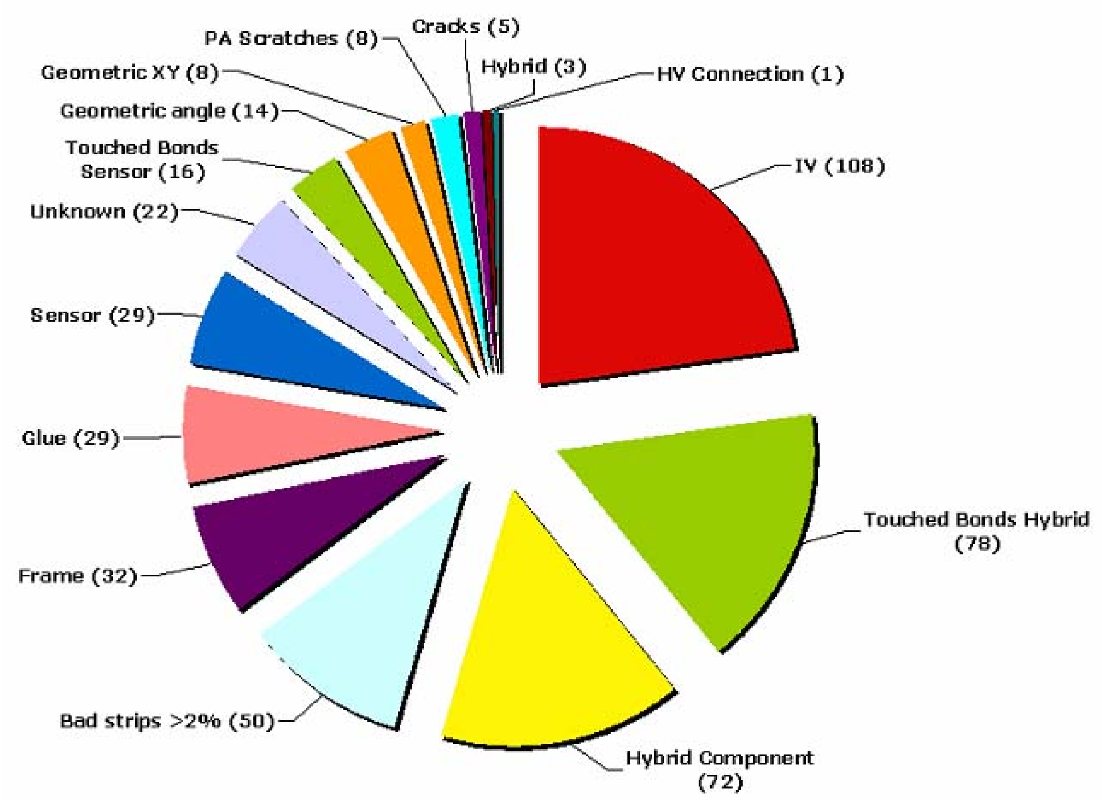

Figure 5.2: Distribution of the faulty TEC modules by the different faults. In brackets the number of modules showing the specified failures are displayed. This plot was also made for every single TEC module geometry separately, but the problems are more or less evenly distributed for each ring.

in the Tracker DB, in total 70 modules have more than 2% bad strips after the petal production. Here only 50 modules are flagged with this problem, because modules with more than 2% bad channels due to scratches on the sensor (problem: Sensor) and on the pitch adapter (problem: PA scratches) are not included in this number. Very few of these modules, which contain only slightly more than 2% bad channels will be useable as spares.

- Frame (32)
  Modules with a mechanically broken frame got disassembled wherever possible.

- Glue (29)
  Modules with glue on bonding pads or which got too much or too less glue during assembly. In a few cases and with a huge effort it would have been possible to save some of these sensors.

- Sensor (29)
  Modules with mechanically broken sensors. In most cases results of mishandling during module production and petal assembly. Some of these sensors broke during the shipment inside a transport box due to improper fixation.

- Unknown (22)
  For these modules it was not possible to define the exact reason for their faultiness, since they were 'lost' and could not be found again from the institutes at which they, according to the TrackerDB, should have been.

- Touched Bonds Sensor (16)
  Modules with touched or broken sensor to sensor or sensor to pitch adapter bonds. This number represents the modules where a repair or rebonding would have been too time consuming.

- Geometric Angle (14)
  Modules where either the sensor to frame or the sensor to sensor angle is outside the specifications. It was decided to not disassemble some of these modules, with only slightly deviations from the nominal value, and to use them as spares.

- Geometric XY (8)
  Modules where at least one of the XY sensor mounting precisions is outside the specifications. Again some of these modules were not disassembled to use them as spares.

- PA scratches (8)
  Modules containing a broken pitch adapter or a pitch adapter with scratches leading to too many open or noisy channels. Again the sensors could be saved.

- Cracks (5)
  Modules with cracks in the positioning holes of the carbon frame. A lot of these cracks could be repaired and only 5 modules with this problem were left unusable and got disassembled.

- Hybrid (3)
  Modules with a mechanically broken hybrid.

- HV Connection (1)
  On one modules the HV connection was completely destroyed .

It was not trivial to make this distribution, since for a lot of the faulty modules, the comments in the TrackerDB where not clear or totally missing. It was a huge effort, to check out the reasons for the faultiness of these modules. There existed even a lot of cases, where faulty modules were not flagged as faulty in the TrackerDB and also some good modules were flagged as faulty. Often the only chance to get certainty about the status of a module was to send an email to the centre where the module was located with the petition to check the module again, which in most of the cases was done within a few days. This was not possible for 22 modules which are flagged with the problem Unknown.

5.2 Touched Bonds

During the TEC petal assembly as much as 435 modules were found with touched bonds. These are 6,02% of the 7.228 assembled modules. This huge number was solely caused by handling failures which would have been completely unnecessary. Unfortunately it was not possible to definitely find out if this happened during the module production, during the shipment of the modules or during the mounting of the modules onto petals. With a huge effort 341 of these modules could be repaired, leaving 94 modules with touched bonds as losses. These repairs were mainly done by Ian McGill at CERN. 78 of these unrepairable modules were lost due to twisted or broken hybrid to APV or APV to pitch adapter bonds. It was not possible to repair them, because the bond pads on the APV are too small to bond for a second time. Although the bonding specialists came to the agreement, that a rebonding would never lead to satisfying results, in a very few cases, single hybrid bonds got rebonded like displayed in Figure 5.3. If the APV bond pads would have been a bit larger, a big part of the 78 faulty modules with touched hybrid bonds could have been repaired. Luckily the hybrids were not the limiting part in the module production and the sensors on these modules could be recycled in Vienna.

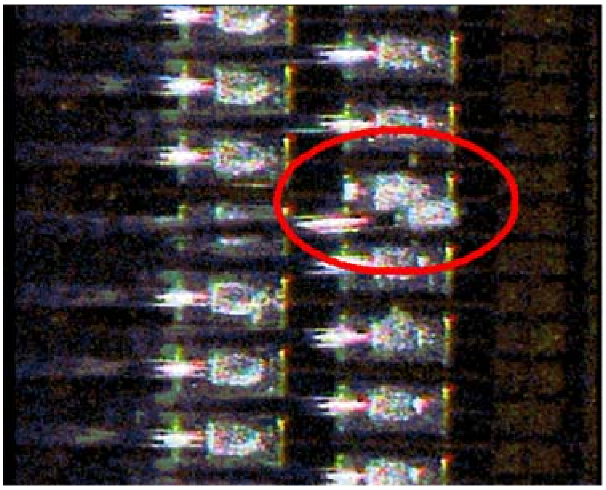

Figure 5.3: One of the very rare cases where a second bond was bonded on an APV bonding pad.

5.3 Sensor Recycling

The sensors of 222 modules[2] were disassembled before September 2006. 28 more modules got disassembled afterwards, but it was too late for producing new modules out of them, since the appropriate assembly centers moved already to other

[2]This number does again not include modules which contained hybrids from bad batches. Taking these modules into account, the sensors of 412 modules got disassembled, whereof only 46 sensors were unusable afterwards.

Ring	assembled modules	faulty modules	disassembled modules	lost sensors	remaining faulty
R1N	169	8	3	0	5
R1S	171	12	5	1	8
R2N	321	16	9	0	7
R2S	315	11	8	0	3
R3	711	44	26	10	28
R4	681	40	15	3	28
R4A	470	33	12	4	25
R5N	820	58	36	0	22
R5S	820	49	25	1	25
R6	946	43	24	0	19
R6A	167	7	3	0	4
R7	1.637	146	56	1	91
All	7.228	467	222	20	265

Table 5.1: The column lost sensors gives the number of modules, where the sensor broke during disassembly or failed in the subsequent sensor tests. The last column gives the remaining lost modules, after subtracting all modules where the sensor was successfully recycled.

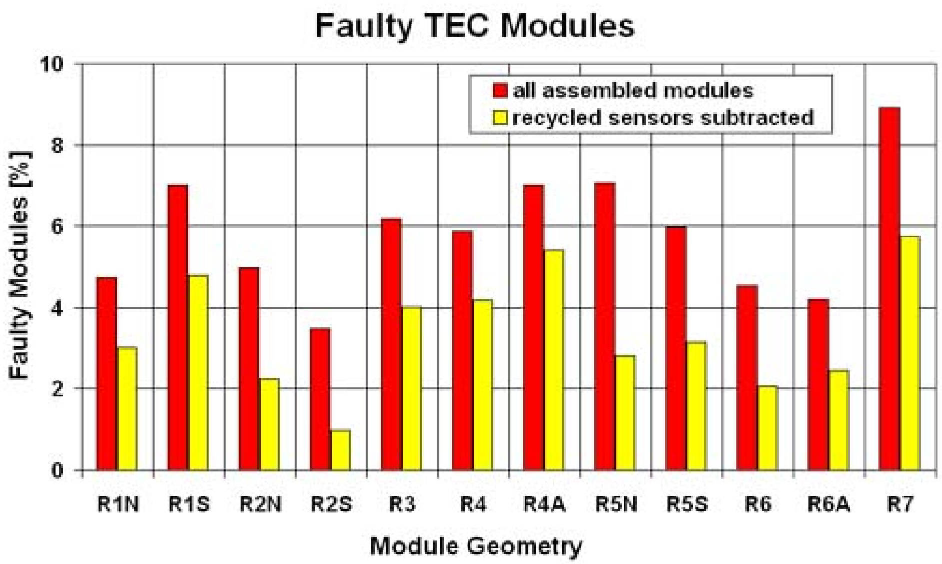

Figure 5.4: Percentage of the assembled faulty modules per geometry. In red, all assembled modules are included and in yellow the disassembled modules, where the sensors could be recycled, are not taken into account. In total 467 modules, 6,46% of the 7.288 assembled modules are faulty (red). When subtracting all modules, where the sensor was successfully recycled, only 265 modules, 3,77% of the remaining 7.026 assembled modules, are lost (yellow).

issues. All the sensors were recycled at HEPHY Vienna and each disassembly took about half an hour. At first, all sensor bonds had to be removed. Then the glue was softened with alcohol and the sensors were carefully detached from the frame with the help of a thin nylon string. In the cases of the very fragile alignment modules a second persons had to assist. Afterward the remaining glue on the sensor backplane was slowly rubbed off.

Out of the 222 disassembled modules only on 20 modules a sensor broke during the disassembly or was faulty in the subsequent sensor tests. The good sensors were afterward sent to the appropriate module assembly centers and got reintroduced into the module production.

Taking the recycled sensors into account, only 265 TEC modules, 3,77% of the remaining 7.026 produced modules (7.228 assembled modules minus 202 disassembled modules where the sensor was successfully recycled), are left faulty as displayed in Figure 5.4 and Table 5.1. Of course, this number reflects only the number of faulty modules that still contain sensors or where the sensors could not successfully be recycled. It gives no information about the losses of the other module parts.

Chapter 6

Finalised TEC Module Quality

Here the quality of the finished TEC modules after the module assembly on petals is summarised. The main steps during the module production were the reception tests of the industrially produced module parts, the precise mechanical assembly, the application of the thin wire micro-bond connections and the electrical functionality test in automated setups. The finalised modules got assembled onto petals, which were tested and mounted on carbon fibre discs. These carbon fibre discs were built together to form the two Tracker End Caps. The TEC+, displayed in Firgure 6.1, was already successfully cold tested and the cold test for the TEC- is running at the moment. In the end of February 2007 the two TECs will be mounted in the CMS Tracker. The quality assurance schemes of the different steps are described in this diploma thesis.

Ring	module type	produced modules	good	faulty	yield
R1N	2.5.17.14	169	161	8	95,27
R1S	2.5.18.15	171	159	12	92,98
R2N	2.6.19.16	321	305	16	95,02
R2S	2.6.20.17	315	304	11	96,51
R3	2.7.21.18	711	667	44	93,81
R4	2.8.22.19	681	641	40	94,13
R4A	2.18.22.19	470	437	33	92,98
R5N	2.9.23.20	820	762	58	92,93
R5S	2.9.24.21	820	771	49	94,02
R6	2.11.25.22	946	903	43	95,45
R6A	2.19.25.22	167	160	7	95,81
R7	2.13.26.23	1.637	1.491	146	91,08
total TEC		7.228	6.761	467	93,54

Table 6.1: The finalised amount and quality of the produced TEC modules. In Table 7.1 in the Appendix, the numbers for the other three subsystems and for the whole Silicon Strip Tracker are given.

The huge effort needed for module repairs is included. Out of the 7.228 produced modules 809 modules (11,2%) have at least one repair action in the TrackerDB. All the numbers are from September 2006, at a later date some minor changes appeared due to the ongoing repair effort done to create some more spare modules. In Table 6.1 these finalised numbers for the Tracker End Caps are listed.

It is important to mention, that in all the numbers prototype modules and modules containing hybrids from bad batches or hybrids with via-problems are not taken into account. Out of these 325 modules that were built with prototype or unusable hybrids, 190 got disassembled again and their sensors were successfully reintroduced into the module production.

Since 6.400 modules are needed to complete the two TECs, 361 (5,94%) good spare modules were produced by September 2006. This number will even slightly increase, after all the outstanding repairs are done. The number of available spare modules is sufficient for small repairs if an accident happens during the cold tests of the two Tracker End-Caps or during the Tracker integration.

Most impressive about the TEC module quality is, that only 8263 or 0,2% of the about 4,1 million channels included in the two Tracker End Caps are considered as bad channels. This number gets even more spectacular when compared with the target for the number of bad strips to be less than 2%.

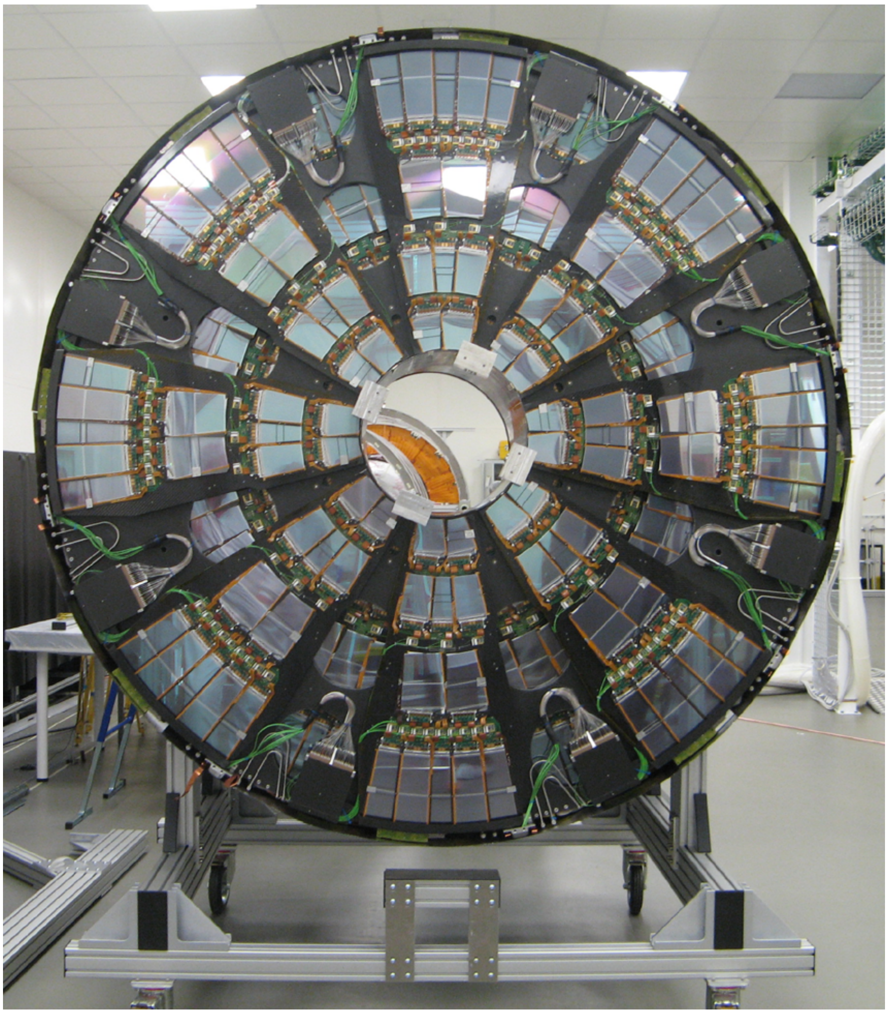

Figure 6.1: TEC+ after cold test.

Chapter 7

Conclusions

The module production for the Tracker End-Caps of the CMS Silicon Strip Tracker was a complete success. This was achieved even though the TEC module production was more difficult than the production of the other subsystems of the Silicon Strip Tracker due to the large number of different module geometries and the large amount of involved institutes; for the final TEC production almost all CMS institutes have contributed.

The positive outcome of this huge project could only be achieved because:

- All single components were extensively tested and stressed beyond their limits before the mass production was started.
- A very detailed quality assurance scheme was developed which contained multiple functionality test for every component during the production.
- Mostly automatic test setups were developed which ensured largely uniform test environments. So it was possible to compare the test results from the different institutes.
- Precise procedures were designed for every single production step (even trivial ones) which ensured that the knowledge did not vanish during this long time production. This was very important since at the contributing institutes some personal changes did happen.
- Every week, between the bimonthly Tracker meetings at CERN, a video conference within the CMS Tracker Collaboration was held. During them the current status of the production for each Institute was presented and occurred problems were discussed. Together solutions for arisen problems were developed and every change in the production was evaluated. This ensured, that the best solutions were found and the consistent dispatching of new instructions.
- The response to arising problems was very quick with even complete production stops if necessary.
- The central data base was consequent used, which was absolutely necessary to coordinate the production and to keep trace of the different components.

- The coordination and ideal distribution of the module components was centrally managed by HEPHY Vienna. The distribution of the finalised modules was centrally managed by the Institute de Recherches Subatomiques Strasbourg.

- Single institutes specialised for delicate actions like the sensor recycling, the repair of touched bonds and the repair of faulty modules. This ensured a central accumulation of the needed knowledge to perform these actions.

The handling and integration of modules into petals turned out to be very delicate. Many modules were damaged before they reached the integration center and during integration. Some defects were even added to the modules during the dismounting and rebuilding of petals which was done because of missing glue reinforcement, missing backplane bonds and in the rare cases when modules were faulty during the petal tests.

In the end, all occurred problems could be solved and the quality of the CMS Silicon Strip Tracker is excellent. Only 0,1% to 0,2% of the about 9,6 million channels included in the CMS Silicon Strip Tracker are considered as bad channels.

Bibliography

[1] HEPHY, *"Institute of High Energy Physics of the Austrian Academy of Sciences"; Nikolsdorfer Gasse 18, 1050 Wien, Austria (http://www.hephy.at/)*

[2] The BABAR Collaboration, *"Observation of CP violation in the B^0 meson system."; Phys.Rev.Lett. 87 (2001)*

[3] J. Engelen, *"The LHC project - overview and status"; Czechoslovak Journal of Physics, Vol. 55, PartI, B13 (2005)*

[4] The LHC Collaboration", *web page: "LHC Machine Outreach"; http://lhc-machine-outreach.web.cern.ch/lhc%2Dmachine%2Doutreach/*

[5] The LEP Electroweak Working Group, *"Search for the Standard Model Higgs boson at LEP"; Physics Letters B, Vol. 565 ,61-75 (2003)*

[6] M. Spira, *"QCD effects in Higgs physics"; WILEY-VCH Verlag Berlin GmbH, Fortschritte der Physik Vol 46, 203284 (1998)*

[7] C.-E. Wulz, *"CMS Physics Overview"; Czechoslovak Journal of Physics, Vol. 52, Suppl. C 155-170 (2002)*

[8] K. Desch, J. Kalinowski, G. Moortgat-Pick, K. Rolbiecki and W.J. Stirling, *"Combined LHC/ILC analysis of a SUSY scenario with heavy sfermions"; BABAR-CONF-06/038, SLAC-PUB-12028 (2006)*

[9] Daisuke Ida, Kin-ya Oda and Seong Chan Park, *"Rotating Black Holes at Future Colliders."; Phys.Rev. D73, 124022 (2006)*

[10] A. Schopper, *"Flavor Physics and CP Violation at LHC"; Flavor Physics and CP Violation Conference, Vancouver (2006)*

[11] B. Müller, *"Heavy Ions - prospects at the LHC"; Czechoslovak Journal of Physics, Vol 55, PartI, B313 (2005)*

[12] D. Acosta et al., *"CMS Physics Technical Design Report Volume I: Detector Performance and Software"; CERN/LHCC 2006-001, CMS TDR 8.1 (2006)*

[13] J. Lykken, *"Phenomenology beyond the Standard Model"; Czechoslovak Journal of Physics, Vol 55, PartII, B577 (2005)*

[14] The CMS Collaboration, *web page: "CMS Outreach"; http://cmsinfo.cern.ch/outreach/CMSdetectorInfo/CMSdetectorInfo.html*

[15] The CMS Collaboration, *"The CMS Electromagnetic Calorimeter Technical Design Report"; CERN/LHCC 97-33, CMS TDR 4 (1997)*

[16] The CMS Collaboration, *"The Hadron Calorimeter Technical Design Report"; CERN/LHCC 97-31, CMS TDR 2 (1997)*

[17] Department of Physics and Astronomy, Georgia State University, *web page: "HyperPhysics"; http://hyperphysics.phy-astr.gsu.edu/Hbase/hframe.html*

[18] The CMS Collaboration, *"Muon Technical Design Report"; CERN/LHCC 97-32, CMS TDR 3, (1997)*

[19] J. Bartels et al., *"The European Physical Journal C"; Springer Verlag, Vol. 15, No.1-4 (2000)*

[20] M. Friedl, *PhD Thesis: "The CMS Silicon Strip Tracker and its Electronic Readout"; University of Technology Vienna (2001)*

[21] M. Friedl, T. Bauer, M. Krammer, *"A Simple Model of Charge Collection in Silicon Detectors"; Nuclear Instruments and Methods in Physics Research A 461, 192-196 (2001)*

[22] W. de Boer et al., *"Lorentz angle measurements in irradiated silicon detectors between 77 and 300 K"; NIM A, Vol. 461, 200-203 (2001)*

[23] S. Breibant et al., *"Investigation of design parameters for radiation hard silicon microstrip detectors"; Nuclear Instruments and Methods in Physics Research A 485, 343-361 (2002)*

[24] G. Kramberger, *"Recent results of the RD50 collaboration"; 6th International Conference on Radiation Effects on Semiconductor Materials, Detectors and Devices (2006)*

[25] G. Lindstrm, *"Radiation Damage in Silicon Detectors"; 9th European Symposium on Semiconductor Detectors, Schloss Elmau, Germany (2002)*

[26] M. Moll, *PhD Thesis: "Radiation damage in silicon particle detectors: Microscopic defects and macroscopic properties."; Hamburg University, DESY-THESIS-1999-040 (1999)*

[27] R. Wunstorf, *PhD Thesis: "A Systematic investigation of the radiation hardness of silicon detectors for high-energy physics experiments" (in German); University of Hamburg, DESY FH1K-92-01 (1992)*

[28] E. Forton, *PhD Thesis: "Radiation damage induced by neutrons in CMS silicon sensors"; Université catholique de Louvain, FYNU (2006)*

[29] S. Yong Choi, F. Lehner, *"What do we know about radiation damage in silicon detectors"; The D⊘ Experiment, Fermilab, D⊘ note 3803 (2000)*

[30] D. Zontar, *PhD Thesis: "Study of radiation damage in silicon detectors for high luminosity experiments at LHC"; University of Ljubljana (1998)*

[31] L. Borello et. al., *"Sensor design for the CMS Silicon Strip Tracker"; CMS Note 2003/020, CERN (2003)*

[32] M. Krammer et al., *"The Silicon Sensors for the Compact Muon Solenoid Tracker - Design and Qualification Procedure"; NIM A, Vol. 517, 1-3, 77-93 (2004)*

[33] R. Turchetta et. al., *"Design and results from the APV25, a deep sub-micron CMOS front-end chip for the CMS tracker"; NIM A, Vol. 466, 359365 (2001)*

[34] The CMS Collaboration, *web page: "CMS Tracker Construction Database"; http://cmsdoc.cern.ch/∼cmstrkdb/*

[35] T. Bergauer, *"Monitoring of the Fabrication Process of Silicon Strip Sensors for Large Scale Productions"; SNIC Symposium, Stanford, California (2006)*

[36] T. Bergauer, *Diploma Thesis: "Process Quality Control of Silicon Strip Detectors for the CMS Tracker"; University of Technology Vienna (2004)*

[37] A. Dierlamm, *"Irradiation qualification of CMS silicon tracker components with protons "; NIM A, Vol. 514, 1-3 (2003)*

[38] UCL Institut de Physique Nucléaire, *web page: "Tests of hybrids circuits for the CMS tracker : FHIT project"; http://www.fynu.ucl.ac.be/themes/he/cms/activities/tracker/hybrids.html*

[39] B. Reinhold, *Diploma Thesis: "Automatic Bonding Test of Front End Hybrids for the CMS Tracker"; RWTH Aachen University (2004)*

[40] U.Goerlach, *"Industrial Production of Front-End Hybrids for the CMS Silicon Tracker"; Proc. of the 9th Workshop on Electronics for LHC experiments (2003)*

[41] CMS Gantry Working Group, *web page: "Gantry Center Assembly Procedures"; http://www.ba.infn.it/∼CMS_TRKR/gantry_files/gantry_proc.ps*

[42] A. Honma et. al., *"An Automated Silicon Module Assembly System for the CMS Silicon Tracker"; CMS NOTE 2002/005 (2002)*

[43] RWTH Physics AC-lb, *web page: "Local CMS Homepage at RWTH Aachen-lb"; http://accms04.physik.rwth-aachen.de/∼cms/Tracker/Modules/*

[44] S. Costa and the CMS Tracker Bonding Working Group, *web page: "Proposed Procedure for Bonding of the CMS Silicon Tracker Modules"; http://cms.ct.infn.it/bonding/*

[45] M. Krammer, *Talk: "Module Production for the CMS Tracker: Problems and Achieved Quality"; 15th International Workshop on Vertex Detectors, preprint submitted to Elsevier Science (2006)*

[46] T. Franke, *PhD Thesis: "Development and Evaluation of a Test System for the Quality Assurance during the Mass Production of Silicon Microstrip Detector Modules for the CMS Experiment"; University of Technology Aachen (2005)*

[47] M. Axer et. al., *"Testing of FE Hybrids and Si detector modules for the CMS Tracker"; NIM A, Vol. 485, 1-2, 73-77 (2002)*

[48] M. Meschini et. al., *"Procedures For CMS Silicon Tracker Module Testing Using ARC System"; CMS Internal Note 2004/018, May 2004*

[49] A. Affolder et. al., *"Test of CMS tracker silicon detector modules with the ARC system"; NIM A, Vol. 535, 374378 (2004)*

[50] R. Brauer et. al., *"Design and Test Beam Performance of Substructures of the CMS Tracker End Caps"; CMS NOTE 2005/025 (2005)*

Appendix

Tracker Inner Barrel

Ring	Type	produced modules	good	bad	yield
L12P.6D	1.1.1.1	839	822	17	97,97
L12SL.6U	1.1.2.2	427	406	21	95,08
L12SR.6U	1.1.3.3	433	412	21	95,15
L34P.4D	1.2.4.1	1.327	1.274	53	96,01
total TIB		3026	2914	112	96,30

Tracker Inner Disc

Ring	Type	produced modules	good	bad	yield
R1P.6D	4.15.5.4	159	156	3	98,11
R1SB.6U	4.15.7.6	81	78	3	96,30
R1SF.6U	4.15.6.5	82	82	0	100,00
R2P.6D	4.6.8.7	164	158	6	96,34
R2SB.6U	4.6.10.9	86	80	6	93,02
R2SF.6U	4.6.9.8	87	85	2	97,70
R3P.4D	4.7.11.10	260	257	3	98,85
total TID		919	896	23	97,50

Tracker Outer Barrel

Ring	Type	produced modules	good	bad	yield
L12P.4D	3.4.14.12	564	550	14	97,52
L12P.4U	3.4.12.12	577	567	10	98,27
L12S.4D	3.4.16.13	565	556	9	98,41
L12S.4U	3.4.15.13	561	552	9	98,40
L34P.4U	3.4.12.11	1.417	1.399	18	98,73
L56P.6U	3.3.13.11	1.750	1.724	26	98,51
total TOB		5.434	5.348	86	98,42

total Tracker	produced modules	good	bad	yield
	16.607	15.919	688	95,47

Table 7.1: The amount and quality of the produced Tracker Inner Barrel (TIB), Tracker Inner Disk (TID) and Tracker Outer Barrel (TOB) modules. In the last table the amount and quality of the total produced CMS Tracker modules are listed.

Acknowledgements

Really a lot of people at HEPHY Vienna and in the CMS collaboration contributed directly or indirectly to the work presented in this thesis. It was really great being part of this community and I hope that I can continue.

First of all I would like to thank Manfred Krammer for the possibility of making this thesis. He gave me not only constant support and advise during my work, but also, together with Meinhard Regler and Walter Bartl, inspired my interest in high energy physics. In addition he encouraged me a lot to break my panic for presentations down, and for not taking my first really disastrous talk too serious.

I want to express my thanks to our project leader Josef Hrubec for his support and help not only for the solution of the module alignment problem, but also for having the right ideas whenever needed.

Huge thanks go to Thomas Bergauer, Marko Dragicevic, Markus Friedl, Edmund Widl and Christian Irmler for answering all my questions and helping me to get a deeper knowledge in high energy physics and in the used electronics. Especially Thomas Bergauer and Marko Dragicevic were involved in a lot of the work presented in this thesis and had always time for discussions about physics and other stuff.

I would like to acknowledge Dieter Uhl, Roland Stark and Margit Oberegger for a lot of discussions and help in different issues, like module repairs, bonding and the the conductive glue problem. Especially Dieter Uhl had always time for small jokes and made my work enjoyable.

All the people at HEPHY and especially the people mentioned above made me, from the beginning, feel very comfortable at HEPHY Vienna. This starts with friendly small talks and ends with the Semiconductor Detector Group Skiing Day.

I never would have been able to reach that far without my family. Special thanks goes to my parents Yvonne Hänsel and Arno Hänsel and their new partners Uschi Knoglinger and Günter Tautscher. Not only did you support me the whole time, but also enriched my life with my five brothers and sisters Anatol Tautscher, Fiona Hänsel, Naomi Hänsel, Ben Hänsel and Nico Hribernik. Special thanks to all of them for beeing what they are and especially how they are. Thanks to my grandparents Ingrid and Hermann Hänsel and Lilo and Wolf Renner for your time and support. Sadly Hermann Hänsel has gone before he could see me finish my studies.

Vinzenz Schwarz, Edmund Widl, Thomas Pommerening and Klaus Beiter, thanks a lot for all these days and nights. Since it's not possible for me to name all of my friends, I just want to mention one more friend, Anni Döring, for helping

me immense with spending so much time with my children. Without you I would not have been able to take the time for this work.

Last but not least, the biggest thanks goes to the three most important persons in my life. What can I say, I love you Dani and I love our two children Ronja and Leo.

Keep on smiling!